



HAL
open science

Instabilities of non isothermal flows and Two-phase flows

Harunori Yoshikawa

► **To cite this version:**

Harunori Yoshikawa. Instabilities of non isothermal flows and Two-phase flows. Fluid mechanics [physics.class-ph]. Université Nice Sophia Antipolis, 2015. tel-01284088

HAL Id: tel-01284088

<https://hal.science/tel-01284088>

Submitted on 7 Mar 2016

HAL is a multi-disciplinary open access archive for the deposit and dissemination of scientific research documents, whether they are published or not. The documents may come from teaching and research institutions in France or abroad, or from public or private research centers.

L'archive ouverte pluridisciplinaire **HAL**, est destinée au dépôt et à la diffusion de documents scientifiques de niveau recherche, publiés ou non, émanant des établissements d'enseignement et de recherche français ou étrangers, des laboratoires publics ou privés.

Rapport d'Habilitation à Diriger des Recherches

Université Nice Sophia Antipolis

Spécialité: Mécanique

Instabilités des écoulements non isothermes et Écoulements diphasiques

présenté par

Harunori NAKAGAWA-YOSHIKAWA

Soutenue le 13 novembre 2015 devant le jury composé de

| | | |
|-----|-----------------------|------------|
| M. | Gérard Iooss | Président |
| Mme | Laurette Tuckerman | Rapporteur |
| M. | Thierry Dauxois | Rapporteur |
| M. | Patrice Le Gal | Rapporteur |
| M. | Masato Nagata | Examineur |
| M. | José-Eduardo Wesfreid | Examineur |

à Hiromi

Instabilités des écoulements non isothermes et Écoulements diphasiques

Abstract

This manuscript is composed of three parts. Part I is devoted to theoretical investigations of the thermo-electrohydrodynamic (TEHD) convection. This convection is generated by an electrohydrodynamic (EHD) effect, called *dielectrophoretic (DEP) force*, on non isothermal fluid layer. This thermal force can be assimilated with the thermal Archimedean force by introducing an electric effective gravity. This gravito-EHD analogy enables us not only to understand intuitively the flow motion under the DEP force, but also to simulate geophysical flows at global scales by EHD experiments. Similarities and differences between the TEHD convection and the thermal convections in gravitational fields are clarified. In Part II, non-isothermal Taylor-Couette (TC) flows are investigated by linear perturbation theory. Flows in a vertical TC system as well as in a TC system in microgravity that is subjected to the radial DEP force are considered. Focus is the effects of two radial thermal forces on flow behavior: one, called *centrifugal buoyancy*, arising from the centrifugal acceleration; the other being the DEP force. Oscillatory modes associated with these two forces are discovered in certain parameter ranges. In Part III, three experimental investigations on different two-phase flow systems are reported: the stability of a bubble in an oscillatory flow; the dynamics of vapor bubbles on a heating wall surface in a shear flow; formation of spiral patterns by bubbles at a liquid free surface.

Résumé

Ce manuscrit se compose de trois parties. La Partie I est consacrée aux études théoriques de la convection thermo-électrohydrodynamique (TEHD). Cette convection est générée par un effet électrohydrodynamique (EHD), appelé *force diélectrophorétique (DEP)*, sur une couche de fluide non isotherme. Cette force thermique peut être assimilée à la force d'Archimède thermique, en introduisant une gravité effective électrique. Cette analogie gravito-EHD nous permet non seulement de comprendre intuitivement le mouvement de fluide sous la force DEP, mais aussi de simuler des écoulements géophysiques à l'échelle globale par des expériences EHD. Des similitudes et différences entre la convection TEHD et les convections thermiques dans des champs gravitationnels sont clarifiées. Dans la Partie II, des écoulements de Couette-Taylor (CT) non isothermes sont analysés par la théorie des perturbations linéaires. Les écoulements dans un système CT vertical ainsi que dans un système de CT en microgravité qui est soumis à la force radiale DEP, sont considérés. On s'intéressera particulièrement aux effets de deux forces radiales thermiques sur le comportement des écoulements: l'une due à l'accélération centrifuge; l'autre étant la force DEP. Les modes oscillatoires associés à ces deux forces sont mis en évidence dans certaines gammes de paramètres. En Partie III, trois études expérimentales sur différents écoulements diphasiques sont présentées: la stabilité d'une bulle dans un écoulement oscillant; la dynamique des bulles de vapeur sur une surface chauffante dans un écoulement pariétal; la formation de motifs spiralés de bulles à la surface libre d'un liquide.

Preface

This manuscript gives a summary of my research activities after the completion of my PhD in 2006. The majority of the presented researches were carried out during my postdoctoral experiences (2007–2013) outlined in *General Introduction* at the beginning of the manuscript as well as in my CV included in appendix A.

In the manuscript, the presentation of obtained results by these researches is made with classifying the researches into the following two large categories according to subjects regardless their chronological order: Instabilities of non isothermal flows (Parts I & II) and Two phase flows (Part III).

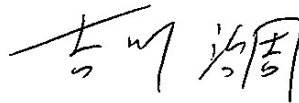
The description of each research is only a brief summary. Interested readers are invited to refer to related publications found in a publication list given in appendix B. Some of the publications are included in appendix C.

All the chapters have been written in English for non French speaking jury members of the present “Habilitation à Diriger des Recherches.”

Acknowledgements

I wish to express my sincere gratitude to my former and current colleagues who helped me during the researches reported in the manuscript. I would like to thank Drs. Pascal Kurowski, Philippe Petitjeans, Farzam Zoueshtiagh and Hervé Caps, with whom I did my first postdoctoral position. They made me familiar with microgravity sciences. I learned many things from them about experimental approaches to two-phase flows. I would also like to thank to Prof. Catherine Colin who gave me the opportunity of doing a postdoctoral position with her. I worked for the first time on the boiling, a complex phenomenon that is related to many industrial applications. I acknowledge the encouragement and support that she offered me throughout my stay in Toulouse. I'm grateful to Drs. Christian Mathis, Philippe Maïssa and Germain Rousseaux, with whom I had an opportunity to work on a fascinating spiral pattern formation in a simple flow system. For this subject, I did fluid mechanics and botany at the same time, an interesting experience. I'm also grateful to Prof. Innocent Mutabazi and Dr. Olivier Crumeyrolle, with whom I met the electrohydrodynamics (EHD). I'm very happy to have been familiar with problems in the EHD, since they remind me of my background in electrical engineering. I acknowledge invaluable advice and help from Prof. Innocent Mutabazi as well as his enthusiasm in physics that have been transmitted to me.

I thank the jury members who kindly accepted to read and comment this manuscript and come all the way long to Nice for my presentation.



Harunori NAKAGAWA-YOSHIKAWA

Université Nice Sophia Antipolis
September, 2015

Introduction générale (Traduction en français des pages 1–4)

Carrière scientifique

Doctorat et Expériences postdoctorales

J'ai obtenu mon diplôme de bachelier en génie électronique à l'Université Doshisha à Kyoto au Japon en mars 2000. Puis, je fis mes études de master en génie électronique à la même université (de l'avril 2000 au mars 2002), en travaillant au Laboratoire de Physique Appliquée sur la dynamique des plasmas non-neutres sous la direction du Prof. Motoi Wada et du Dr. Toshiro Kasuya. Ma recherche a été consacrée aux effets de la diffusion moléculaire sur le profil de vitesse d'un jet de gaz d'électrons. Pendant ces études de master, j'ai été sélectionné pour un programme d'échange d'étudiants entre la Faculté de génie de l'Université et de l'École Supérieure de Physique et de Chimie Industrielles (ESPCI). Ainsi, j'ai eu une opportunité de faire un stage au sein du laboratoire de Physique et Mécanique des Milieux Hétérogènes (PMMH) sous la direction du Dr José Eduardo Wesfreid (Septembre 2000 - Juillet 2001). J'ai découvert les problèmes de stabilité hydrodynamique, en travaillant sur l'instabilité Rosensweig de la surface libre d'une couche de ferrofluide dans un champ magnétique.

Après l'obtention du diplôme de master, j'ai commencé en 2002 ma carrière scientifique, en préparant ma thèse au laboratoire PMMH sous la direction du Dr Wesfreid. Au début, je me suis intéressé à la stabilité de la surface d'un milieu granulaire cisailé par un liquide visqueux et j'ai travaillé sur la formation des rides de sable sous l'influence d'un écoulement oscillant [67]. J'y ai appris des méthodes de résolution des problèmes de stabilité pour un état de base et j'ai développé un code numérique. Puis, je suis retourné à un problème analogue pour une interface liquide-liquide non miscibles, où le cisaillement oscillant tangentiel provoque une instabilité pour former des ondulations à l'interface [102,103]. Ce problème a été moins étudié que la stabilité d'une surface libre de liquide soumis à des vibrations verticales, c.-à-d., le problème de l'instabilité de Faraday. J'ai effectué l'analyse de stabilité linéaire et comparé les résultats obtenus avec des résultats expérimentaux obtenus dans une expérience que j'avais conçue et réalisée. Ma thèse, intitulée « Instabilités des interfaces sous oscillations », est constituée par ces travaux théoriques et expérimentaux. Elle a été soutenue en 2006 devant le jury composé des Prof. Stéphane Zaleski, Prof. Tatyana Lyubimova, Prof. Philippe Gondret, Prof. Innocent Mutabazi, et Dr. José Eduardo Wesfreid.

Après la thèse, j'ai travaillé en tant que chercheur postdoctoral dans différents laboratoires en France avec différents chercheurs. Tout d'abord, je me suis joint à une équipe de recherche des Drs Philippe Petitjeans et Pascal Kurowski au PMMH et j'ai étudié la stabilité de bulles soumises à un écoulement oscillant en micropesanteur (Février 2007 - Août 2007). En travaillant avec le Dr Farzam Zoueshtiagh (IEMN, Lille) et le Dr Hervé Caps (Université de Liège), j'ai réalisé des expériences et analysé les résultats obtenus afin de caractériser la stabilité des bulles et de révéler le mécanisme de scission observée. Nous avons montré que la taille des bulles stables était limitée par la longueur capillaire basée sur l'accélération de l'écoulement oscillant et que l'inertie de l'écoulement du liquide était responsable de la scission [94,104].

Après cette première expérience dans le domaine de la micropesanteur, j'ai obtenu une bourse postdoctorale du Centre National d'Etudes Spatiales (CNES) et travaillé avec le Prof. Catherine Colin à l'Institut Mécanique des Fluides de Toulouse pour un projet expérimental sur l'ébullition nucléée en micropesanteur (Septembre 2007 - Août 2009). Je ai conçu et réalisé une expérience, en participant aux deux campagnes de vols paraboliques, l'une organisée par le CNES et l'autre par l'Agence spatiale européenne (ESA) [88,95]. Nous avons développé un modèle mécanistique de la dynamique d'une bulle de vapeur isolée, qui se développait et était en mouvement au voisinage d'une paroi chauffée. Nous avons examiné ce modèle, en le comparant avec les données obtenues dans l'expérience.

Les deux expériences postdoctorales m'ont fait connaître les sujets et les problèmes des sciences et technologies en micropesanteur.

En Septembre 2009, je me suis installé à Nice pour un autre poste postdoctoral et je me suis joint à une équipe de recherche des Dr Christian Mathis, Philippe Maïssa et Germain Rousseaux au Laboratoire J.-A. Dieudonné (Septembre 2009 - Décembre 2011). Nous étions intéressés par la formation de motif dans un système d'un écoulement diphasique qui semblait être similaire à la phyllotaxie, c.-à-d., la formation de l'arrangement régulier des feuilles autour d'une tige d'une plante. Par des expériences et une modélisation théorique, nous avons montré que le mécanisme de la formation était similaire à celui proposé pour la phyllotaxie [98,99]. A la fin de ce poste postdoctoral, j'ai aussi travaillé pour un projet sur l'ébullition nucléée pendant quelques mois. J'ai mené la recherche sur le champ de température entourant une bulle de vapeur en croissance sur une surface chauffante. La thermométrie à fluorescence induite par laser à deux colorants a été appliquée pour la mesure de température [42].

Ma dernière expérience postdoctorale était au Havre (Janvier 2012 - Août 2013) avec le Prof. Innocent Muta-bazi au Laboratoire Ondes et Milieux Complexes (LOMC). La première année a été consacrée à une analyse théorique de la convection thermique d'un fluide diélectrique dans un champ électrique. Cette convection, appelée *la convection thermo-électrohydrodynamique*, est induite par une composante de la force électrohydrodynamique. Pour mener la recherche sur ce sujet, j'ai aussi travaillé avec le Dr Olivier Crumeyrolle. Nous avons établi, par une analyse de stabilité linéaire, des critères pour que la convection se développe dans différentes configurations d'électrodes [52,96,97]. Nous avons également calculé le transfert de chaleur par une simulation numérique directe dans une géométrie particulière. Pendant huit derniers mois de ce poste postdoctoral, j'ai travaillé sur la stabilité d'un écoulement de Taylor-Couette, soumis à un gradient radial de température et clarifié les effets de ce gradient sur la stabilité de l'écoulement [101]. Je me suis consacré également à un problème similaire mais avec un champ électrique radial. J'ai constaté que les forces thermiques radiales pourraient générer des ondes [100]. À la fin de ce postdoctorat, j'ai commencé à travailler sur le transfert de chaleur dans les tourbillons de Görtler développés sur une surface de paroi concave en collaboration avec le Dr Jorge Peixinho. Nous avons développé un modèle théorique qui a pris en compte la conductivité thermique finie de la paroi [36].

Pendant le développement de ma carrière scientifique en tant que chercheur, comme décrit ci-dessus, j'ai aussi enseigné en sciences physiques : j'ai encadré des stages de licence et master (voir Annexe A pour plus de détails). J'ai aussi participé à la formation de thésards pendant mes séjours à Nice et au Havre. Lorsque je travaillai à Toulouse, j'ai donné des cours sur l'automatisme (systèmes de contrôle analogiques, systèmes de contrôle numérique) au Département d'Electronique de l'Institut Catholique d'Arts et Métiers pour des élèves en premier cycle ainsi que pour les ingénieurs.

Après ces expériences de recherche et d'enseignement, j'ai obtenu en 2013 un poste de Maître de Conférences de Section 60 (Mécanique, Génie mécanique, Génie civil) du CNU à l'Université Nice Sophia Antipolis (UNS).

Poste actuel à l'Université Nice Sophia Antipolis

Depuis Septembre 2013, je suis maître de conférence à Université Nice Sophia Antipolis. Je suis attaché à l'école d'ingénieur, *École Polytechnique Universitaire de Nice Sophia*, et j'assure des cours et TDs pour les élèves de première année du Département Bâtiments. J'enseigne actuellement en *Mécanique générale*, *Thermodynamique*, *Outils numériques*, et *Mécanique des fluides* afin de donner aux élèves une base scientifique qui leur permette une spécialisation ultérieure en ingénierie du bâtiment. Je suis responsable du programme de formation et des élèves de la première année. J'ai aussi la responsabilité de la démarche qualité du département en vue de maintenir le certificat ISO 90001.

Pour ma recherche, je travaille au laboratoire J.-A. Dieudonné, où j'ai déjà séjourné en tant que chercheur postdoctoral. Je suis intégrée à l'équipe de recherche *Modélisation numérique et dynamique des fluides*, dirigé par le Prof. Didier Clamond. Je suis un membre du groupe expérimental au sein de l'équipe, composé des Drs Christian Mathis, Philippe Maïssa et Pascal Henry Biwolé.

Activités de recherche actuelles

Mes activités de recherche actuelles sont concentrées aux instabilités électrohydrodynamiques (EHD) d'écoulements non isothermes. La recherche sur ce sujet est motivée par l'analogie entre une force EHD thermique et la poussée d'Archimède thermique. En utilisant cette analogie, on peut simuler une certaine classe d'écoulements géophysiques par des expériences en laboratoire. Cette recherche est aussi motivée par l'application potentielle de la force EHD thermique aux systèmes thermiques qui sont utilisés en micropesanteur et dans des dispositifs microfluidiques. Je suis familier avec la force EHD thermique depuis mon expérience postdoctorale au Havre. En continuant la collaboration avec le groupe du LOMC au Havre et en développant une collaboration avec le Prof. Masato Nagata de l'Université de Tianjin en Chine, je mène des analyses théoriques sur des écoulements générés par la force EHD thermique, soit dans un condensateur plan, soit dans un condensateur cylindrique. Depuis mon arrivée à Nice en Septembre 2013, j'ai déposé des projets de recherches sur ce sujet à différents appels de l'ANR et du CNRS. Un des projets a été retenu pour l'appel « Projet Exploratoire Premier Soutien - Physique Théorique et ses Interfaces » en 2014. L'UNS soutient également ce projet en finançant la collaboration avec le Prof. Nagata en 2014 et 2015.

Je travaille aussi sur deux autres sujets. Le premier concerne la convection Rayleigh-Bénard avec des bulles de vapeur injectées. La recherche est motivée par l'importance de l'intensification du transfert de chaleur par des écoulements diphasiques dans l'industrie. L'objectif est d'améliorer, par des études expérimentales, notre compréhension actuelle sur les effets thermiques et mécaniques des bulles de vapeur sur le flux et le transfert thermique global. En particulier, l'interaction thermique et mécanique entre des bulles et des plumes thermiques dans des régimes non linéaires de l'écoulement sera étudiée. Cette recherche, menée avec l'un de mes collègues, le Dr Christian Mathis, est soutenu par l'UNS. Elle fait partie d'un projet de collaboration avec le Prof. Thierry Coupey (Institut du Calcul Intensif, Nantes) et le Dr Séverine Boyer (PPRIME, Poitiers), qui effectuent la simulation numérique et la modélisation théorique.

Le deuxième sujet est le mouillage d'une surface solide, en présence de particules de taille submillimétriques. Le comportement dynamique des lignes de contact sur une surface contaminée par des particules est étudié par des approches expérimentales, théoriques et numériques. La recherche est motivée par la propriété d'auto-nettoyage de surfaces solides, qui se rapporte à de nombreuses applications industrielles. Cette recherche vient de commencer dans le cadre d'un projet de collaboration internationale coordonné par le Prof. Farzam Zoueshtiagh (IEMN, Lille) et le Prof. Ichiro Ueno (Université des Sciences de Tokyo, Japon), avec un soutien financier du CNRS et de la JSPS¹. Le travail expérimental est mené à l'IEMN et à l'Université des Sciences de Tokyo avec des dispositifs expérimentaux existants. Je travaille sur la modélisation théorique du comportement de la ligne de contact et j'effectue également l'analyse des données expérimentales en collaboration avec d'autres partenaires en France et au Japon.

1. Japan Society for the Promotion of Science

Organisation du mémoire

En rédigeant le présent mémoire, j'ai essayé de résumer les résultats scientifiques essentiels que j'ai obtenus depuis l'obtention de mon diplôme de doctorat. Puisque j'ai fait quatre postdoctorats, les sujets abordés sont variés. L'accent du mémoire est, cependant, mis sur les instabilités électrohydrodynamiques : ce sont les sujets sur lesquels porteront essentiellement mes activités de recherche dans les années qui viennent.

La Partie I est consacrée à la convection TEHD. La base de la modélisation théorique des écoulements EHD est donnée dans le Chap. 1, en soulignant l'analogie entre la force EHD thermique et la poussée d'Archimède thermique due à la pesanteur. Le Chapitre 2 traite l'instabilité TEHD et la convection en résultant, dans une couche de fluide entre deux électrodes planes parallèles. Le Chapitre 3 concerne l'instabilité TEHD en géométrie annulaire cylindrique, où une couche de fluide est soumise à un champ électrique imposé par deux électrodes cylindriques concentriques. La Partie II est consacré à la stabilité de l'écoulement Couette-Taylor soumis au chauffage radial. Dans le Chap. 4, un système de Couette-Taylor vertical est considéré. Dans le Chap. 5, un système de Couette-Taylor soumis également à un champ électrique radial est considéré en micropesanteur. La Partie III contient trois travaux expérimentaux sur différents écoulements avec des bulles. Les résultats sur la stabilité d'une bulle dans un écoulement oscillant, le comportement d'une bulle de vapeur sur une paroi chauffée dans un écoulement parietal, et la formation d'un motif de bulles sur une surface libre sont présentés dans les Chaps. 6, 7, et 8, respectivement. Un projet de recherche pour les années qui viennent est donnée dans la Partie IV.

Résumés en français des Chapitres 1–8

PARTIE I. INSTABILITÉ THERMO-ELECTROHYDRODYNAMIQUE (TEHD)

Chapitre 1. Analogie Gravito-EHD

La première partie du présent mémoire est consacrée à une convection thermique, appelée *convection thermo-électrohydrodynamique (TEHD)*, générée par une force électrohydrodynamique. Au chapitre 1, la base théorique de cette convection est donnée pour les analyses présentées dans les chapitres ultérieurs. On souligne l'analogie de la force motrice de la convection TEHD avec la poussée d'Archimède thermique, en introduisant la notion de la gravité électrique (Sec. 1.1). Après avoir discuté des conditions nécessaires de la domination de cette force sur d'autres effets du champ électrique appliqué au fluide en Sec. 1.2, les équations régissant la convection TEHD sont présentées en Sec. 1.3. La section 1.4 est consacrée à des états conductifs du fluide dans trois configurations particulières d'électrodes. En Sec. 1.5, les nombres adimensionnels caractérisant la convection TEHD sont introduits avec une version adimensionnelle des équations régissant la convection TEHD.

Chapitre 2. Convection TEHD dans une géométrie plane

Des études théoriques et numériques de la convection TEHD en géométrie parallèle plane sont menées afin d'examiner l'analogie de la convection TEHD avec la convection de Rayleigh-Bénard (RB). Bien que cette analogie soit connue depuis le début des études théoriques et expérimentales de la convection TEHD, elle n'a pas été étudiée en détails. En menant des études théorique et numérique, nous confirmons les similitudes entre ces deux phénomènes de convection par rapport aux paramètres critiques et au comportement faiblement non linéaire des écoulements convectifs développés. Cependant, des analyses détaillées montrent des différences essentielles dues à deux facteurs : la non-uniformité du champ de gravité électrique et la rétroaction du champ électrique sur le champ de température. Le premier effet est significatif seulement si la variation thermique de la permittivité diélectrique est importante : $\frac{1}{\epsilon} \frac{d\epsilon}{dT} \Delta T > 1$. En revanche, le second effet différencie toujours la convection TEHD de celle de RB : dans une convection TEHD, une perturbation en champ de température induit une perturbation du champ électrique, et donc une perturbation de la gravité électrique. Cette rétroaction a tendance à stabiliser l'état conductif. Donc, pour que la convection se développe, la force thermoélectrique doit surmonter non seulement la dissipation visqueuse de l'énergie mais aussi la stabilisation de la rétroaction. Par conséquent, les paramètres critiques sont différents de ceux de l'instabilité de RB. La composante de la force thermoélectrique liée à la gravité électrique perturbée pénalise aussi l'écoulement convectif dans son régime non linéaire : la convection est affaiblie et le transfert de chaleur est moins efficace en comparant avec la convection RB.

Les travaux présentés dans ce chapitre ont été réalisés en 2012 au Laboratoire Ondes et Milieux Complexes au Havre en collaboration avec Mireille Tadie Fogaing, Olivier Crumeyrolle et Innocent Mutabazi. Les résultats obtenus ont été communiqués dans plusieurs conférences et dans des séminaires. Ils ont été publiés dans *Eur. Phys. J. E* [28] et *Phys. Rev. E* [101]. Ces articles sont inclus dans l'Annexe C.

Chapitre 3. Convection TEHD dans une géométrie annulaire cylindrique

La convection TEHD dans une géométrie annulaire cylindrique a intéressé des géophysiciens en raison de la similitude de cet écoulement avec certains écoulements géophysiques. Des études existantes sur la convection TEHD dans une géométrie annulaire cylindrique ont concerné seulement des perturbations axisymétriques pour les petits entrefers (c.-à-d., le rapport des rayons $\eta \gtrsim 0,9$). En élargissant la plage des paramètres, nous considérons différentes configurations de la gravité électrique de base (Voir Fig. 1.1 récapitulant les configurations). La relation étroite entre la stabilité de l'état conductif et la gravité électrique de base est montrée. L'instabilité se produit uni-

quement dans les Zones I et IV, où la gravité électrique se dirige dans le même sens que le gradient de température imposé à travers la couche de fluide. Il est aussi montré que le mode critique est toujours non-axisymétrique. L'hypothèse de perturbations axisymétriques aboutira à la surestimation du seuil d'instabilité, en particulier, dans le cas de petit η . Nous analysons aussi le processus de transfert d'énergie à partir de l'écoulement de base à l'écoulement de perturbation grâce à une équation sur l'évolution de l'énergie cinétique (Eq. 2.5). Selon l'analyse, l'analogie gravito-EHD est exacte pour petites valeurs de η , où l'effet stabilisant de la gravité électrique de perturbation est négligeable. Cette conclusion valide l'application géophysique de la convection TEHD.

Ce travail a été réalisé en 2012 au Laboratoire Ondes et Milieux Complexes au Havre en collaboration avec Satish Malik, Olivier Crumeyrolle et Innocent Mutabazi. Les résultats ont été présentés dans plusieurs conférences et publiés dans *Acta Astronaut.* [55] et *Phys. Fluides* [100]. Ce dernier est inclus dans l'Annexe C.

PARTIE II. Ecoulements de Couette-Taylor soumis à des forces thermiques radiales

Chapitre 4. Ecoulement de Couette-Taylor soumis à un gradient de température radial

Le problème de la stabilité d'un écoulement de Couette circulaire, dans l'entrefer de deux cylindres concentriques verticaux et soumis à un gradient de température radial, est réexaminé par une analyse de stabilité linéaire. L'analyse clarifie le rôle de la force de flottabilité due à l'accélération centrifuge. Pour de petites valeurs du paramètre $F = \nu / \sqrt{gd^3}$, l'effet de cette force est négligeable en comparant avec la poussée d'Archimède thermique. La stabilité du système est indépendante de la direction de chauffage, comme prédit par Ali & Weidman [1]. Le chauffage stabilise l'état conductif pour une petite différence de température ΔT . Pour de grandes valeurs de F , la force de flottabilité centrifuge influence de manière significative le comportement du système. La stabilité est sensible à la direction de chauffage : à petit ΔT , le système est plus stable dans un gradient de température positif que dans celui négatif.

L'analyse montre également que la force de flottabilité centrifuge modifie de façon significative la nature des modes critiques. Même en l'absence d'advection par la vitesse axiale de l'écoulement de base (c.-à-d., quand $|Gr|$ est petit), des modes axisymétriques oscillatoires peuvent se développer à partir de l'état conductif sous un gradient de température négatif. La fréquence de ces modes est donnée par la fréquence de Brunt-Bäisälä basée sur l'accélération centrifuge. Ce résultat indique une relation étroite des modes d'oscillation avec les ondes internes se propageant dans une couche fluide stratifiée.

Cette étude théorique sur la stabilité de l'écoulement de Couette-Taylor non isotherme a été menée en 2013 en collaboration avec Antoine Meyer (LOMC), Innocent Mutabazi (LOMC), and Masato Nagata (Université de Tianjin). Certains résultats ont été communiqués dans différentes conférences et publiés dans *Phys. Fluides* [105]. Ce dernier article est inclus dans l'Annexe C.

Chapitre 5. Ecoulement de Couette-Taylor soumis à une force thermoélectrique radiale

La stabilité d'un écoulement de Couette-Taylor soumis à un gradient de température et aussi à une force radiale de flottabilité due à la gravité électrique \mathbf{g}_e est étudiée par la théorie de la perturbation linéaire. La théorie prend en compte une autre force de flottabilité due à l'accélération centrifuge \mathbf{g}_c . Il est montré que le comportement de l'écoulement est sensible à la direction de chauffage. Différents régimes de l'instabilité sont distingués : le mode critique peut être axisymétrique oscillant (OA), soit à forte flottabilité thermoélectrique (c.-à-d., à grande valeur du nombre de Rayleigh électrique $|L|$) sous un gradient de température positif ou à faible flottabilité thermoélectrique (c.-à-d., à petit $|L|$) sous un gradient de température négatif dans un liquide à grand nombre de Prandtl. Dans ce régime OA, l'instabilité est provoquée par la force centrifuge comme dans l'instabilité de Taylor. L'effet net de ces

deux forces de flottabilité thermique stabilise l'écoulement de base et produit l'oscillation du mode critique. La fréquence du mode critique est donnée par la fréquence de Brunt-Väisälä (Eq. 5.2), basée sur les deux forces de flottabilité, qui caractérise les ondes internes se propageant dans une couche fluide stratifié.

Ce résultat sur la relation entre modes critiques OA et ondes internes est une généralisation de la relation étroite trouvée dans notre étude sur l'écoulement Couette-Taylor non-isotherme dans le Chap. 4. Dans le dernier système, la force de flottabilité centrifuge génère des modes OA uniquement dans un gradient de température négatif, puisque, seulement dans cette configuration, la stratification thermique de la masse volumique est stable dans le champ d'accélération centrifuge \mathbf{g}_c et peut ainsi permettre la propagation des ondes. Dans l'écoulement de Couette-Taylor considéré dans le présent chapitre, la stratification peut également permettre des ondes dans un gradient de température positif si la force de flottabilité due à la gravité électrique \mathbf{g}_e est supérieure à celle due à l'accélération centrifuge \mathbf{g}_c . Nous pourrions espérer la génération d'ondes similaires dans d'autres systèmes de Couette-Taylor non-isothermes, comme celui d'un ferrofluide soumis à un champ électrique.

Ce travail a été commencé en 2013 en collaboration avec Antoine Meyer (LOMC) et Innocent Mutabazi (LOMC). Les résultats obtenus ont été présentés dans plusieurs conférences et publiés dans *Phys. Rev. E* [104]. Cet article est inclus dans l'Annexe C.

PARTIE III. Ecoulements avec des bulles

Chapitre 6. Stabilité de bulles dans un écoulement oscillant

La stabilité d'une bulle à taille centimétrique dans un écoulement oscillant est étudiée par des expériences en micro-pesanteur. La scission de la bulle se produit à une accélération constante $A\omega^2$ dans un liquide donné. L'analyse de la translation de la bulle et l'analyse sur le seuil de scission de bulle révèlent que le critère inertiel $We > 12$ (c.-à-d., Eq. 6.7) explique bien les résultats expérimentaux. Ce mécanisme inertiel de la scission est indépendante de la viscosité du liquide et le critère prédit que la scission se produit à une vitesse constante U_b de la bulle pour une taille de bulle donnée et dans un liquide donné. La viscosité du liquide, cependant, influence le mouvement de la bulle : dans un liquide visqueux, la bulle se déplace avec un amplitude d'oscillation $A_b = U_b/\omega$ faible (Eq. 6.2) et, par conséquent, avec une petite vitesse U_b . Ainsi, la bulle est plus stable dans un liquide plus visqueux, comme nous l'avons observé dans les expériences (Fig. 6.5).

En provoquant la scission par un écoulement oscillant, on peut contrôler la taille de bulles dans un écoulement diphasique liquide-gaz. Selon le critère (Eq. 6.4) obtenu dans nos études expérimentales, on peut briser des bulles plus grandes que

$$D_e = 1.27 \sqrt{\frac{\sigma^{0.846} \nu^{0.229}}{\rho^{0.846} A^{0.995} f^{1.92}}} \approx 8.0 \ell'_{cap} \left(\frac{\rho^2 \nu^3 f}{\sigma^2} \right)^{0.017} \quad (0-1)$$

par un écoulement oscillant, où ℓ'_{cap} est la longueur capillaire basée sur l'accélération de l'écoulement oscillant. Ce résultat confirme les résultats précédents reportés dans Zoueshtiagh et al. [110] et les généralise pour différents liquides avec différentes viscosités.

Ce travail a été réalisé en collaboration avec Farzam Zoueshtiagh (IEMN, Lille), Hervé Caps (GRASP, Liège), Pascal Kurowski (PMMH, Paris) et Philippe Petitjeans (PMMH, Paris). Les résultats ont été communiqués dans plusieurs conférences et publiés dans *Microgravity Sci. Technol.* [98] et *Eur. Phys. J. E* [108]. Ce dernier article est inclus dans l'Annexe C.

Chapitre 7. Dynamique de bulles en micropesanteur

La dynamique d'une bulle de vapeur isolée dans un écoulement pariétal est étudiée par une expérience en micropesanteur. La mesure optique du mouvement de la bulle est effectuée afin d'estimer les différentes forces exercées sur la bulle au site de nucléation sur la paroi chauffante. Les forces calculées confirment l'équilibre des forces pendant le développement de la bulle et suggère que le départ de la bulle à partir du site de nucléation pourrait être associé avec la rupture de l'équilibre des forces. La modélisation de la dynamique des bulles de vapeur par l'équilibre des forces est donc une façon prometteuse pour prédire le comportement des bulles de vapeur. Il est cependant nécessaire d'affiner les modèles de forces, parce que l'accord quantitatif entre le modèle et l'expérience n'est pas satisfaisant.

Ce travail a été réalisé en collaboration avec Catherine Colin (IMFT, Toulouse) et Cees van der Geld (Université de technologie d'Eindhoven). Les résultats ont été communiqués dans différents conférences et publiés dans les actes de conférences internationales [49,99] ainsi que dans *Phys. Fluides* [92].

Chapitre 8. Formation de motifs spiralés dans un système liquide-gaz simple

La formation de motifs exposés par des bulles émergeant périodiquement à partir de la surface libre d'un liquide est étudiée par une expérience avec un système diphasique liquide-gaz simple. L'observation expérimentale du comportement des bulles montre que l'interaction bulle-bulle dans une bosse de la surface (apex) joue un rôle décisif dans la formation de motif. Cela indique l'analogie avec le développement méristématique au sommet de la pousse d'une plante qui conduit à un arrangement régulier des feuilles, appelé *phyllotaxie*. Un modèle théorique simple est développé pour notre système diphasique. Le modèle se base sur l'équilibre des forces sur chaque bulle et prend en compte l'advection des bulles par l'écoulement du liquide et l'interaction bulle-bulle, les deux influençant la compaction de bulles dans l'apex. Le modèle peut reproduire le comportement de l'angle de divergence ψ observé dans l'expérience, en particulier, la transition entre le régime distique et le régime spiral.

Cette recherche a été réalisée en collaboration avec Christian Mathis, Philippe Maïssa et Germain Rousseaux du Laboratoire J.-A. Dieudonné, ainsi qu'avec Stéphane Douady (MSC, Paris). Les résultats ont été publiés dans *Eur. Phys. J. E* [103] et dans un livre des actes d'un colloque [102]. Le premier article est inclus dans l'Annexe C.

Contents

| | |
|---|-----------|
| Preface | i |
| Acknowledgements | iii |
| Introduction générale – Traduction en français de General Introduction (pp. 1–4) | v |
| Résumés en français des Chapitres 1–8 | ix |
| | |
| General Introduction | |
| Scientific career | 1 |
| Current research | 3 |
| Organization of manuscript | 3 |
| | |
| I Thermo-electrohydrodynamic (TEHD) instability | |
| | |
| 1 Gravito-EHD analogy | 5 |
| 1.1 Introduction | 5 |
| 1.2 EHD force | 7 |
| 1.3 Governing equations of the TEHD convection | 8 |
| 1.4 Electric gravity in elementary electrode configurations | 9 |
| 1.5 Control parameters and nondimensionalized governing equations | 12 |
| | |
| 2 TEHD convection in plane geometry | 13 |
| 2.1 Introduction | 13 |
| 2.2 Linear stability analysis | 14 |
| 2.3 2D numerical simulation | 18 |
| 2.4 Heat transfer | 21 |
| 2.5 Conclusion | 21 |
| | |
| 3 TEHD convection in cylindrical annular geometry | 23 |
| 3.1 Introduction | 23 |
| 3.2 Linear stability analysis | 25 |
| 3.3 Conclusion | 29 |
| | |
| II Taylor-Couette flow with radial thermal body forces | |
| | |
| 4 Taylor-Couette flow with a radial temperature gradient | 31 |
| 4.1 Introduction | 31 |

| | | |
|------------------------------|--|-----------|
| 4.2 | Conductive state | 34 |
| 4.3 | Linear stability analysis | 35 |
| 4.4 | Conclusion | 40 |
| 5 | Taylor-Couette flows subjected to radial thermoelectric buoyancy | 41 |
| 5.1 | Introduction | 41 |
| 5.2 | Linear stability theory | 44 |
| 5.3 | Analysis | 47 |
| 5.4 | Conclusion | 49 |
| III Flow with bubbles | | |
| 6 | Stability of bubbles in oscillatory flow | 51 |
| 6.1 | Introduction | 51 |
| 6.2 | Results | 53 |
| 6.3 | Discussion on the splitting mechanism | 54 |
| 6.4 | Conclusion | 56 |
| 7 | Vapor bubble dynamics in microgravity environments | 57 |
| 7.1 | Introduction | 57 |
| 7.2 | Experiments | 59 |
| 7.3 | Conclusions | 62 |
| 8 | Formation of spiral patterns in a simple liquid-gas system | 63 |
| 8.1 | Introduction | 63 |
| 8.2 | Experiments | 64 |
| 8.3 | Theoretical model | 66 |
| 8.4 | Conclusion | 68 |
| Perspectives | | |
| | Research project for coming years | 69 |
| Bibliography | | |
| 71 | | |
| Appendixes | | |
| A | Curriculum vitae | 79 |
| B | List of Publications | 83 |
| C | Selected articles published in international journals | 89 |
| | <i>Dielectrophoretic Rayleigh-Bénard convection under microgravity conditions (Phys. Rev. E, 2013)</i> | 91 |
| | <i>Heat transfer in the thermo-electro-hydrodynamic convection under microgravity conditions (Eur. Phys. J. E, 2014)</i> | 99 |
| | <i>Dielectrophoretic force-driven thermal convection in annular geometry (Phys. Fluids, 2013)</i> | 105 |

CONTENTS

Instability of the vertical annular flow with a radial heating and rotating inner cylinder (Phys. Fluids, 2013) 119

Linear stability of a circular Couette flow under a radial thermoelectric body force (Phys. Rev. E, 2015) 133

Bubble splitting in oscillatory flows on ground and in reduced gravity (Eur. Phys. J. E, 2010) . . . 145

Pattern formation in bubbles emerging periodically from a liquid free surface (Eur. Phys. J. E, 2010) 155

General Introduction

Scientific career

PhD and Postdoctoral experiences

I graduated from the Department of Electronics at Doshisha University in Kyoto, Japan in March 2000. I did my master in electrical engineering at the same university (April 2000 – March 2002), doing my master research on the dynamics of non-neutral plasma in the Applied Physics Laboratory under the supervision of Prof. Motoi Wada and Dr. Toshiro Kasuya. My research was concerned with the effects of molecular diffusion on the velocity profile of an electron gas jet. During this master course, I was selected for a student exchange program between the Faculty of Engineering of the university and the Ecole Supérieure de Physique et de Chimie Industrielles (ESPCI) in Paris. I was thus able to do my internship in the laboratory Physique et Mécanique des Milieux Hétérogènes (PMMH) with Dr. José Eduardo Wesfreid (Septembre 2000 – July 2001). I worked for the first time on hydrodynamic stability problems, analyzing the Rosensweig instability of the free surface of a ferrofluid layer in a magnetic field.

After obtaining the master degree, I started in 2002 my scientific career, preparing my PhD thesis at PMMH under the supervision of Dr. Wesfreid. At the beginning of my PhD research I was interested in the stability of the surface of granular material sheared by viscous liquid and worked on the formation of sand ripples under oscillatory flow [67]. I learned to solve a stability problem for an unsteady base state by developing a numerical code. Then, I turned to an analogous problem for an immiscible liquid-liquid interface, where tangential oscillatory shear provokes an instability to form ripples at the interface [102, 103]. This problem had been investigated less compared with the stability of a liquid free surface subjected to vertical vibration, i.e., the Faraday instability problem. I performed linear stability analyses and compared results obtained from the experiments that I had designed and performed. My thesis, consisting of these works and entitled “Instabilités des interfaces sous oscillations,” was defended in 2006 in front of the jury composed of Prof. Stéphane Zaleski, Prof. Tatyana Lyubimova, Prof. Philippe Gondret, Prof. Innocent Mutabazi, and Dr. José Eduardo Wesfreid.

After the thesis I worked as a postdoctoral research fellow with different researchers in different laboratories in France. First, I joined a research team of Dr. Philippe Petitjeans and Dr. Pascal Kurowski at PMMH and investigated the stability of bubbles in oscillatory flow in microgravity environments (February 2007 – August 2007). Collaborating with Dr. Farzam Zoueshtiagh (IEMN, Lille) and Dr. Hervé Caps (Université de Liège), I realized experiments and analyzed the results in order to characterize the stability and to reveal the mechanism of observed bubble splitting. We showed that the size of stable bubbles was limited by the capillary length based on the acceleration of oscillatory flow and that the inertia of liquid flow was responsible for the bubble splitting [94, 104].

After this first experience in microgravity science I obtained a postdoctoral fellowship from the CNES (Centre National d’Etudes Spatiales) to work with Prof. Catherine Colin at Institut Mécanique des Fluides in Toulouse for an experimental project on nucleate boiling in microgravity environments (September 2007 – August 2009). I designed and performed experiments, participating in two parabolic flight campaigns, one organized by the CNES and the other by the European Space Agency [88, 95]. We developed a mechanical model of the dynamics of a single vapor bubble growing and moving on a heated wall. We examined this model by comparing it with experimental measurements. These two postdoctoral experiences have made me familiar with topics and problems in microgravity technologies.

In September 2009, I moved to Nice for another postdoctoral research fellowship and joined a research team of Dr. Christian Mathis, Dr. Philippe Maïssa and Dr. Germain Rousseaux at Laboratoire J.-A. Dieudonné (September 2009 – December 2011). We were interested in a pattern formation in a liquid-gas two phase flow system that seemed to be similar to the phyllotaxis, i.e., the formation of the regular arrangement of leaves around a stem

of a plant. By experiments and theoretical modeling, we showed that the mechanism of the pattern formation was similar to that proposed for the phyllotaxis [98, 99]. During some months at the end of this postdoctoral fellowship, I also worked on a subject about the nucleate boiling. I investigated the temperature field surrounding a vapor bubble growing on a heated surface by applying the two-color laser induced fluorescence thermometry [42]. My final experience as a postdoctoral research fellow was in Le Havre (January 2012 – August 2013) with Prof. Innocent Mutabazi at Laboratoire Ondes et Milieux Complexes (*LOMC*). The first year was devoted to a theoretical analysis of thermal convection of dielectric fluid in an electric field. This convection, called *the thermo-electrohydrodynamic (TEHD) convection*, is induced by a component of the electrohydrodynamic force. For research on this subject, I also collaborated with Dr. Olivier Crumeyrolle. By linear stability analyses, we established the criteria for convection to develop in different configurations of electrodes [52, 96, 97]. We also computed heat transfer by a direct numerical simulation in a particular geometry. During the final 8 months, I worked on the stability of a Taylor-Couette flow in radial heating to clarify the effects of the radial temperature gradient on the flow stability [101]. I also considered a similar problem but with a radial electric field and found that the radial thermal forces could generate waves [100]. At the end of this postdoctoral position, I started to work on the heat transfer in Görtler vortices developed on a concave wall surface in collaboration with Dr. Jorge Peixinho. We developed a theoretical model that took into account the finite thermal conductivity in the wall [36].

Developing my scientific career as a researcher, I also taught science either by supervising researches or by giving courses. I supervised research internships of undergraduates and master students in different laboratories (see appendix A for details). I also participated in research training of PhD students during my stay in Nice and in Le Havre. When I worked in Toulouse, I gave courses of automatics (Analog control systems, Digital control systems) to undergraduates as well as to engineers at the Department of Electronics of the Institut Catholique d'Arts et Métiers.

After these research and teaching experiences, I obtained in 2013 a position of Maître de Conférences of the section 60 (Mechanics, Mechanical Engineering, Civil Engineering) of the CNU¹ at Université Nice Sophia Antipolis (*UNS*).

Current Position at Université Nice Sophia Antipolis

Since September 2013, I am a Maître de Conférences at Université Nice Sophia Antipolis. I'm attached to the engineering school, *École Polytechnique Universitaire Nice Sophia*, and give courses to the first year students of the Department of Buildings. I teach currently *General Mechanics*, *Thermodynamics*, *Numerical Methods*, and *Fluid Mechanics*. They form the basis for students to master courses more specialized to building engineering. I'm responsible for the first year program, being the director of studies for the first year students. I also take a responsibility for the department to be certified for ISO 9001.

For research I work at the laboratory J.-A. Dieudonné, where I did one of my postdoctoral positions. I'm integrated to the research team *Numerical Modeling and Fluid Dynamics* headed by Prof. Didier Clamond. I'm a member of experimental fluid mechanics group in it, consisting of Dr. Christian Mathis, Dr. Philippe Maïssa and Dr. Pascal Henry Biwole.

¹Conseil National des Universités (National Council of Universities)

Current research

My current research activities are concentrated on electrohydrodynamic (EHD) instabilities of non-isothermal flows. The investigation is motivated by the analogy between a thermal EHD force and the thermal Archimedean buoyancy. Using this analogy one can simulate a certain class of geophysical flows by laboratory experiments. The research is also motivated by potential application of the thermal EHD force to thermal management systems working in microgravity conditions and to microfluidic devices. I have been familiar with flows driven by the thermal EHD force since my postdoctoral experience in Le Havre. Continuing the collaboration with the LOMC group in Le Havre and developing a collaboration with Prof. Masato Nagata of Tianjin University in Tianjin, China, I am performing theoretical analyses of the thermal EHD flows generated either in a plane parallel capacitor or in a cylindrical annular capacitor. Since my arrival at Nice in September 2013, I have applied for different calls for projects of CNRS and ANR with research proposals on this subject. One of these proposals was selected and I obtained a financial support from CNRS (Projet Exploratoire Premier Soutien – Physique Théorique et ses Interfaces) in 2014. My university also supports the project by funding collaboration with Prof. Nagata in 2014 and 2015.

I'm also working for other two subjects. The first one is concerned with the Rayleigh-Bénard convection with injected vapor bubbles. The investigation is motivated by importance of the heat transfer enhancement by two-phase flow systems in industries. The goal is to improve by experimental studies our current understanding on the thermal and mechanical effects of vapor bubbles on flow and global heat transfer. In particular, the thermal and mechanical interaction between bubbles and thermal plumes in highly non-linear flow regimes will be investigated. This research, carried out with one of my colleagues, Dr. Christian Mathis, is supported by UNS. It is a part of a collaboration project with Prof. Thierry Coupez (Institut du Calcul Intensif, Nantes) and Dr. Séverine Boyer (PPRIME, Poitiers), who perform numerical simulation and theoretical modeling.

The second subject is the wetting of a solid surface in the presence of submillimeter-sized particles. The dynamical behavior of contact lines on a surface contaminated by particles is investigated by experimental, theoretical, and numerical approaches. The research is motivated by self-cleaning property of solid surfaces, which pertains to many industrial applications. This research has just started in the framework of an international collaboration project coordinated by Prof. Farzam Zoueshtiagh (IEMN, Lille) and Prof. Ichiro Ueno (Tokyo University of Science, Japan), with a financial support from CNRS and JSPS². Experiments are performed at IEMN and Tokyo University of Science by using existing experimental facilities. I work for theoretical modeling of the contact line behavior and also perform analysis of experimental data in collaboration with other partners in France and in Japan.

Organization of manuscript

Writing the present manuscript, I tried to summarize essential scientific results that I had obtained since completion of my PhD. I did four postdoctoral positions so that the subjects are varied. The manuscript focus, however, to the electrohydrodynamic instabilities, as my research for coming years will be concentrated to this topic.

Part I is concerned with the TEHD convection. The basis of theoretical modeling of this EHD flow is given in Chap. 1, with underlining the analogy between a thermal EHD force and the thermal Archimedean force due to the gravity. Chapter 2 deals with the TEHD instability and the resulting convection in a fluid layer between two plane parallel electrodes. Chapter 3 is concerned with the TEHD instability in cylindrical annular geometry, where a fluid layer is subjected to an electric field applied by two concentric cylindrical electrodes. Part II is devoted to the stability of Taylor-Couette flows in radial heating. A vertical Taylor-Couette system is considered in Chap. 4.

²Japan Society for the Promotion of Science

In Chap. 5, a system subjected also to a radial electric field is considered in microgravity conditions. Part III contains three experimental investigations on different flows with bubbles. The results on the stability of a bubble in oscillatory flow, the behavior of a vapor bubble on a heated wall in a shear flow, and the pattern formation of bubbles on a free surface are presented in Chaps. 6, 7, and 8, respectively. A research project for coming years is given in Part 8.4.

Part I

Thermo-electrohydrodynamic (TEHD) instability

Chapter 1

Gravito-EHD analogy

The first part of the present manuscript is concerned with a thermal convection, called *the thermo-electrohydrodynamic (TEHD) convection*, induced by an electrohydrodynamic force. In the present chapter, the general basis for the theoretical analysis of this convection is given. The analogy of the driving force of the TEHD convection with the thermal Archimedean force is pointed out by introducing the concept of the electric gravity in Sec. 1.1. After discussing the necessary conditions for neglecting other effects of applied electric fields on fluid motion in Sec. 1.2, the governing equations of the TEHD convection are presented in Sec. 1.3. Section 1.4 is devoted to a summary of the conductive states of fluid in three particular electrode configurations. In Sec. 1.5, the dimensionless numbers characterizing the TEHD convection are introduced with a nondimensionalized governing equations.

1.1 Introduction

Interaction of fluids with electromagnetic fields is an important subject in different scientific fields and modern technologies. Micro-encapsulation process in electric fields for biomedical application and levitation of liquid metal drops for metallurgical operations are examples at small scales where the interaction provides means of control of fluid motion. The control of plasma in a nuclear fusion reactor by magnetic fields is another example but at larger scale. Magneto rotational instabilities regarded as the mechanism of angular momentum transport in an accretion disk is an example at galaxy scales.

The electrohydrodynamics (EHD) is concerned with the mechanics of electrically poorly conducting fluids and dielectric fluids in electromagnetic fields. The time and length scales, τ , ℓ , of their flows are assumed to satisfy the following conditions:

$$\tau, \tau_e \gg \tau_{em}, \quad (1-1)$$

where $\tau_e = \epsilon/\sigma_e$ is *the charge relaxation time* characterizing the charge accumulation process through electrical conduction in the fluid (σ_e , ϵ : the electrical conductivity and the dielectric permittivity of the fluid, respectively). The length scale ℓ is involved in *the electromagnetic transit time* $\tau_{em} = \ell/c$, where c is the speed of light. Under the conditions (1-1), electromagnetic fields can be analyzed in the electroquasistatic approximation and the force exerted by the field on the fluid can be computed from the EHD stress tensor that is independent from the magnetic field (Sec. 1.2).

The EHD force is used widely for manipulating dispersed phases (i.e., bubbles, drops and particles), e.g., in pollution control [90], levitation, powder deposition, and other applications in biomedical fields. The EHD force is also used to control and pump single-phase flow. Since strong EHD force can be generated by a reasonable value of electric tension at small scales, the use of EHD effects to transport mass, momentum, and energy in fluid

Table 1.1: Properties of some electrically poorly conducting and dielectric fluids

| | ρ [kg/m ³] | ν [10 ⁻⁶ m ² /s] | σ_e [10 ⁻⁶ S/m] | ϵ_r [-] | $\alpha = \frac{1}{\rho} \left(\frac{d\rho}{dT} \right)$ [10 ⁻³ K ⁻¹] | $e = \frac{1}{\epsilon} \left(\frac{d\epsilon}{dT} \right)$ [10 ⁻³ K ⁻¹] | Pr [-] | Polarity [-] |
|---------------|---------------------------------|---|--|-----------------------|---|--|-------------|-------------------|
| Acetonitrile | 777 | 0.439 | 700 | 36.0 | 1.38 | 155 | 4.7 | 5.8 |
| Nitrobenzene | 1198 | 1.52 | 0.5 | 34.7 | 0.83 | 188 | 19 | 4.5 |
| Acetone | 785 | 0.386 | 6 | 19.1 | 1.43 | 86 | 4.2 | 5.1 |
| Chlorobenzene | 1101 | 0.686 | – | 5.61 | 0.985 | 15.7 | 7.9 | 2.7 |
| Cyclohexane | 774 | 1.17 | < 10 ⁻⁶ | 2.02 | 1.22 | 1.60 | 14 | 0.2 |
| Silicone oil | 920 | 5.0 | < 10 ⁻⁶ | 2.70 | 1.08 | 1.065 | 59.9 | – |
| Silicone oil | 968 | 99.2 | < 10 ⁻⁶ | 2.73 | 0.96 | 3.2 | 910 | – |

is common practice in microfluidics. μ TAS (micro total-analysis systems) and MEMS (microelectromechanical systems) are the area where the EHD forces can play important roles.

The *dielectrophoresis* is one of the manipulation techniques of dispersed phases by a component of the EHD force, called the *dielectrophoretic (DEP) force*, that results from the difference in polarization between the dispersed phases and the surrounding continuous phase [58]. For a spherical particle of radius a that is small compared with the length scale of the electric field spatial variation, the DEP force is given by

$$\mathbf{F}_{DEP} = 2\pi a^3 \epsilon_{ref} K_{CM} \nabla \mathbf{E}^2, \quad (1-2)$$

where ϵ_{ref} is the dielectric permittivity of the continuous phase [35, 61]. The coefficient K_{CM} is the *Clausius-Mossotti factor*: $K_{CM} = (\epsilon - \epsilon_{ref})/(\epsilon + 2\epsilon_{ref})$, where ϵ is the permittivity of the particle. The DEP force (1-2) can also act on a fluid particle of the same fluid as the continuous phase, if the particle has a different temperature from the surrounding fluid. This thermal DEP force has an interesting feature: it behaves in a similar way to the thermal Archimedean buoyancy. This gravito-EHD analogy enables us to introduce an electric effective gravity. The dielectric permittivity varies with temperature. For a small temperature variation, its behavior can be modeled by the linear equation:

$$\epsilon = \epsilon(T) = \epsilon_{ref} (1 - e\theta), \quad (1-3)$$

where θ is the deviation of the fluid temperature T from a reference temperature T_{ref} : $\theta = T - T_{ref}$. The coefficient e is positive except for some polar liquids (e.g., acetic and butyric acids). It takes a value of the order of 10⁻³ K⁻¹ for non-polar fluids, of 10⁻²-10⁻¹ K⁻¹ for polar fluids (Table 1.1). The thermal DEP force on a spherical fluid particle is computed by substituting Eq. (1-3) to Eq. (1-2). The Clausius-Mossotti factor is given by $K_{CM} = -e\theta/3$, leading to the following expression of the DEP force:

$$\mathbf{F}_{DEP} = -\frac{2\pi}{3} a^3 e\theta \epsilon_{ref} \nabla \mathbf{E}^2 = -\frac{4\pi}{3} a^3 \rho \alpha \theta \mathbf{g}_e, \quad (1-4a)$$

$$\text{with } \mathbf{g}_e = \frac{e}{\alpha\rho} \nabla \left(\frac{\epsilon_{ref} \mathbf{E}^2}{2} \right). \quad (1-4b)$$

The coefficient of thermal expansion α has been introduced. The last term in Eq. (1-4a) takes the same form as the thermal Archimedean buoyancy force on a spherical particle but in an effective gravity field \mathbf{g}_e . This gravito-EHD analogy is useful to understand the effects of \mathbf{F}_{DEP} on fluid motion. One may expect that thermal convection would develop if the electric gravity were directed from low to high temperature zones of a fluid layer. This convection is indeed known as the *thermo-electrohydrodynamic (TEHD) convection*. The heat transfer enhancement by this convection is expected to reduce the weight and volume of thermal systems. This electrohydrodynamically induced

convection is hence of great importance for aeronautical and astronomical heat exchanger components [57, 73].

The concept of the electric gravity can enable us not only to understand the effects of the thermal DEP force on fluid motion in the light of the analogy with the thermal Archimedean buoyancy, but also to simulate some large-scale geophysical flows by EHD laboratory experiments. For understanding geophysical flows, laboratory experiments are often desired to check theoretical ideas. For thermal convection at planetary scales, the Rayleigh number is huge, e.g., it is of the order of 10^7 for the convection in the Earth's mantle [72]. The flow is highly nonlinear and the approach by direct numerical simulations to the problem is limited. One can use an EHD laboratory experiment to simulate experimentally such geophysical flows.¹ For this aim, the electric gravity should be isotropic and centripetal, similar to the Earth's gravity. We can realize such an electric gravity field by using two concentric spherical electrodes maintained at different temperatures and different electrostatic potentials (Sec. 1.4).

Attempts of geophysical flow simulations by EHD experiments have been made in different geometries and in different gravity conditions. To the best of my knowledge, Chandra & Smylie [11] were the first who studied experimentally the TEHD convection to simulate geophysical flows. They performed experiments with two concentric cylindrical electrodes on the ground. Later, TEHD convection experiments for geophysical flows were performed rather in microgravity environments. In fact, the Earth's gravity is undesired, since it can induce spurious fluid motions in a tentative of establishing a radial temperature gradient. Sitte et al. [73] and Dahley et al. [21] performed experiments in cylindrical geometries in a drop tower and during parabolic flights, respectively. Hart et al. realized experiments in semi-spherical geometry on board of the space shuttle Challenger [31]. Recently, the GEOFLOW experiments were realized in the science laboratory Columbus on board of the International Space Station (ISS) [28].

1.2 EHD force

The EHD force has components other than the DEP force. For the gravity-EHD analogy, these components should be negligible in fluid dynamics. In general, the EHD force consist of a component \mathbf{F}_E arising from the Coulomb forces on free charges (i.e., ions, charged impurities suspended in the fluid) and a dielectric component \mathbf{F}_D due to the polarization of fluid. Free charges accelerated by the Coulomb forces transfer their momentum to surrounding electroneutral molecules through collisions. The fluid is thus subjected to the force $\mathbf{F}_E = \rho_e \mathbf{E}$ per unit volume in macroscopic view. The dielectric force \mathbf{F}_D is computed from the dielectric stress tensor σ_D , which is obtained from the Maxwell's stress tensor by replacing the permittivity of vacuum ϵ_0 by the dielectric permittivity ϵ and by adding an electrostriction component. In dyadic representation, the tensor is given by

$$\sigma_D = \epsilon \mathbf{E} \mathbf{E} - \frac{\epsilon \mathbf{E}^2}{2} \mathbf{I} + \frac{\rho}{2} \left(\frac{\partial \epsilon}{\partial \rho} \right)_T \mathbf{E}^2 \mathbf{I}, \quad (1-5)$$

where the first two terms in the right-hand-side correspond to the Maxwell's tensor and the last term represents the electrostriction effect [45, 54]. The second-order unit tensor is denoted by \mathbf{I} . The total EHD body force density $\mathbf{F}_{EHD} = \mathbf{F}_E + \mathbf{F}_D$ is given by [34]

$$\mathbf{F}_{EHD} = \rho_e \mathbf{E} - \frac{1}{2} \mathbf{E}^2 \nabla \epsilon + \nabla \left[\frac{\rho}{2} \left(\frac{\partial \epsilon}{\partial \rho} \right)_T \mathbf{E}^2 \right]. \quad (1-6)$$

¹One can also realize such experimental simulation of geophysical flows with non-isothermal ferrofluid in magnetic fields [56, 66, 80, 7].

When the variation of the permittivity ϵ arises only from thermal effects, we can cast the EHD force (1-6) into a form revealing the gravito-EHD analogy. Substituting Eq. (1-3) into Eq. (1-6), we have

$$\mathbf{F}_{EHD} = \rho_e \mathbf{E} - \nabla p_{EHD} - \rho \alpha \theta \mathbf{g}_e, \quad (1-7a)$$

$$\text{with } p_{EHD} = - \left[\frac{e \theta \epsilon_{\text{ref.}} \mathbf{E}^2}{2} + \frac{\rho}{2} \left(\frac{\partial \epsilon}{\partial \rho} \right)_T \mathbf{E}^2 \right], \quad (1-7b)$$

$$\mathbf{g}_e = \frac{e}{\rho \alpha} \nabla \left(\frac{\epsilon_{\text{ref.}} \mathbf{E}^2}{2} \right), \quad (1-7c)$$

where p_{EHD} is the EHD pressure that can be lumped with the hydrodynamic pressure p in the momentum equation. The last term of Eq. (1-7a) is the generalization of the thermal DEP force (1-4a) on a spherical fluid particle to continuous fluid. It confirms the gravito-EHD analogy. Indeed, it has the same form as the thermal Archimedean buoyancy in the Boussinesq approximation. The electric gravity (1-7c) is identical to the earlier definition (1-4b).

In a *d.c.* electric field or an *a.c.* electric field of frequency f smaller than the inverse of the charge relaxation time τ_e , the accumulation of free charges occurs in the fluid where its electric properties vary in space, e.g., at the surface of the fluid and in a zone with a sharp temperature gradient. In general, the Coulomb force \mathbf{F}_E on the accumulated charges have stronger effects on the fluid motion than the dielectric force \mathbf{F}_D .

If the frequency of an *a.c.* field is high compared with the charge relaxation time and the viscous relaxation time $\tau_v = d^2/\nu$, i.e., if

$$f \gg \frac{1}{\tau_e}, \frac{1}{\tau_v}, \quad (1-8)$$

the charge accumulation will not occur (d : the distance between the electrodes; ν : the kinematic viscosity of the fluid). Initially non-charged fluid will remain electroneutral so that the Coulomb force is negligible. Even if the fluid has initially charged in certain zone, no net dynamical effects can arise from the Coulomb force \mathbf{F}_E , since it completes a cycle before the fluid motion is induced and the time average of this force is zero. In contrast, the dielectric force \mathbf{F}_D involves the electric field squared so that it has a non-zero time averaged component. The dielectric force \mathbf{F}_D is hence dominant compared with the Coulomb force in the conditions (1-8).

1.3 Governing equations of the TEHD convection

We consider convection induced by the thermal DEP force, $-\rho \alpha \theta \mathbf{g}_e$ in (1-7a), in a single-phase dielectric fluid between two stationary solid electrodes which are kept at different temperatures T_1 and T_2 with an imposed difference $\Delta T = T_1 - T_2$. For dominance of the dielectric force \mathbf{F}_D over the Coulomb force \mathbf{F}_E , we apply an *a.c.* electric tension $V(t) = \sqrt{2} \Phi_0 \sin(2\pi f t)$ between the electrodes and assume the conditions (1-8). We also assume that the fluid is initially electroneutral everywhere. As no charge accumulation can occur, the latter assumption implies that $\rho_e = 0$ throughout the fluid motion.

For modeling the TEHD convection mathematically, the following continuity, momentum and heat conduction equations can be used [87]:

$$\nabla \cdot \mathbf{u} = 0, \quad (1-9a)$$

$$\rho \left(\frac{\partial \mathbf{u}}{\partial t} + \mathbf{u} \cdot \nabla \mathbf{u} \right) = -\nabla \pi + \rho \nu \nabla^2 \mathbf{u} - \rho \alpha \theta (\mathbf{g} + \mathbf{g}_e), \quad (1-9b)$$

$$\frac{\partial \theta}{\partial t} + \mathbf{u} \cdot \nabla \theta = \kappa \nabla^2 \theta, \quad (1-9c)$$

where π is the generalized pressure $\pi = p + p_{\text{EHD}} + \rho \mathbf{g} \cdot \mathbf{r}$ and κ is the thermal diffusivity of the fluid (\mathbf{g} : the gravitational acceleration of the Earth; \mathbf{r} : the position vector). In Eqs. (1-9a) & (1-9b), the Boussinesq approximation has been adopted, whose validity can be justified by a similar argument for the ordinary thermal convections [87]. The pressure force term, $-\nabla\pi$, and hence the EHD pressure will not affect the fluid motion in this approximation, as it cannot generate any vorticity and the fluid has no mobile boundary. In Eq. (1-9c), the viscous energy dissipation and the ohmic heating have been neglected. These effects, which might appear in the right-hand-side of the equation in the form $(2\rho\nu\dot{\epsilon} : \dot{\epsilon} + \sigma_e \mathbf{E}^2)/(\rho c_p)$, are negligible compared with the thermal conduction [91] (c_p : the specific heat; $\dot{\epsilon}$: the rate-of-strain tensor).

We have the electric gravity in the momentum equation (1-9b), which should be computed from Eq. (1-7c). The electric field \mathbf{E} is required for this computation. It is governed by the Maxwell's equations for \mathbf{E} :

$$\nabla \cdot [\epsilon_{\text{ref}} (1 - e\theta) \mathbf{E}] = 0, \quad (1-10a)$$

$$\nabla \times \mathbf{E} = 0. \quad (1-10b)$$

The thermal permittivity variation (1-3) and the electroneutrality assumption ($\rho_e = 0$) have been taken into account when writing the Gauss' law (1-10a). The Faraday's law (1-10b) implies that the electric field can be computed from an electrostatic potential ϕ : $\mathbf{E} = -\nabla\phi$.

The electric gravity \mathbf{g}_e oscillate in time, as the applied electric voltage is *a.c.* However, due to the viscous filtering of high frequency fluctuations, only the time-averaged component of \mathbf{g}_e affects the motion of the fluid. We can compute directly this time-averaged component of the electric gravity by converting the *a.c.* electric field problem to an equivalent *d.c.* problem. This conversion is made by replacing the actual electric voltage $\sqrt{2}\Phi_0 \sin(2\pi ft)$ imposed between the electrodes by its root-mean-square Φ_0 . The boundary conditions for modeling the TEHD convection are thus given by

$$\mathbf{u} = \mathbf{0}, \quad \theta = \theta_1, \quad \phi = \Phi_0 \quad \text{at } S_1, \quad (1-11a)$$

$$\mathbf{u} = \mathbf{0}, \quad \theta = \theta_2, \quad \phi = 0 \quad \text{at } S_2, \quad (1-11b)$$

where S_1 and S_2 denote the surfaces of the first and second electrodes, respectively. The temperatures of the electrodes are specified by their deviations from the reference temperature: $\theta_1 = T_1 - T_{\text{ref}}$, $\theta_2 = T_2 - T_{\text{ref}}$. This time-averaged description based on the high frequency assumption (1-8) is valid when $2\pi f \gtrsim 100/\tau$, according to a theoretical investigation by Smorodin & Velarde [74].

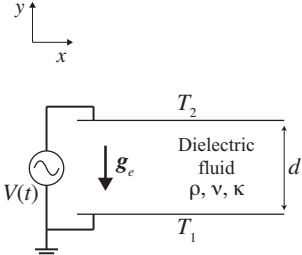
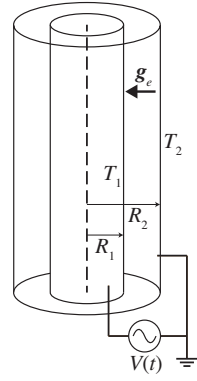
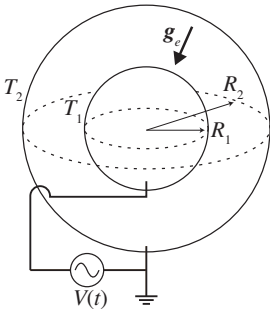
1.4 Electric gravity in elementary electrode configurations

Three geometrical configurations of the electrodes are of particular interest in applications: plane parallel, cylindrical annular and spherical shell geometries (see illustrations in Table 1.2). This section is devoted to the summary of the electric gravity generated in stationary conductive flow states in these geometries. We will denote by ζ a spatial coordinate in the direction normal to the electrode surfaces: ζ means y in the plane geometry (Table 1.2a) and it means the radial coordinate r in cylindrical and spherical configurations (Table 1.2bc).

When the fluid is at rest, thermal energy is transported only by conduction.² In this conductive state, the temperature varies only in the ζ direction: $\theta = \theta(\zeta)$, since the temperature difference is applied by the electrodes. Similarly,

²The fluid is also in a conductive state, when the flow velocity field is perpendicular to the temperature gradient, e.g., in a Couette flow induced by the motion of electrodes along their surfaces.

Table 1.2: Three elementary electrode configurations and the fields in the stationary conductive state $\bar{\mathbf{u}} = 0$. A temperature difference $\Delta T = T_1 - T_2$ and an electric tension $V(t) = \sqrt{2}\Phi_0 \sin(2\pi ft)$ are applied to the electrodes. Dimensionless parameters are used for brief expression: the thermoelectric parameter $\gamma_e = e\Delta T$ and the radius ratio $\eta = R_1/R_2$.

| | |
|---|---|
| (a) Plain parallel geometry | |
|  | $\bar{\theta} = -\Delta T \frac{y}{d} \quad \text{with} \quad T_{\text{ref.}} = \frac{T_1 + T_2}{2}, \quad (1-12)$ |
| | $\bar{\mathbf{E}} = -\frac{\Phi_0}{d} \frac{\gamma_e}{\log\left(\frac{1-\gamma_e/2}{1+\gamma_e/2}\right)} \frac{1}{1 + \gamma_e y/d} \mathbf{e}_y, \quad (1-13)$ |
| | $\bar{\mathbf{g}}_e = -\frac{e\epsilon_{\text{ref.}}\Phi_0^2\gamma_e}{\alpha\rho d^3} \left[\frac{\gamma_e}{\log\left(\frac{1-\gamma_e/2}{1+\gamma_e/2}\right)} \right]^2 \left(1 + \gamma_e \frac{y}{d}\right)^{-3} \mathbf{e}_y \quad (1-14)$ |
| (b) Cylindrical annular geometry | |
|  | $\bar{\theta} = \Delta T \frac{\log(r/R_2)}{\log \eta} \quad \text{with} \quad T_{\text{ref.}} = T_2, \quad (1-15)$ |
| | $\bar{\mathbf{E}} = \frac{\Phi_0}{r \log \eta} \frac{\gamma_e}{\log(1 - \gamma_e)} \left[1 - \gamma_e \frac{\log(r/R_2)}{\log \eta} \right]^{-1} \mathbf{e}_r, \quad (1-16)$ |
| | $\bar{\mathbf{g}}_e = -\frac{e\epsilon_2}{\alpha\rho} \left(\frac{\Phi_0}{\log \eta} \right)^2 \left[\frac{\gamma_e}{\log(1 - \gamma_e)} \right]^2 \frac{1 - \frac{\gamma_e}{\log \eta} \left(1 + \log \frac{r}{R_2}\right)}{r^3 \left[1 - \gamma_e \frac{\log(r/R_2)}{\log \eta} \right]^3} \mathbf{e}_r. \quad (1-17)$ |
| (c) Spherical shell geometry | |
|  | $\bar{\theta} = \frac{\eta}{1 - \eta} \Delta T \left(\frac{R_2}{r} - 1 \right) \quad \text{with} \quad T_{\text{ref.}} = T_2, \quad (1-18)$ |
| | $\bar{\mathbf{E}} = -\frac{\eta\Phi_0}{(1 - \eta)R_2 \log(1 - \gamma_e)} \left(\frac{R_2}{r} \right)^2 \left[1 - \frac{\eta\gamma_e}{1 - \eta} \left(\frac{R_2}{r} - 1 \right) \right]^{-1} \mathbf{e}_r, \quad (1-19)$ |
| | $\bar{\mathbf{g}}_e = -\frac{2e\epsilon_2\Phi_0^2}{\alpha\rho R_2^3} \left(\frac{\eta}{1 - \eta} \right)^2 \left[\frac{\gamma_e}{\log(1 - \gamma_e)} \right]^2 \left(\frac{R_2}{r} \right)^5 \frac{1 - \frac{\eta\gamma_e}{2(1 - \eta)} \left(\frac{R_2}{r} - 2 \right)}{\left[1 - \frac{\eta\gamma_e}{1 - \eta} \left(\frac{R_2}{r} - 1 \right) \right]^3} \mathbf{e}_r. \quad (1-20)$ |

$\phi = \phi(\zeta)$, so that the electric field is in the ζ direction. The heat conduction equation (1-9c) and the Gauss' law (1-10a) are then imply that the heat and electric fluxes are constant:

$$S \frac{d\theta}{d\zeta} = cst., \quad \epsilon S \frac{d\phi}{d\zeta} = cst., \quad (1-21)$$

where S is the geometrical factor: $S = 1, r,$ and r^2 for the plane, cylindrical, and spherical cases. The temperature

field can be obtained by integrating the first equation with taking into account the boundary conditions (1-11). Eliminating ζ from these two equations and, then, eliminating θ from the result with making use of the linear relationship (1-3), we have $\epsilon d\phi/d\epsilon = cst.$, of which the solution under the boundary conditions (1-11) is given by

$$\phi = \Phi_0 \frac{\log [\epsilon(\theta)/\epsilon_2]}{\log (\epsilon_1/\epsilon_2)}. \quad (1-22)$$

The values of the permittivity at the electrodes S_1 and S_2 are denoted by ϵ_1 and ϵ_2 , respectively: $\epsilon_1 = \epsilon(\theta_1)$, $\epsilon_2 = \epsilon(\theta_2)$. Substituting this result in Eq. (1-7c), we get:

$$\mathbf{g}_e = -\frac{e\epsilon_2}{\rho\alpha\epsilon^2} \left[\frac{\Phi_0}{\log (\epsilon_1/\epsilon_2)} \right]^2 \left(\frac{d\epsilon}{d\zeta} \right)^2 \left(\frac{1}{\epsilon} \frac{d\epsilon}{d\zeta} + \frac{1}{S} \frac{dS}{d\zeta} \right) \mathbf{e}_\zeta. \quad (1-23)$$

The electric gravity is aligned with the ζ axis. The temperature, the electric field and the electric gravity calculated with Eqs. (1-22), & (1-23) for different electrode configurations are summarized in Table 1.2.

The two terms inside the last parenthesis in Eq. (1-23) represent the competition between the permittivity stratification and the geometry curvature. In the plane geometry, the latter effect is absent and the direction of the electric gravity is opposite to the permittivity gradient. Since the permittivity decreases with the temperature, \mathbf{g}_e is in the same direction as the temperature gradient. This result also holds in curved geometries when the curvature is small: the gravity is centripetal if the inner electrode is hotter than the outer one (outward heating); it is centrifugal otherwise. If the curvature effect dominates over the stratification, the electric gravity is centripetal independently of heating direction. When the permittivity stratification and the curvature are comparable, the electric gravity can change its direction inside the gap. The phase diagram in Fig. 1-1 summarizes the direction of the electric gravity in curved geometries, where γ_e is the *thermoelectric parameter* $\gamma_e = e\Delta T$ and η is the radius ratio $\eta = R_1/R_2 (< 1)$ of the inner to outer cylinder radii. The thermoelectric parameter γ_e quantifies the permittivity stratification. The radius ratio η characterizes the geometry curvature. A small η means a large curvature.

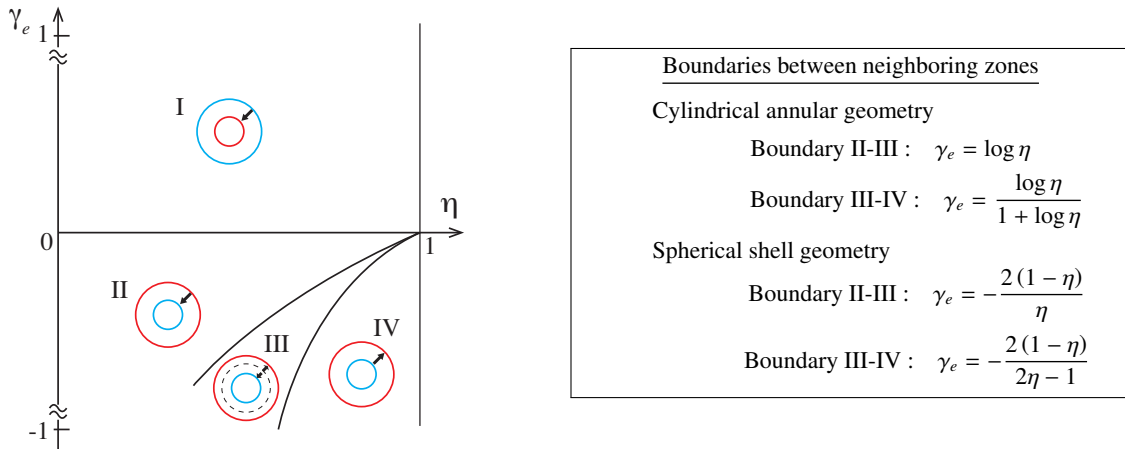


Figure 1-1: Phase diagram of the electric gravity configuration in cylindrical and spherical geometries. The thermoelectric parameter $\gamma_e = e\Delta T$ is positive (negative), when the heating is outward (inward). The parameter η is the ratio of the inner to outer cylinder radii: $\eta = R_1/R_2$.

1.5 Control parameters and nondimensionalized governing equations

In the light of the analogy of the thermal DEP force with the thermal Archimedean buoyancy force, we can find dimensionless parameters characterizing the TEHD convection. In the ordinary thermal convection, the Rayleigh number $R = \alpha \Delta T g d^3 / \nu \kappa$ controls the stability of the conductive state. The nonlinear development of the convection depends on the Rayleigh number as well as the Prandtl number $\text{Pr} = \nu / \kappa$ that compares momentum to thermal diffusions. For the TEHD convection, Roberts introduced a dimensionless number L that plays an equivalent role to the Rayleigh number [65]:

$$L = \frac{\alpha \Delta T G_{e,0} d^3}{\nu \kappa}, \quad (1-24)$$

where $G_{e,0}$ is the electric gravity estimated at some reference point in the fluid. The TEHD convection will also depend on the Prandtl number.

For the TEHD convection, we need also the thermoelectric parameter $\gamma_e = e \Delta T$. It appears, indeed, in the formulae of the electric gravity in the conductive state (Table 1.2).

These three dimensionless numbers emerge naturally when we nondimensionalize the governing equations (1-9) and (1-10) with the scales d of length, τ_v of time, d/τ_v of velocity, ΔT of temperature, Φ_0 of electrostatic potential and $G_{e,0}$ of electric gravity:

$$\nabla \cdot \mathbf{u} = 0, \quad (1-25a)$$

$$\frac{\partial \mathbf{u}}{\partial t} + \mathbf{u} \cdot \nabla \mathbf{u} = -\nabla \pi + \nabla^2 \mathbf{u} - \frac{L}{\text{Pr}} \theta \mathbf{g}_e, \quad (1-25b)$$

$$\frac{\partial \theta}{\partial t} + \mathbf{u} \cdot \nabla \theta = \frac{1}{\text{Pr}} \nabla^2 \theta, \quad (1-25c)$$

$$\nabla \cdot [(1 - \gamma_e \theta) \nabla \phi] = 0. \quad (1-25d)$$

The last equation is the Gauss' law (1-10a), nondimensionalized and expressed in terms of the electrostatic potential ϕ . The electric gravity \mathbf{g}_e in Eq. (1-25b) is related to the electric field by

$$\mathbf{g}_e = \mathcal{G} \nabla \frac{(\nabla \phi)^2}{2}. \quad (1-26)$$

The factor $\mathcal{G} = e \epsilon_{\text{ref}} \Phi_0^2 / \rho \alpha d^3 G_{e,0}$ is not independent of other dimensionless numbers. It is a function of γ_e in the plane geometry and of (η, γ_e) in the curved geometries.

The boundary conditions (1-11) is nondimensionalized as follows:

$$\mathbf{u} = \mathbf{0}, \quad \theta = \theta_1, \quad \phi = 1 \quad \text{at } S_1, \quad (1-27a)$$

$$\mathbf{u} = \mathbf{0}, \quad \theta = \theta_2, \quad \phi = 0 \quad \text{at } S_2, \quad (1-27b)$$

where the nondimensionalized temperature deviations θ_1 and θ_2 should satisfy $\theta_2 - \theta_1 = 1$. The set of equations (1-25) and (1-26) with the boundary conditions (1-27) provides the theoretical basis for the analysis of the TEHD convection.

Chapter 2

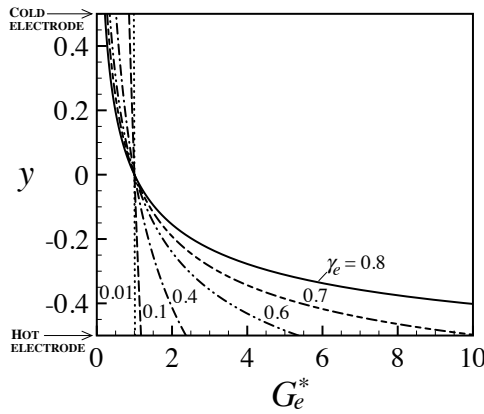
TEHD convection in plane geometry

Theoretical and numerical investigations on the TEHD convection in plane parallel geometry are reported in this chapter. These investigations were performed in 2012 at the Laboratoire Ondes et Milieux Complexes in Le Havre in collaboration with Mireille Tadie Fogaing, Olivier Crumeyrolle and Innocent Mutabazi. Obtained results were communicated at a number of conferences and seminars. They were published in *Eur. Phys. J. E* [27] and in *Phys. Rev. E* [97]. These articles are included in appendix C.

2.1 Introduction

The temperature and electric fields, $(\bar{\mathbf{u}}, \bar{\mathbf{E}})$, in the conductive state are given in Table 1.2 (Eqs. 1-12 & 1-13). The temperature is a linear function of the coordinate normal to the wall surfaces (y) as in the Rayleigh-Bénard (RB) problem. The electric field is intense in the hot fluid zone near the hot electrode, where the permittivity is small. The electric gravity given by Eq. (1-14) is directed from cold to hot electrodes so that the thermoelectric buoyancy is expected to have destabilizing effects on the conductive state.

Figure 2-1 shows some profiles of the electric gravity normalized by its value at the mid-gap. For small thermoelectric parameters, $\gamma_e < 0.1$, the gravity \mathbf{g}_e is almost uniform throughout the fluid layer. In contrast, the non-uniformity is significant for $\gamma_e > 0.1$: the gravity takes large values in the vicinity of the hot electrode and attenuates near the cold electrode. This non-uniformity at large γ_e will differentiate the TEHD convection from the classical RB convection, in which the Earth's gravity \mathbf{g} is uniform.



Electric gravity at the mid-gap

| ΔT [K] | γ_e [-] | $G_e(0)$ [m/s ²] |
|---------------------|---------------------|----------------------------------|
| 0.06 | 0.01 | 0.46 |
| 0.65 | 0.1 | 4.60 |
| 2.58 | 0.4 | 17.9 |
| 3.87 | 0.6 | 26.0 |
| 4.52 | 0.7 | 29.6 |
| 5.16 | 0.8 | 32.9 |

Figure 2-1: Electric gravity $\bar{\mathbf{g}}_e = -G_e(y)\mathbf{e}_y$ in the conductive state in plane geometry for different values of the thermoelectric parameter γ_e . (a) Normalized profiles $G_e^*(y) = G_e(y)/G_e(0)$. (b) Values $G_e(0)$ in acetonitrile for an electrode configuration with a gap $d = 10$ mm and an electric tension $\Phi_0 = 1$ kV.

The instability generating the TEHD convection has been investigated theoretically in plane geometry since the pioneering work of Roberts [65] and Turnbull [87] at the late 60's. They investigated the stability of the conductive state, with or without the Earth's gravity. In microgravity conditions, Roberts predicted the critical electric Rayleigh number $L_c = 2128.696$, beyond which a stationary critical mode of wavenumber $k_c = 3.2260$ started to grow. This result was confirmed by later theories of Takashima & Hamabata [82] and Stiles [77]. Stiles et al. [79] performed a weakly nonlinear analysis and computed the heat transfer coefficient in the framework of the Landau theory. Their results show that the Nusselt number Nu , which is the ratio of the convective to conductive heat transfer, is given by $Nu = 1 + a\delta$ with $a \approx 0.8$, where δ is the normalized distance from the criticality: $\delta = L/L_c - 1$. The coefficient a characterizes the heat transfer improvement beyond but in the vicinity of the critical condition.

Even though all these theoretical works were performed for vanishing thermoelectric parameter: $\gamma_e \rightarrow 0$ and, hence, for a uniform electric gravity field, the instability threshold L_c is 20 % above the critical Rayleigh number R_c of the RB convection ($R_c = 1707.762$). The critical wavenumber k_c is slightly larger than that of the RB instability $k_c^{RB} = 3.117$ [12]. The heat transfer improvement coefficient a of the RB convection is given by $a^{RB} = 1.43$ [71]. The conductive state is, therefore, more stable against the electric gravity than against the Earth's gravity and the TEHD convection is less efficient in transferring heat than the RB convection.

The origins of these quantitative differences between the TEHD and RB convections have not been clarified by the existing studies. Our investigations are intended to reveal how these differences arise. A linear stability analysis (Sec. 2.2) and a direct numerical simulation (Sec. 2.3) are performed for this aim. The effects of the Prandtl number on the heat transfer (Sec. 2.4) are also examined, since the dependence of the flow behavior on the fluid properties is of practical interest in application.

2.2 Linear stability analysis

Flow states slightly deviated from the conductive state (1-12)–(1-14) are governed by Eqs. (1-25) linearized around the conductive state:

$$\nabla \cdot \mathbf{u}' = 0, \quad (2-1a)$$

$$\frac{\partial \mathbf{u}'}{\partial t} = -\nabla \pi' + \nabla^2 \mathbf{u}' - \frac{L}{\text{Pr}} \theta' \bar{\mathbf{g}}_e - \frac{L}{\text{Pr}} \bar{\theta} \mathbf{g}'_e, \quad (2-1b)$$

$$\frac{\partial \theta'}{\partial t} + \mathbf{u}' \cdot \nabla \bar{\theta} = \frac{1}{\text{Pr}} \nabla^2 \theta', \quad (2-1c)$$

$$\nabla \cdot \left[(1 - \gamma_e \bar{\theta}) \nabla \phi' + \gamma_e \theta' \bar{\mathbf{E}} \right] = 0, \quad (2-1d)$$

where \mathbf{u}' , θ' , and ϕ' are the perturbation components of the velocity, temperature, and electrostatic potential, respectively. The perturbation component of the electric gravity, \mathbf{g}'_e , is computed from the perturbation electric field by

$$\mathbf{g}'_e = \mathcal{G} \nabla (\bar{\mathbf{E}} \cdot \mathbf{E}') = -\mathcal{G} \nabla \left[\bar{\mathbf{E}} \cdot \nabla \phi' \right]. \quad (2-2)$$

The boundary conditions (1-27) read for the perturbation fields:

$$\mathbf{u}' = \theta' = \phi' = 0 \quad \text{at } y = \pm \frac{1}{2}. \quad (2-3)$$

Equation (2-1b) is identical to the linearized momentum equation governing the RB instability except the last term involving the perturbation electric gravity \mathbf{g}'_e . This component is a consequence of a feedback process of the

electric field to the temperature field: since the temperature perturbation θ' modifies the electric field through the Gauss' law (2-1d), the electric gravity also has a perturbation component. In addition to the non-uniformity of the gravity field $\bar{\mathbf{g}}_e$ (Fig. 2-1), this thermoelectric feedback would differentiate the TEHD convection from the RB convection.

Assuming an infinite lateral extent of the flow system, we can examine the stability of the conductive state by considering Eqs. (2-1) for a normal mode of $\exp[st + ikx]$, where $s = \sigma - i\omega$ is the complex growth rate (σ : the growth rate; ω : the frequency) and k is the wavenumber in the x direction. For this normal mode, Eqs. (2-1) read the set of ordinary differential equations with respect to the transversal coordinate y :

$$\mathbf{A}\mathbf{X} = s\mathbf{B}\mathbf{X}, \quad (2-4)$$

where $\mathbf{X} = [\hat{\mathbf{u}}' \hat{\pi}' \hat{\theta}' \hat{\phi}']^T$ is the complex amplitude of the normal mode and \mathbf{B} is a constant matrix. The differential matrix operator \mathbf{A} depends on the wavenumber k and involves the parameters (Pr, L, γ_e). We solve this eigenvalue problem numerically by invoking a spectral collocation method based on the Chebyshev polynomials. If the growth rate σ is negative for any wavenumber k , the conductive state is judged to be stable for a given set of parameters (L, Pr, γ_e). Otherwise, the conductive state is unstable.

Critical parameters

A marginal stability curve $L = L(k)$ is obtained for a given parameter set (Pr, γ_e) by determining the value of L at which the eigenvalue s crosses the imaginary axis in the complex plain. The minimum of a marginal curve gives the critical conditions for instability. Some marginal curves for different values of the thermoelectric parameter γ_e are shown in Fig. 2-2(a). Marginal curves are independent of the Prandtl number Pr . This observation is consistent with the fact that no oscillatory mode is found in the analysis. In fact, we can show from Eqs. (2-1) that the marginal conditions cannot depend on the Pr if the instability is stationary.¹ Marginal conditions, in contrast, depend on the thermoelectric parameter γ_e . While only slight influence is detected at small γ_e ($\lesssim 0.1$), the marginal curve shifts downward with increasing γ_e ($\gtrsim 0.1$).

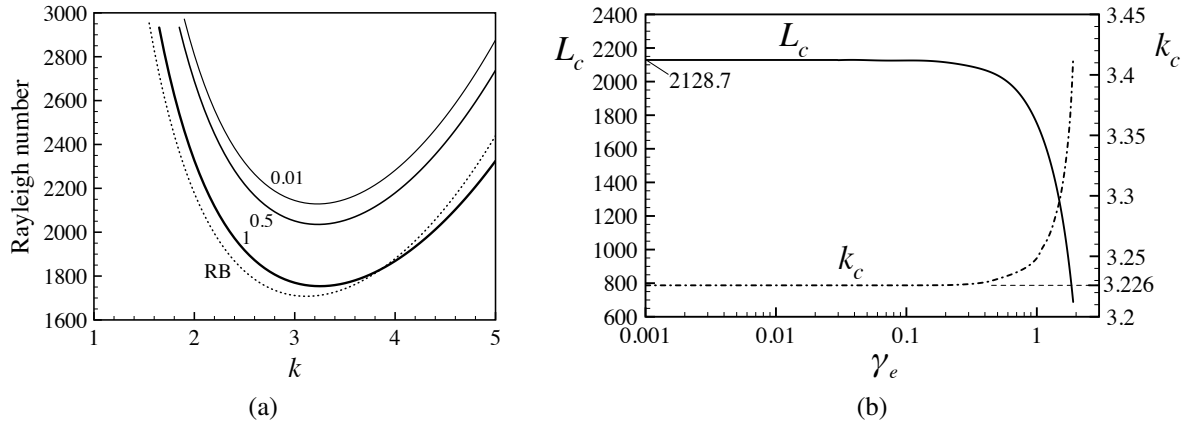


Figure 2-2: Predictions of the linear stability theory: (a) Marginal curves for different values of the thermoelectric parameter $\gamma_e = e\Delta T$, (b) Critical electric Rayleigh number L_c and wavenumber k_c . In (a), the marginal curve of the Rayleigh-Bénard instability is also shown for reference.

¹Once the time, velocity, and pressure are rescaled by Pr^{-1} , Pr , and Pr , respectively, i.e., when we substitute $\text{Pr}t$, $\text{Pr}^{-1}\mathbf{u}$, and $\text{Pr}^{-1}\pi$ to t , \mathbf{u} , and π in the governing Eqs. (2-1), the Prandtl number appears only as coefficients of the time derivative terms. The Prandtl number can hence not influence any stationary mode in marginal conditions.

As this behavior of the marginal curve implies, the critical electric Rayleigh number and wave number are constant for γ_e smaller than 0.1 (Fig. 2-2b). They are $L_c = 2128.7$ and $k_c = 3.226$, recovering the results reported in early investigations [65, 77, 82]. Significant variation is found both in L_c and k_c for $\gamma_e > 0.1$. This variation would arise from the non-uniformity of the electric gravity $\bar{\mathbf{g}}_e$: according to its profiles in Fig. 2-1, a sublayer with intense gravity appears in the vicinity of the hot electrode beyond $\gamma_e = 0.1$. The instability would occur within this sublayer rather than in the whole gap. Eigenfunctions of the critical modes confirm this conjecture (Fig. 2-3). The convection is concentrated in a sublayer attached on the hot electrode. The reference electric gravity $G_{e,0}$ taken at the mid-gap will underestimate the electric gravity in this sublayer. This explain the decrease of the critical electric Rayleigh number for large $\gamma_e (> 0.1)$. The sublayer also gives an explanation to the increase of the critical wavenumber at large γ_e , as its thickness is smaller than the whole layer thickness.

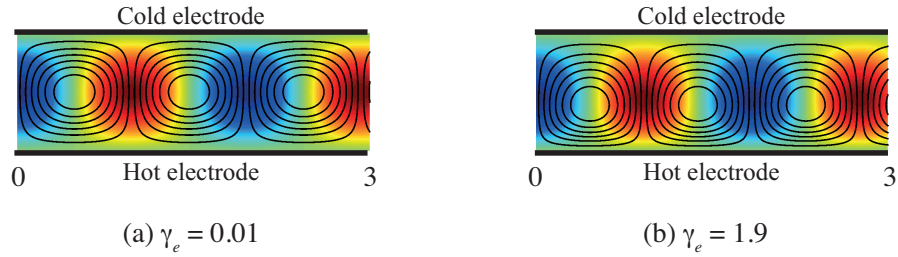


Figure 2-3: Eigenfunctions of critical modes for different values of the thermoelectric parameter γ_e . Velocity and temperature fields are shown by streamlines and by colors, respectively.

Energy transfer from base to perturbation flows

The critical parameters (L_c, k_c) take values different from the RB instability in spite of the gravito-EHD analogy. This difference is significant even at vanishing γ_e , where the electric gravity is uniform (Fig. 2-1). Its origin should be attributed to the perturbation electric gravity, \mathbf{g}'_e . In order to quantify the effects of this perturbation component, we can use an evolution equation for the kinetic energy of perturbation flow. This equation is derived from the linearized momentum Eq. (2-1b) by taking inner products with \mathbf{u}' . By averaging the result over a spatial period in the x direction and by integration over the gap, we have

$$\frac{dK}{dt} = W_{BG} + W_{PG} - D_v, \quad (2-5)$$

where K is the kinetic energy of the perturbation flow, W_{BG} and W_{PG} are the power by the buoyancy forces associated with the base and perturbation electric gravities, and D_v is the viscous energy dissipation rate. These terms are computed from the volumetric density of corresponding quantities:

$$K = \langle \mathcal{K} \rangle, \quad W_{BG} = \langle w_{BG} \rangle, \quad W_{PG} = \langle w_{PG} \rangle, \quad D_v = \langle d_v \rangle, \quad (2-6a)$$

$$\text{with the densities } \mathcal{K} = \frac{1}{2} \mathbf{u}'^2, \quad w_{BG} = -\frac{L}{\text{Pr}} \theta' \bar{\mathbf{g}}_e \cdot \mathbf{u}', \quad w_{PG} = -\frac{L}{\text{Pr}} \theta' \bar{\mathbf{g}}'_e \cdot \mathbf{u}', \quad d_v = \dot{\epsilon} : \dot{\epsilon}, \quad (2-6b)$$

where $\dot{\epsilon}$ is the rate-of-strain tensor. The angle brackets mean the averaging and integrating operation:

$$\langle \cdot \rangle = \frac{k}{2\pi} \int_0^{2\pi/k} dx \int_{-1/2}^{1/2} dy \cdot \cdot \quad (2-7)$$

Equation (2-5) is the Reynolds-Orr equation truncated at the first order. It states that the growth of the perturbation flow occurs, if the sum of the energies transferred from the base state through the powers W_{BG} and W_{PG} is larger than the viscous energy dissipation D_v .

Figure 2-4 shows the powers and the viscous dissipation rate in Eq. (2-5) normalized by $2K$. They are computed at critical conditions so that the sum of them is null. It is seen that W_{BG} , W_{PG} , and D_v are all constant at small γ_e until $\gamma_e \approx 1$. As expected from the gravito-EHD analogy, the buoyancy due to the base electric gravity $\bar{\mathbf{g}}_e$ is responsible for the instability. In contrast, the buoyancy due to the perturbation electric gravity \mathbf{g}'_e is stabilizing ($W_{PG} < 0$). Its magnitude is about 0.2 times W_{BG} . This implies that the buoyancy due to $\bar{\mathbf{g}}_e$ must overcome not only the viscous energy dissipation but also the stabilizing contribution of \mathbf{g}'_e . This explains why the critical value of L of the TEHD instability is larger than the critical Rayleigh number of the RB instability by 20 %.

At γ_e larger than 1, the power W_{BG} increases to compensate the increase in the viscous dissipation D_v . The behavior of D_v would be associated with the non-uniformity of the base gravity $\bar{\mathbf{g}}_e$. The concentration of the flow in the sublayer attached on the hot electrode (Fig. 2-3b) gives rise to a smaller flow structure, leading to intense viscous energy dissipation.

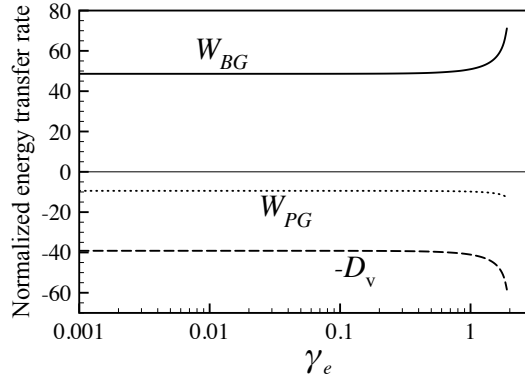


Figure 2-4: Different terms in the kinetic energy equation (2-5): W_{BG} : the power by the buoyancy due to the base electric gravity; W_{PG} : the power by the buoyancy due to the perturbation electric gravity; D_v : the viscous energy dissipation rate. All the terms are computed for critical modes and normalized by the twice of the kinetic energy K .

Dispersion relation

The growth rate σ of the TEHD instability exhibits a typical dispersion relation of a type-I instability, i.e., the instability with a critical mode of finite wavenumber (Fig. 2-5). The maximum of the dispersion curve varies with (L, γ_e) and the detailed shape of the curve depends on the Prandtl number. From the variation of σ in function of k and $\delta (= L/L_c - 1)$, we can determine a time scale τ_0 and a length scale ξ_0 , both characterizing the behavior of the system in the vicinity of the criticality [18]:

$$\tau_0 = \left(\frac{\partial \sigma}{\partial \delta} \right)_{cr}, \quad \xi_0 = \sqrt{\frac{\tau_0}{2} \left(\frac{\partial^2 \sigma}{\partial k^2} \right)_{cr}}. \quad (2-8)$$

The time scale τ_0 gives the perturbation growth rate by δ/τ_0 and the length ξ_0 specifies a spatial scale of amplitude modulation in the weakly nonlinear state of the system. They appear in the Ginzburg-Landau equation as coefficients (Sec. 2.3).

Similar to the RB convection, the scale τ_0 increase with the Prandtl number Pr and the scale ξ_0 is independent

of Pr. As shown in Fig. 2-6(a), the variation of τ_0 agrees well with the result obtained for the RB instability: $\tau_0^{RB} = (\text{Pr} + 0.5117)/19.65$ [19]. Both scales are independent of γ_e at small γ_e ($\lesssim 0.5$), while they decrease slightly with γ_e , about 5 % over the range $0.5 \leq \gamma_e \leq 1.5$ (Fig. 2-6b for ξ_0).

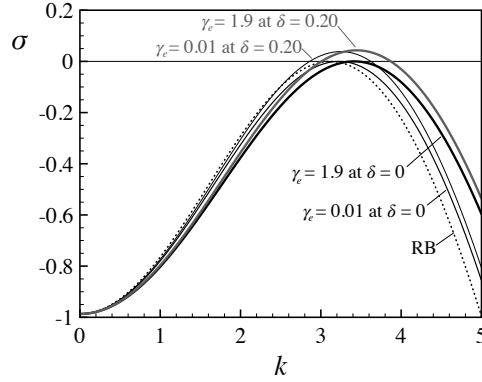


Figure 2-5: Dispersion curves $\sigma = \sigma(k)$ at different distances $\delta (= L/L_c - 1)$ from the criticality and for different values of the thermoelectric parameter γ_e .

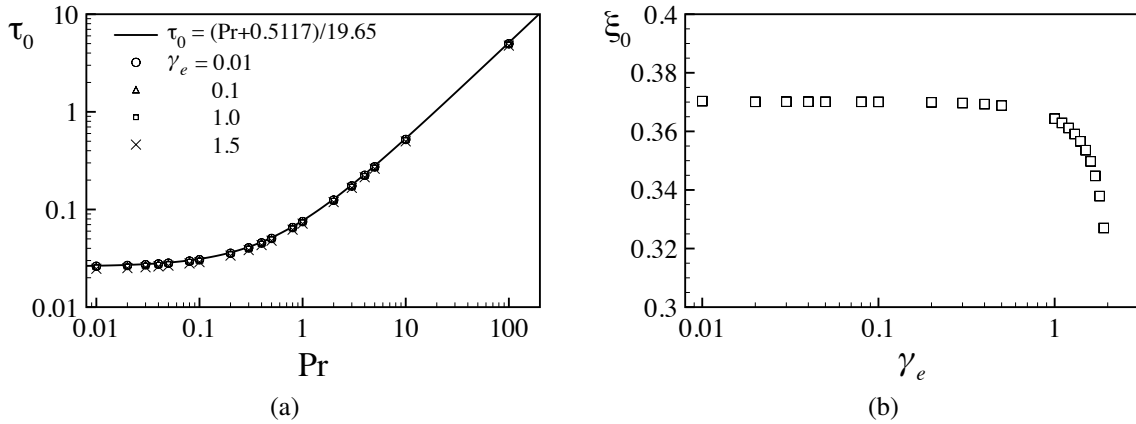


Figure 2-6: Time scale τ_0 and length scale ξ_0 computed from the dispersion relation $\sigma = \sigma(k)$.

2.3 2D numerical simulation

We investigate the nonlinear behavior of the convection developing from the TEHD instability by a direct numerical simulation. In the simulation, the flow is assumed two-dimensional and confined in a finite lateral extent Γd . The aspect ratio Γ is fixed at a large value: $\Gamma = 117$ (Fig. 2-7). The lateral walls are rigid and suppress perturbations by the following imposed boundary conditions:

$$\mathbf{u} = 0, \quad \frac{\partial \theta}{\partial x} = 0, \quad \frac{\partial \phi}{\partial x} = 0 \quad \text{at} \quad x = \pm \frac{\Gamma}{2}, \quad (2-9)$$

i.e., no heat flux and no electric flux across the lateral wall surfaces. These conditions are compatible with the conductive state (1-12)–(1-14) that was regarded as the base state in the linear stability theory in Sec. 2.2. The condition of no electric flux is valid for a wall material of small permittivity ϵ_{wall} compared with ϵ .² If the wall

²The Gauss' law requires $\epsilon(E_{\perp})_{fluid} = \epsilon_{wall}(E_{\perp})_{wall}$ for non charged wall surface [33], where E_{\perp} stands for the normal component of electric field to the surface. Thus, the condition of no electric flux means $\partial \phi / \partial x = (E_{\perp})_{fluid} = (\epsilon_{wall} / \epsilon)(E_{\perp})_{wall} = 0$.

material does not satisfy this requirement, we should modify no electric flux condition. The lateral walls wouldn't however produce any significant effects at the convection in the central part ($x \approx 0$) for such a large aspect ratio as the considered geometry.

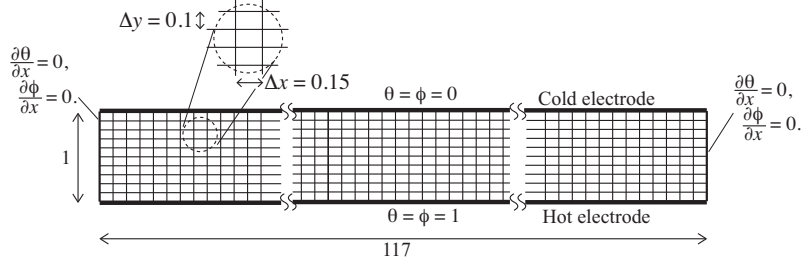


Figure 2-7: Grids and boundary conditions employed in the DNS.

The numerical code is based on the finite element method and implemented on a commercial CFD software (COMSOL Multiphysics 3.5). A regular grid system has been employed with sides $\Delta x = 0.15$ and $\Delta y = 0.1$ (Fig. 2-7). The initial velocity, temperature and electric fields are specified as null everywhere and a temperature difference ΔT ($= 1$) and electric tension Φ_0 ($= 1$) are applied instantaneously at $t = 0$. Simulations are performed for different Prandtl numbers, while the thermoelectric parameter is kept at a small value ($\gamma_e = 0.03$).

No convection is observed at small electric Rayleigh number L and the heat transfer is only due to thermal conduction in the fluid. For L larger than 2130, stationary convection rolls develop through a supercritical bifurcation and improve the heat transfer. The rolls have a well-defined spatial period in the x direction with a wavenumber about 3.2 (Fig. 2-8a). Observed wavenumber values are shown in Fig. 2-8(b), where the Eckhaus instability boundary $\delta = 3\xi_0^2(k - k_c)^2$ is also shown. The value of ξ_0 determined in Sec. 2.2 is used for tracing this boundary. All the wavenumbers are found inside the curve so that the observed convection flows are stable against the Eckhaus instability.

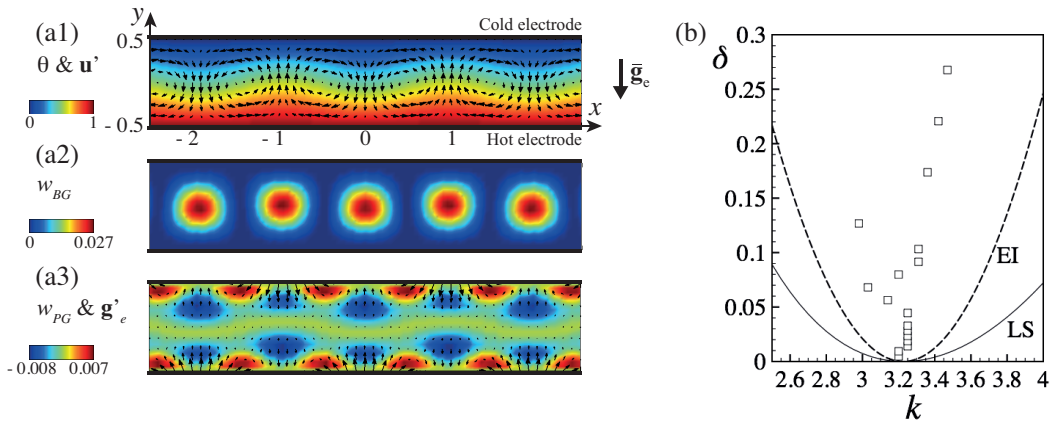


Figure 2-8: Saturated TEHD convection. (a) Fields at $L = 2200$: (a1) the temperature and velocity; (a2) the power density w_{BG} by the buoyancy due to the base electric gravity; (a3) the power density w_{PG} by the buoyancy due to the perturbation electric gravity as well as the perturbation gravity itself. (b) Wavenumbers at different distances δ ($= L/L_c - 1$) from the criticality. The curve labeled as LS is the marginal stability curve determined by the linear stability theory. The curve EI is the Eckhaus instability boundary.

The energy transfer from the base to perturbation flows can be analyzed by the same kinetic energy equation as Eq. (2-5), but with W_{PG} completed by a higher order contribution of the perturbation electric gravity:

$$W_{PG} = \langle w_{PG} \rangle, \quad \text{with the density } w_{PG} = -\frac{L}{\text{Pr}} (\bar{\theta} \mathbf{g}'_e \cdot \mathbf{u}' + \theta' \mathbf{g}'_e \cdot \mathbf{u}'). \quad (2-10)$$

The buoyancy due to the base electric gravity $\bar{\mathbf{g}}_e$ transfers energy at the mi-gap (Fig. 2-8a2), while the power by the buoyancy due to the perturbation electric gravity \mathbf{g}'_e is efficient rather in the vicinity of the electrodes (Fig. 2-8a2). The viscous energy dissipation occurs on the electrodes, as in the RB convection.

Figure 2-9 shows different energy transfer terms of the kinetic energy Eq. (2-5) computed for saturated flow states. Each term is proportional to the normalized distance from the criticality δ . The base and perturbation electric gravities have destabilizing and stabilizing effects, respectively, similar to the results obtained by the linear theory (Sec. 2.2). Their ratio of $W_{BG}/|W_{PG}|$ is also around 0.2. The perturbation electric gravity persists to impede the convection flow so much as in the linear flow regime.

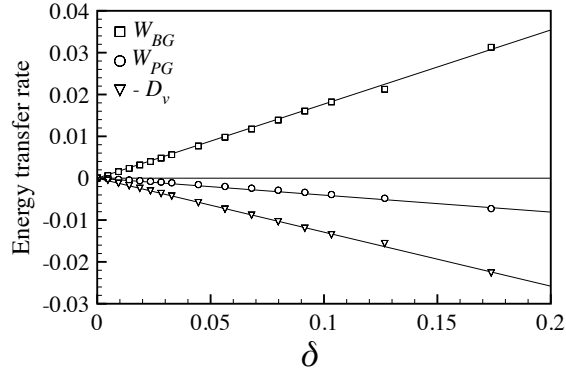


Figure 2-9: Energy transfer terms in the kinetic energy equation (2-5) for saturated convection ($\text{Pr} = 100$, $\gamma_e = 0.03$). The horizontal axis is the distance $\delta (= L - L_c - 1)$ from the criticality.

Weakly nonlinear model

The TEHD instability is of type I-s [20, 18]. The behavior of the flow in the weakly nonlinear regime can be described by the Ginzburg-Landau equation with real coefficients:

$$\tau_0 \frac{\partial A}{\partial t} = \delta A + \xi_0^2 \frac{\partial^2 A}{\partial x^2} - \ell |A|^2 A, \quad (2-11)$$

where A is the amplitude of perturbation flow. We have already obtained the values of ξ_0 and τ_0 from the dispersion relation in Sec. (2.2). We can confirm these values by determining them from the DNS results.

From the initial stage of the convection development in DNS where the amplitude increases exponentially, we can determine the growth rate σ . Repeating this determination at different distances δ , we obtain τ_0^{-1} as the coefficient of proportionality between σ and δ : $\sigma = \tau_0^{-1} \delta$. The value of ξ_0 can be determined from the saturated flow near one of the lateral walls. In a system with a large lateral extent as in the present case, the suppressing effect of a lateral wall results in a hyperbolic tangent variation of the amplitude: $|A| = \sqrt{\delta/\ell} \tanh[(x - x_w)/\xi]$, where $\xi = \sqrt{2}\xi_0\delta^{-1/2}$ and x_w is the coordinate of the wall. This envelope function predicts correctly the amplitude behavior (Fig. 2-10a2). The best fitting hyperbolic tangent profile gives a value of ξ . Determining ξ for different δ , we obtain ξ_0 as the coefficient of proportionality of the relationship $\xi^{-2} = \delta/2\xi_0^2$ (Fig. 2-10b). Determined values recover the results from the dispersion relation reported in Sec. 2.2.

The coefficient of the nonlinear term, ℓ , can be determined from the amplitude A_0 of saturated flow at the central zone. In a system with a large lateral extent, the amplitude is constant ($\partial_x A = 0$) in the central zone so that $A_0 = \sqrt{\delta/\ell}$ according to Eq. (2-11). Plotting A_0^2 in function of δ , the constant ℓ is determined from the coefficient of proportionality between them (Fig. 2-10b).

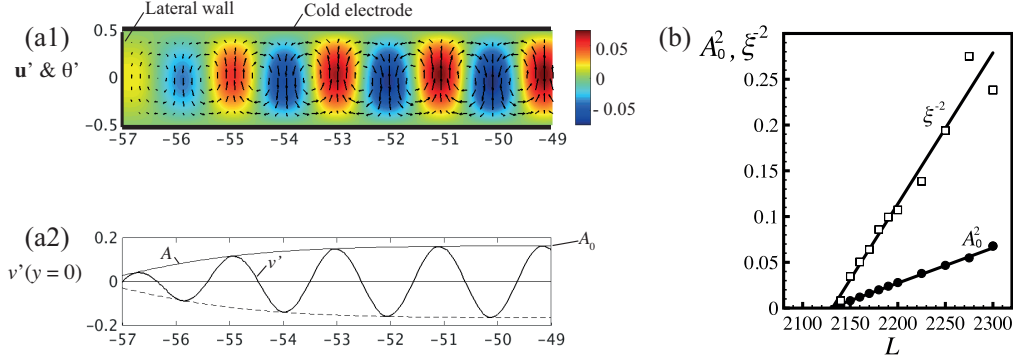


Figure 2-10: Suppressing effects of a lateral wall at $x = -57$ ($\text{Pr} = 10$, $L = 2200$, $\gamma_e = 0.03$). (a1) Velocity and perturbation temperature fields, (a2) Transversal velocity component v' at the mid-gap with a hyperbolic tangent envelop A ; (b) The saturated amplitude at the central zone, A_0 , and the constant ξ that characterizes the hyperbolic tangent envelop.

2.4 Heat transfer

As in the RB convection, the heat transfer is improved by TEHD convection (Fig. 2-11a). In the vicinity of the criticality, the enhancement is given by $Nu = 1 + a\delta$ with $a = 0.78$ for Pr larger than the unity. This value of the improvement coefficient recovers the result of Stiles et al. [79] obtained by a weakly nonlinear analysis. It is significantly smaller than the coefficient for the RB convection. In the simulations, γ_e is small so that the electric gravity $\bar{\mathbf{g}}_e$ is uniform. The observed difference in the value of a between the two convections should be attributed to the buoyancy associated with the perturbation electric gravity. Indeed, as we have seen earlier, W_{PG} takes non-negligible value even in saturated state of convection. The impeding effect of \mathbf{g}'_e on the flow leads to a smaller efficiency of the heat transfer enhancement in the TEHD convection than in the RB convection.

Figure 2-11 (b) shows the values of the coefficient a for different Prandtl numbers. For $\text{Pr} < 0.1$, a increases with Pr , while it is constant for $\text{Pr} \gtrsim 1$. In the RB convection, the variation of the coefficient is given by $a^{RB} = (0.69942 - 0.00472 \text{Pr}^{-1} + 0.00832 \text{Pr}^{-2})^{-1}$ [71]. Seeking for a similar equation, we obtain the correlation for the TEHD convection heat transfer:

$$a = \left(1.28 - \frac{0.0273}{\text{Pr}} + \frac{0.0077}{\text{Pr}^2} \right)^{-1}. \quad (2-12)$$

The curves $a = a(\text{Pr})$ and $a^{RB} = a^{RB}(\text{Pr})$ are shown in Fig. 2-11 (b). The difference between the two convections is significant at Pr larger than 0.1.

2.5 Conclusion

The analogy between TEHD convection and RB convection has been known since the beginning of its theoretical and experimental investigations. However, any critical examination of this analogy has not been done before our investigations. We confirmed similarities between these convection phenomena in the critical parameters and in

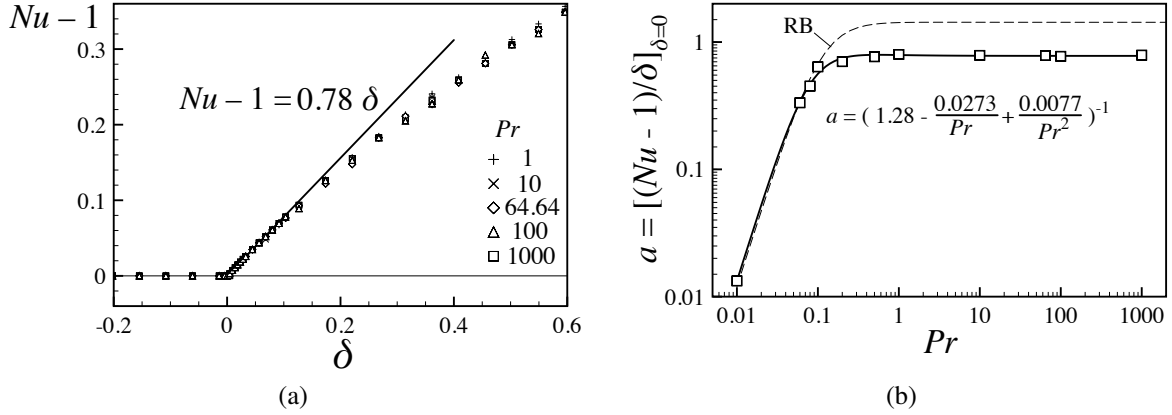


Figure 2-11: Heat transfer enhancement by TEHD convection: (a) the Nusselt number in function of the distance from the criticality δ ($L/L_c - 1$) for Prandtl numbers Pr larger than the unity; (b) the heat transfer improvement coefficient a .

their behavior in nonlinear flow regime. However, detailed analyses showed essential differences arising from two factors: the non-uniformity in the electric gravity field and the feedback of electric field to temperature field. The former effect is prominent only at large $\gamma_e \gtrsim 1$, while the latter always differentiates the TEHD convection from the RB one. The feedback gives rise to a perturbation component in the thermoelectric buoyancy force. For the convection to develop from the conductive state, the driving buoyancy force should overcome the stabilizing effect of this perturbation component as well as the viscous energy dissipation. Consequently, the critical parameters are different from those of the RB instability. The perturbation buoyancy component also impedes the flow in the nonlinear regime. The convection is weakened by it and the heat transfer is less efficient compared with the RB convection.

Chapter 3

TEHD convection in cylindrical annular geometry

Theoretical investigation on the TEHD convection in cylindrical annular geometry is reported. This research was done in 2012 at the Laboratoire Ondes et Milieux Complexes in Le Havre in collaboration with Satish Malik, Olivier Crumeyrolle and Innocent Mutabazi. The results were presented at a number of conferences and published in *Acta Astronaut.* [52] and in *Phys. Fluids* [96]. The latter article is included in appendix C.

3.1 Introduction

In the TEHD convection in plane geometry (Chap. 2), three dimensionless numbers are essential to characterize the system: the thermoelectric parameter γ_e , the Prandtl number Pr and the electric Rayleigh number L . An additional parameter is required in cylindrical annular geometry, which specifies the geometry curvature. We will adopt the ratio $\eta = R_1/R_2$ of the inner cylinder radius R_1 to the outer one R_2 as this parameter. Coupled with the direction of heating specified by the sign of γ_e , the fourth dimensionless number affects the system behavior significantly. Indeed, the electric gravity in the conductive state (Eq. 1-17) changes its direction in function of (η, γ_e) as illustrated in the electric gravity diagram in Fig. 1-1.

In outward heating, i.e., if the inner electrode is hotter than the outer one ($\gamma_e > 0$), the electric gravity (1-17) is centripetal for any η (*Zone I* in the electric gravity diagram). If the heating is inward ($\gamma_e < 0$), the direction of the electric gravity depends on η : centripetal when $\gamma_e > \log \eta$ (*Zone II*); centrifugal when $\gamma_e < \log \eta/(1 + \log \eta)$ (*Zone IV*). When γ_e is found in the narrow zone $\log \eta < \gamma_e < \log \eta/(1 + \log \eta)$ (*Zone III*), the gravity is centripetal in an inner layer and centrifugal in the outer layer. Fig. 3-1 (a) and (b) shows some profiles of the electric gravity. The gravity has been normalized by its magnitude at a reference position $r = r_{\text{ref}}$ inside the gap.

Early theoretical studies on the TEHD convection in cylindrical annular geometry focused to the stability of the conductive state against axisymmetric perturbations. Considered geometries were of small gap ($\eta \gtrsim 0.9$) and researchers had not been aware of the variety of the electric gravity behavior shown in the electric gravity diagram (Fig. 1-1). Chandra & Smylie[11], who pointed out the geophysical interest of the TEHD convection in curved geometries, performed a linear stability analysis with assuming vanishing thermoelectric parameter $\gamma_e \rightarrow 0$ and axisymmetric perturbations. Their analysis was restricted to the case where the electric gravity was centripetal with outward heating. The thermoelectric feedback effect, i.e., the perturbation electric gravity \mathbf{g}'_e , was neglected without any justification. For $\eta = 0.899$ that was a particular case corresponding to their experiment, they obtained the critical parameters $(L_c, k_c) = (2119.346, 3.117)$. In the experiment, they used a vertically installed cylindrical

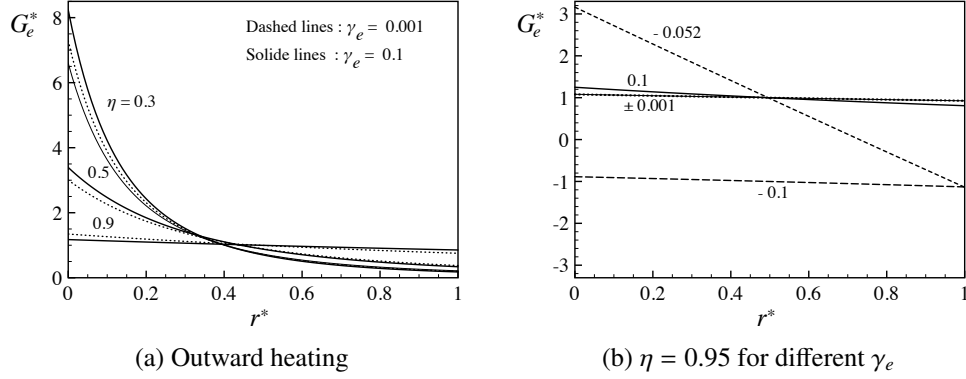


Figure 3-1: The electric gravity $\bar{\mathbf{g}}_e = -G_e(r)\mathbf{e}_r$ in the conductive state in cylindrical annular geometry: (a) profiles for different radius ratios η in outward heating ($\gamma_e > 0$) and (b) profiles in outward and inward heatings at $\eta = 0.95$. The centripetal acceleration is regarded as positive. The acceleration is normalized by its magnitude at a reference point $r = r_{\text{ref.}} = 1/|\log \eta|$: $G_e^* = G_e(r)/|G_e(r_{\text{ref.}})|$. The origin of the normalized shifted coordinate r^* coincides with the inner cylinder. The outer cylinder position corresponds to $r^* = 1$.

electric capacitor of large aspect ratio. The gap of the capacitor was small ($d = 1.92$ mm) and filled by a silicone oil of $\text{Pr} = 154$. The Grashof number $\text{Gr} = \alpha \Delta T g d^3 / \nu^2$ was kept at small values ($\text{Gr} \lesssim 3.5$) so that effects of the Earth's gravity were negligible. Their measurements showed continuous increase of the Nusselt number from the unity at a critical value of the electric Rayleigh number L , implying that the TEHD convection developed beyond the instability threshold through a supercritical bifurcation. The predicted value of L_c agreed well with the experiments. No flow visualization was realized and the wavenumber of the convection was not determined.

Takashima [81] performed a more systematic theoretical study with varying the imposed temperature difference and the radius ratio η , but with keeping the assumption of axisymmetric perturbations. He considered both inward and outward heating for narrow gap geometries: $0.9091 \leq \eta \leq 0.9999$. He took into account partially the thermoelectric feedback effect. His analysis showed strong sensitivity of the stability to the heating direction. With decreasing η , the critical electric Rayleigh number decreased in outward heating, while it increased and seemed to diverge in inward heating. The critical wavenumber varied little and was around 3.2 in outward heating. In inward heating, it increased rapidly with decreasing η .

Recently, Sitte et al. [73] have realized flow visualization by a schlieren technique in a microgravity environment during parabolic flights. Their cylindrical capacitors had large gap ($\eta = 0.29$ and 0.45). They obtained temperature fields integrated in the axial direction. The fields indicated that the developed convection was non axisymmetric.

All the existing theories were concerned only with small gap geometries ($\eta \gtrsim 0.9$). They were all based on the assumption of axisymmetric perturbations, even though an experiment indicated non-axisymmetric convective flows. In our investigation, we explore the whole range of η and to consider both axisymmetric and non-axisymmetric perturbations. The role of thermoelectric parameter is also examined, considering both outward and inward heating cases. The investigation is also intended to get insights into the instability mechanism in order to check the idea of the experimental simulations of geophysical flows: we try to clarify similarities with and differences from thermal convections in a radial gravity field.

Our theoretical work is based on the nondimensionalized governing equations (1-25). The electric Rayleigh number L in the momentum Eq. (1-25b) is based on the electric gravity $G_{e,0}$ at a reference point $r_{\text{ref.}}$ (Eq. 1-24). In the

present chapter, we adopt

$$r_{\text{ref.}} = \frac{1}{|\log \eta|}. \quad (3-1)$$

This coordinate is a radial position where the effect of the geometry curvature cancels in the sense that the heat flux density at $r = r_{\text{ref.}}$ takes the same value as in a plane geometry of the same gap size and the same imposed temperature difference. This reference point is found inner than the mid-gap $r = (r_1 + r_2)/2$, where r_1 and r_2 are the nondimensionalized radial positions of the inner and outer cylinders: $r_1 = \eta/(1 - \eta)$, $r_2 = 1/(1 - \eta)$.

3.2 Linear stability analysis

The evolution of small perturbations around the conductive state is governed by the linearized governing Eqs. (2-1) given in the previous chapter, but with the base conductive state (1-15)–(1-17). The perturbation electric gravity is computed by Eq. (2-2) with the coefficient \mathcal{G} adapted to the cylindrical geometry and to the reference position $r = r_{\text{ref.}}$. The boundary conditions (1-27) read:

$$\mathbf{u}' = \mathbf{0}, \quad \theta' = \phi' = 0 \quad \text{at} \quad r = r_1, r_2. \quad (3-2)$$

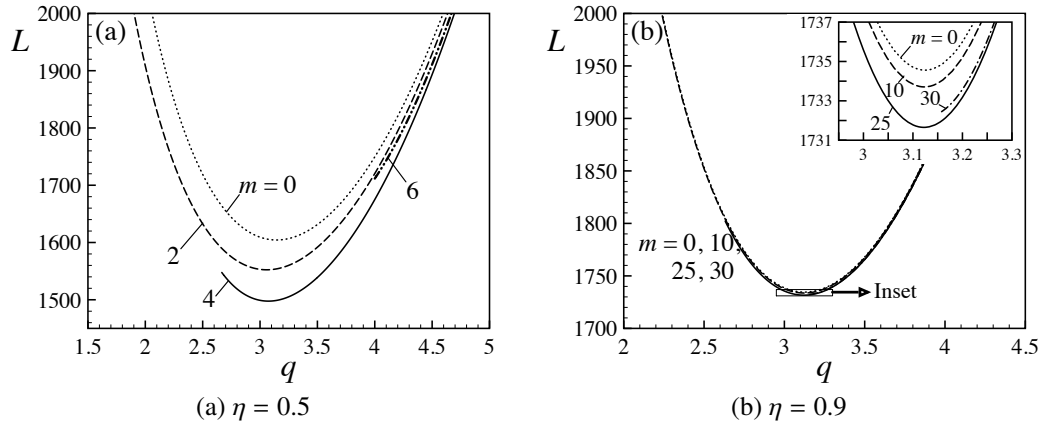


Figure 3-2: Marginal curves for different azimuthal modes in geometries of small and large radius ratios η ($\gamma_e = 0.01$).

We assume cylinders of infinite length. The stability of the conductive state can then be determined by considering normal mode perturbation fields $\exp[st + im\varphi + ikz]$, where $s = \sigma - i\omega$ is the complex growth rate (σ : the growth rate; ω : the frequency), m is the azimuthal mode number, and k is the axial wavenumber. The azimuthal and axial coordinates are denoted by φ and z , respectively. For this mode, the governing Eqs. (2-1) forms an eigenvalue problem $\mathbf{A}\mathbf{X} = s\mathbf{B}\mathbf{X}$, where $\mathbf{X} = [\hat{\mathbf{u}}' \hat{\pi}' \hat{\theta}' \hat{\phi}']^T$ is the complex amplitude of the normal mode and \mathbf{B} is a constant matrix. The differential matrix operator \mathbf{A} depends on the mode and wave numbers (m, k) and involves the parameters $(L, \eta, \gamma_e, \text{Pr})$. We solve this eigenvalue problem numerically by invoking a spectral collocation method based on the Chebyshev polynomials.

The eigenvalue s with the maximum real part crosses the imaginary axis in the complex plane at a certain value of L for given (m, k) and for given parameters $(\eta, \gamma_e, \text{Pr})$. Determining this value of L with varying the wavenumber k , we obtain the marginal stability curve $L = L(k)$ for the azimuthal mode m .

Figure 3-2 shows marginal curves at small and large η for different azimuthal modes. The abscissas are the

total wavenumber q (Fig. 3-3) that is computed from the axial wavenumber k and the azimuthal wavenumber k_φ estimated at the reference radial position r_{ref} . (Eq. 3-1):

$$q = \sqrt{k^2 + k_\varphi^2} \quad \text{with} \quad k_\varphi = \frac{m}{r_{\text{ref}}}. \quad (3-3)$$

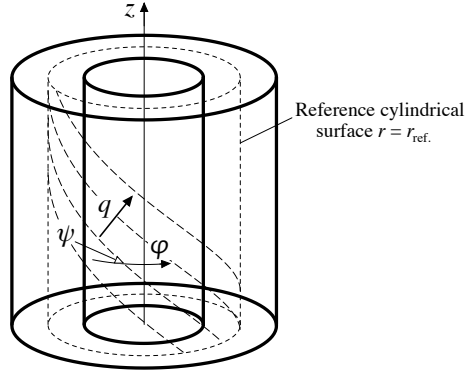


Figure 3-3: Definitions of the total wavenumber q and the inclination angle ψ

In Fig. 3-2, certain curves end at finite values of q , since $q \geq |k_\varphi| > 0$ for non-axisymmetric modes ($m \neq 0$). Marginal curves for different azimuthal modes are distinct from each other at small η (Fig. 3-2a), while mode degeneration is observed at large η (Fig. 3-2b). The degeneration reflects the fact that, as $\eta \rightarrow 1$, the annular geometry approaches a plane geometry where no distinction between axial and azimuthal direction is possible. Instability is found to be stationary ($\omega = 0$), as in the TEHD convection in plane geometry (Chap. 2). This implies that the marginal curves are independent from the Prandtl number Pr (see the argument given in the paragraph *Critical parameters* in Sec. 2.2). For characterizing the stability of the conductive state, we need hence explore only the parameter plane (η, γ_e) .

Seeking marginal curves for different azimuthal modes m in different zones of the η - γ_e plane, we find no instability in Zones II & III in the electric gravity diagram (Fig. 1-1). The conductive state is hence stable in inward heating except in the case where the electric gravity is centrifugal throughout the fluid layer (Zone IV). The stability in Zone II can be understood from the gravito-EHD analogy. The temperature gradient is opposed to the electric gravity in this zone so that the buoyancy due to the electric gravity attenuates perturbations. The stability in Zone III is associated with the thermoelectric feedback, as we will reveal it later by an energetic analysis.

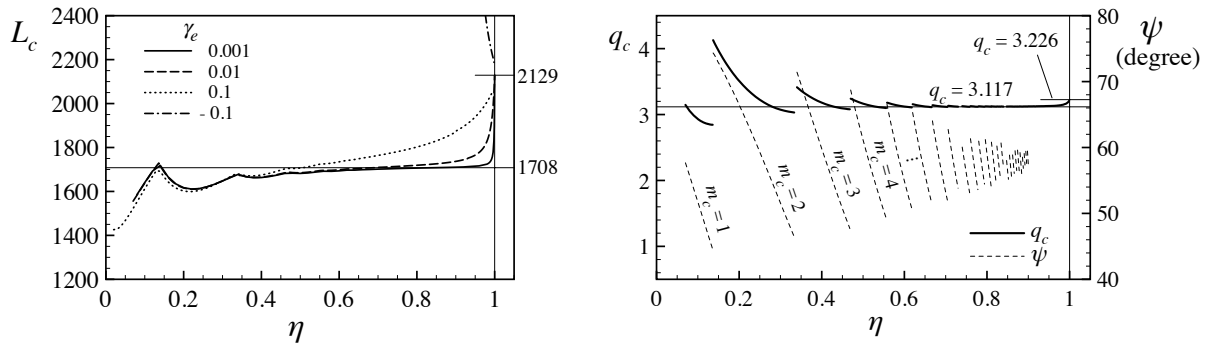


Figure 3-4: Critical parameters: (a) the electric Rayleigh number for different γ_e and (b) the wavenumber and the inclination angle of critical modes.

For given (η, γ_e) in other parameter zones than Zones II & III, we seek the azimuthal mode $m = m_c$ that gives the lowest marginal curve. Determining the minimum of this marginal curve, we obtain the critical parameters (m_c, q_c, L_c) . Figure 3-4 shows L_c and the total wavenumber $k = q_c$ of the critical mode (m_c, k_c) . The inclination angle ψ (Fig. 3-3) of the convection rolls at the reference position r_{ref} is also plotted: $\psi = \arctan(k_\phi/k)$. The critical mode is non axisymmetric independently from η and γ_e , except in the indeterminable case at large η due to the mode degeneration. For outward heating, i.e., in Zone I in the electric gravity diagram (Fig. 1-1), L_c and q_c take similar values to the critical parameters of the RB instability ($R_c = 1708$, $k_c^{RB} = 3.117$). Discontinuities seen in the q_c -curves correspond to changes of the critical azimuthal mode number m_c . When η approaches the unity, the curves of L_c and q_c converge to their values in the plane geometry, as expected. For inward heating ($\gamma_e < 0$), the instability occurs in Zone IV, but with higher critical electric Rayleigh number L_c than in outward heating. As η decreases inside Zone IV, the critical Rayleigh number diverges at the boundary with Zone III where no instability is found. The critical wavenumber increases significantly with decreasing η . This behavior of L_c and q_c for inward heating agrees with Takashima's results [81].

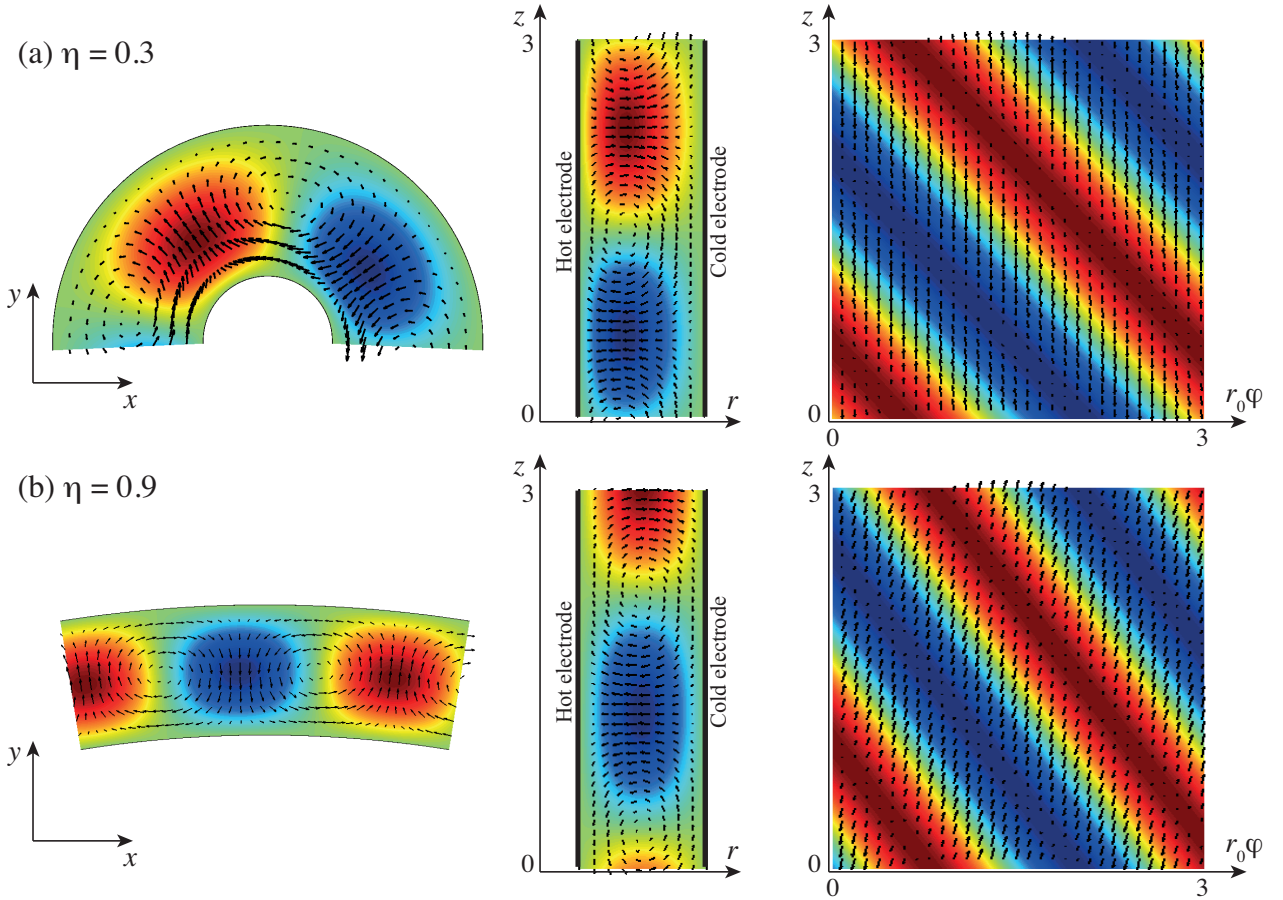


Figure 3-5: Critical eigenmodes for small and large radius ratios η . For $\eta = 0.3$, $m = 2$, $k = 1.91$ and $L = 1177$. For $\eta = 0.9$, $m = 25$, $k = 1.68$ and $L = 1732$. For both cases, the heating is outward ($\gamma_e = 0.01$) so that the electric gravity is centripetal. In the third column, the fields at the mid-gap are visualized with the coordinate $r_0\phi$, where r_0 is the mid-gap radial position.

Eigenfunctions

Eigenfunctions of the critical modes are shown in Fig. 3-5 for small and large η . In both cases, the inner cylinder is hotter than the outer one so that the electric gravity $\bar{\mathbf{g}}_e$ is centripetal (Zone I). Similar to ordinary thermal convections, flow goes radially outward against $\bar{\mathbf{g}}_e$ inside hot cells, while it does inward inside cold cells. At small η , fluid flow is concentrated in an inner region: the centers of convection rolls and temperature cells are found inner than the mid-gap. This justifies our choice of the reference position r_{ref} . (Eq. 3-1) to compute the electric Rayleigh number. The reference position $r = r_{\text{ref}}$ is found inner than the mid-gap and approaches the inner cylinder as η decreases. The electric gravity $\bar{\mathbf{g}}_e$ at $r = r_{\text{ref}}$ would be more representative than that at the mid-gap in geometries with small η .

Energetic analysis

In the analysis of the TEHD convection in plane geometry (Chap. 2), we revealed the role of the perturbation electric gravity by the evolution Eq. (2-5) of the kinetic energy. We can also apply this equation to the current cylindrical geometry. Figure 3-6 shows the powers W_{BG} and W_{PG} by the buoyancy forces associated with the base and perturbation electric gravities, $\bar{\mathbf{g}}_e$ and \mathbf{g}'_e , respectively. Both powers are computed for critical modes and normalized by the twice of the kinetic energy, $2K$ (see Eqs. 2-6 for the definitions of W_{BG} , W_{PG} , and K). As in the TEHD instability in plane geometry, the buoyancy due to $\bar{\mathbf{g}}_e$ is responsible for the destabilization ($W_{BG} > 0$), while the buoyancy associated with \mathbf{g}'_e is stabilizing ($W_{PG} < 0$). In inward heating ($\gamma_e > 0$), the contribution of W_{PG} is negligible at small η , while it becomes significant at large η . When $\eta \approx 1$, the magnitude of W_{PG} is around 20 % of W_{BG} as in the plane geometry case. This behavior of W_{PG} explains why the critical parameters (L_c, q_c) recovers the results of the RB instability at small η , although they converge to the values of the TEHD instability in plane geometry as $\eta \rightarrow 1$. Except for large η , the thermoelectric feedback is negligible in the TEHD instability in annular geometry. The TEHD instability at small η is hence an exact analogue to the ordinary thermal convection in a given radial gravity field $\mathbf{g} = \bar{\mathbf{g}}_e$. This validates the attempts to simulate geophysical flows by the TEHD instability.

In inward heating, the instability can occur only in Zone IV where η is large and the stabilizing effect of the perturbation electric gravity is significant. As η decreases, the stabilization becomes more and more important. The buoyancy due to $\bar{\mathbf{g}}_e$ cannot overcome this stabilization even in Zone III where the density stratification is potentially unstable in a sublayer against the base electric gravity $\bar{\mathbf{g}}_e$. The absence of the TEHD instability in Zone III arises from the dominance of the perturbation electric gravity over the base electric gravity.

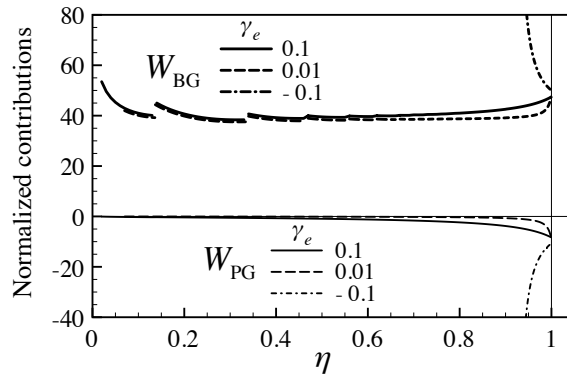


Figure 3-6: Energy transfer from the base to perturbation flows. The powers W_{BG} and W_{PG} by the buoyancy forces due to the base and perturbation electric gravities are computed for critical modes. Both powers are normalized by the twice of the kinetic energy K .

3.3 Conclusion

Existing theories on the TEHD instability in annular geometry have been concerned only with axisymmetric perturbations in small gap geometries ($\eta \gtrsim 0.9$). These limits disabling to explain experimental results were removed in the present work. We considered the whole area of the η - γ_e plain and showed the close relation of the stability with the behavior of the base electric gravity, e.g., with the electric gravity diagram (Fig. 1-1). The instability occurs only in Zones I & IV, where the base electric gravity $\bar{\mathbf{g}}_e$ has the same direction as the imposed temperature gradient throughout the fluid layer. Our analysis also showed the non-axisymmetry of critical modes: the hypothesis of axisymmetric perturbations will overestimate the instability threshold, in particular at small η . We examined the energy transfer process from the base to perturbation flows by an evolution Eq. (2-5) of the kinetic energy. An important conclusion was derived: the gravito-EHD analogy is exact at small η , where the thermoelectric feedback, i.e., the perturbation electric gravity \mathbf{g}'_e , is negligible. This conclusion validates the geophysical application of the TEHD convection.

The negligibility of the thermoelectric feedback at small η would hold even in the nonlinear flow regime. Recently, Travnikov et al. [86] realized a direct numerical simulation for different fluids of different Prandtl numbers ($0.7 \leq \text{Pr} \leq 100$) in geometries with small η ($0.1 \leq \eta \leq 0.5$). They confirmed the development of non-axisymmetric convection rolls and computed heat transfer. The coefficient a of the heat transfer improvement, i.e., a in the relationship $Nu = 1 + a(L/L_c - 1)$, is significantly larger than in the plan geometry case. For example, $a = 1.42$ for $\eta = 0.5$ and $\text{Pr} \gtrsim 1$. In plane geometry, the coefficient a takes a small value 0.78 for $\text{Pr} \gtrsim 1$, as a consequence of the impeding effects of the thermoelectric feedback (Sec. 2.4). The large values of a obtained by Travnikov et al. [86] are comparable with the coefficient for the RB instability ($a^{RB} = 1.43$) and would indicate that the perturbation electric gravity is negligible in nonlinear convection in curved geometries of small η .

Part II

Taylor-Couette flow with radial thermal body forces

Chapter 4

Taylor-Couette flow with a radial temperature gradient

Theoretical investigation on the stability of the flow in a vertical non-isothermal Taylor-Couette system is reported. The considered flow is induced by differential heating of the cylinders and by the inner cylinder rotation. This investigation was started in 2013 in collaboration with Antoine Meyer (LOMC), Innocent Mutabazi (LOMC), and Masato Nagata (University of Tianjin). Some results were communicated at different conferences and published in *Phys. Fluids* [101]. The latter article is included in appendix C.

4.1 Introduction

Heat removal through fluid between stationary and rotating elements is one of the keys for efficient and reliable operation of mechanical systems [5, 43, 47]. For controlling heat transfer between the elements, it is important to explore the conditions under which vortices emerge due to an instability from non-vortical flow at low Reynolds number. A prototype of such systems is a Taylor-Couette flow between two coaxial cylinders with a radial temperature gradient and with the inner cylinder rotating.

In this axisymmetric system, the fluid is stratified in density and viscosity, as they vary with the fluid temperature T . If the temperature variation is small, the fluid flow can be modeled by the following continuity and momentum equations in the Boussinesq approximation:

$$\frac{\partial u}{\partial r} + \frac{1}{r} \frac{\partial v}{\partial \varphi} + \frac{\partial w}{\partial z} = 0, \quad (4-1a)$$

$$\rho_{\text{ref.}} \frac{\partial u}{\partial t} + \rho_{\text{ref.}} u \frac{\partial u}{\partial r} + \frac{\rho_{\text{ref.}} v}{r} \frac{\partial u}{\partial \varphi} + \rho_{\text{ref.}} \frac{\partial u}{\partial z} - \rho(\theta) \frac{v^2}{r} = -\frac{\partial p}{\partial r} + \rho_{\text{ref.}} \nu_{\text{ref.}} \left(\Delta u - \frac{u}{r^2} - \frac{2}{r^2} \frac{\partial v}{\partial \varphi} \right) \quad (4-1b)$$

$$\rho_{\text{ref.}} \frac{\partial v}{\partial t} + \rho_{\text{ref.}} u \frac{\partial v}{\partial r} + \frac{\rho_{\text{ref.}} v}{r} \frac{\partial v}{\partial \varphi} + \rho_{\text{ref.}} \frac{\partial v}{\partial z} = -\frac{1}{r} \frac{\partial p}{\partial \varphi} + \rho_{\text{ref.}} \nu_{\text{ref.}} \left(\Delta v - \frac{v}{r^2} + \frac{2}{r^2} \frac{\partial u}{\partial \varphi} \right) \quad (4-1c)$$

$$\rho_{\text{ref.}} \frac{\partial w}{\partial t} + \rho_{\text{ref.}} u \frac{\partial w}{\partial r} + \frac{\rho_{\text{ref.}} v}{r} \frac{\partial w}{\partial \varphi} + \rho_{\text{ref.}} \frac{\partial w}{\partial z} = -\frac{\partial p}{\partial z} + \rho_{\text{ref.}} \nu_{\text{ref.}} \Delta w - \rho(\theta) g, \quad (4-1d)$$

where (u, v, w) are the radial, azimuthal and axial components of the velocity field. The Laplacian operator in the cylindrical coordinates (r, φ, z) for scalars is designated by Δ : $\Delta = \partial_r^2 + \frac{1}{r} \partial_r + \frac{1}{r^2} \partial_\varphi^2 + \partial_z^2$. The fluid density and kinematic viscosity are denoted by ρ and ν , respectively. The subscript ref. means “at a reference temperature $T = T_{\text{ref.}}$ ” and θ is the deviation of the fluid temperature T from the reference temperature: $\theta = T - T_{\text{ref.}}$. The gravitational acceleration g has been assumed to be directed in the negative z direction.

The temperature dependence of the density $\rho(\theta) = \rho_{\text{ref.}}(1 - \alpha\theta)$ is retained only in the terms involving either the acceleration v^2/r or the gravity g , since the fluid acceleration induced by these terms can be significant compared with the effects of other terms even for a small θ . Equations (4-1b)–(4-1d) can be written in a vectorial form:

$$\rho \left(\frac{\partial \mathbf{u}}{\partial t} + \mathbf{u} \cdot \nabla \mathbf{u} \right) = -\nabla \pi + \rho \nu \nabla^2 \mathbf{u} - \rho \alpha \theta (\mathbf{g}_c + \mathbf{g}) \quad (4-2)$$

where \mathbf{g}_c stands for the centrifugal acceleration: $\mathbf{g}_c = (v^2/r) \mathbf{e}_r$ and π is the generalized pressure: $\pi = p + \rho \mathbf{g} \cdot \mathbf{r}$ (\mathbf{r} : the position vector). In Eq. (4-2), the subscript ref. has been omitted. The last term in Eq. (4-2) consists of two parts: the first one, $-\rho \alpha \theta \mathbf{g}_c$, is the thermal buoyancy force arising from the centrifugal acceleration \mathbf{g}_c and the second one, $-\rho \alpha \theta \mathbf{g}$, is the thermal Archimedean buoyancy force due to the Earth's gravity \mathbf{g} . We call the former *the centrifugal buoyancy force* to underline the origin of this buoyancy, although its direction can be centripetal or centrifugal depending on the temperature deviation θ .

The stability of Taylor-Couette flow with radial heating has been investigated both experimentally and theoretically. In an experiment with a small gap of radius ratio $\eta = 0.958$ and with different fluids of Prandtl number $\text{Pr} \approx 5$ and 19, Snyder & Karlsson [75] found that a temperature difference ΔT imposed on the system stabilized the flow if its magnitude $|\Delta T|$ is small, while it was destabilizing for large $|\Delta T|$. In the stabilizing temperature range, toroidal vortices were observed. Spiral flow consisting of pairs of counter rotating vortices of uneven sizes was observed in the destabilizing temperature range. The wavelength of this flow pattern was almost constant, while the azimuthal wavenumber varied with ΔT . The flow pattern moved in the azimuthal direction with an angular velocity almost the half of the inner cylinder rotation speed. Sorour & Coney [76] performed experiments also in small gap geometries ($\eta = 0.911$ or 0.948). Their fluid was viscous oil with the kinematic viscosity either $\nu = 41 \text{ mm}^2/\text{s}$ or $\nu = 75 \text{ mm}^2/\text{s}$. They found continuous destabilization with increasing $|\Delta T|$. The observed toroidal flow consisted of uneven sized vortices. Lepiller et al. [49] performed an experiment in wide gap geometry ($\eta = 0.8$) with deionized water ($\text{Pr} = 5.5$). Their experiment showed continuous destabilization with increasing temperature difference independently of its sign. The observed flow was spiral. The size of the spiral vortices increased with ΔT until a certain value, beyond which flow pattern became insensitive to further increase of the temperature difference.

Theoretical studies of non-isothermal Taylor-Couette flows have been based on the Boussinesq approximation, i.e., on the continuity Eq. (4-1a) and the momentum Eq. (4-2). Many of them assumed axisymmetric perturbations so that experimentally observed spiral vortices could not be explained by these theories. Furthermore, other assumptions were often made. Some of the existing investigations were concerned only with the case where the thermal Archimedean buoyancy is negligible [2, 3, 25, 26, 41, 49, 51, 75, 78, 83, 89, 93], because of the interests in particular flow systems (e.g., centrifugal pumps used in microgravity environments) and in astrophysical applications. It was shown that the role of the temperature gradient on the flow stability was dependent of the geometry (i.e., the radius ratio η) and the fluid diffusion properties (i.e., the Prandtl number Pr) [41, 78, 83, 89]. Only a few of the existing studies [25, 75] highlighted the sensitivity of the flow behavior to the heating direction. A thorough linear stability analysis has been performed by Ali & Weidman [1] for both axisymmetric and non-axisymmetric perturbations with varying the radius ratio η and the Prandtl number Pr . Inward heating (i.e., the outer cylinder is hotter than the inner one) as well as outward heating (i.e., the inner cylinder is hotter than the outer one) were considered. The theoretical model took into account the Archimedean buoyancy, but neglected the centrifugal buoyancy. The stabilization by the temperature gradient was shown to depend both on η and Pr . The authors discussed the symmetry properties of their theoretical model and derived important conclusions: the stability of the system is independent of the heating direction, while the axial phase velocity of perturbation flow changes the sign

if the heating direction is inverted. These conclusions are consistent with the experiment of Lepiller et al. [49], but inconsistent with the results of Snyder & Karlsson [75]. The latter authors found that their flow system was more stable in outward heating than in inward heating.

In the existing theoretical studies, there are discrepancies between them regarding the stabilizing temperature effect and the sensitivity to the heating direction. Furthermore, the centrifugal buoyancy has not been taken into account in any theories for non-axisymmetric perturbations. We revisit the linear stability problem of non-isothermal Taylor-Couette flows, considering a system with inner and outer cylinders maintained at temperatures T_1 and T_2 , respectively (Fig. 4-1a). Only the inner cylinder rotates with an angular velocity Ω . We employ the full momentum Eq. (4-2) in the Boussinesq approximation, with the centrifugal and Archimedean thermal buoyancy terms. We examine the stability against axisymmetric and non-axisymmetric perturbations. In order to clarify the effects of the heating direction, both outward and inward heatings are considered by setting the temperature difference $\Delta T = T_1 - T_2$ at positive and negative values. The results reported in the present chapter are concerned mainly with a particular geometry of $\eta = 0.8$, which corresponds to the experiment of Lepiller et al. [49].

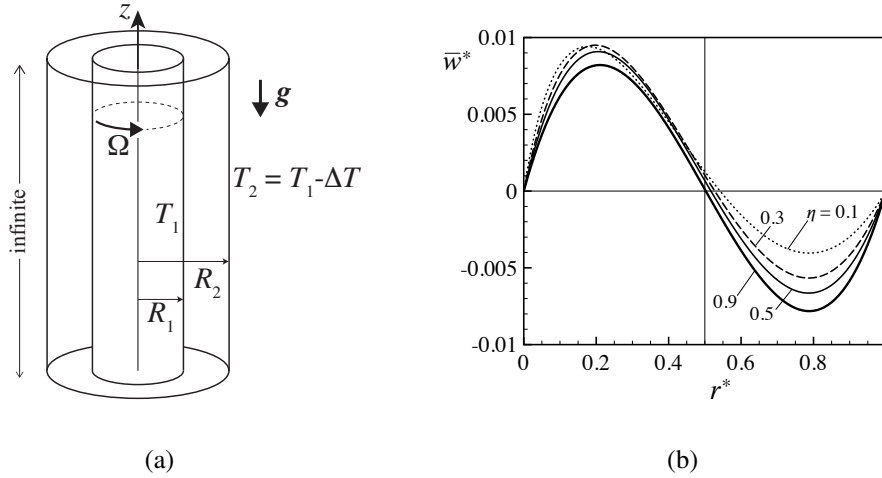


Figure 4-1: A non-isothermal Taylor-Couette flow. (a) Schematic illustration of the considered system. (b) Normalized vertical velocity in the conductive state $\bar{w}^* = \bar{w}/Gr$ for different values of the radius ratio η . The abscissa r^* is the normalized shifted coordinate: $r^* = r - r_1$. The origin of r^* coincides with the inner cylinder, while $r^* = 1$ corresponds to the outer cylinder position.

Nondimensionalized governing equations and dimensionless parameters

Our theoretical model is based on the continuity and momentum equations in the Boussinesq approximation, Eqs. (4-1a) & (4-2), as well as the heat conduction equation. Nondimensionalizing them with the scales d ($= R_2 - R_1$) of length, $\tau_v = d^2/\nu$ of time, d/τ_v of velocity and ΔT of temperature, we have

$$\nabla \cdot \mathbf{u} = 0, \quad (4-3a)$$

$$\frac{\partial \mathbf{u}}{\partial t} + \mathbf{u} \cdot \nabla \mathbf{u} = -\nabla \pi + \nabla^2 \mathbf{u} - Gr F^2 \theta g_c \mathbf{e}_r + Gr \theta \mathbf{e}_z \quad (4-3b)$$

$$\frac{\partial \theta}{\partial t} + \mathbf{u} \cdot \nabla \theta = \frac{1}{Pr} \nabla^2 \theta, \quad (4-3c)$$

where $g_c = v^2/r$ is the dimensionless centrifugal acceleration. In the heat conduction Eq. (4-3c), the viscous heating has been neglected. The boundary conditions on the inner and outer cylinders are given by

$$\mathbf{u} = \sqrt{\frac{\eta}{1-\eta}} \text{Ta} \mathbf{e}_\varphi, \quad \theta = 1 \quad \text{at } r = r_1; \quad \mathbf{u} = \mathbf{0}, \quad \theta = 0 \quad \text{at } r = r_2, \quad (4-3d)$$

where r_1 and r_2 are the coordinates of the inner and outer cylinders: $r_1 = \eta/(1-\eta)$ and $r_2 = 1/(1-\eta)$.

The Taylor number and the Grashof number as well as another dimensionless number F have been introduced:

$$\text{Ta} = \frac{R_1 \Omega d}{\nu} \sqrt{\frac{d}{R_1}}, \quad \text{Gr} = \frac{\alpha \Delta T g d^3}{\nu^2}, \quad \text{F} = \frac{\nu}{\sqrt{g d^3}}. \quad (4-4)$$

A positive value of the Grashof number Gr implies outward heating, while a negative Gr means inward heating. The parameter F depends on the geometry and the fluid viscosity only. It represents the relative importance of the centrifugal buoyancy to the Archimedean buoyancy. The square of F is identical to the inverse of the Galileo number $\text{Ga} = g d^3 / \nu$.

4.2 Conductive state

Even in the absence of the cylinder rotation, differential heating by cylinders creates fluid vertical motion. The fluid rises and falls in the vicinity of hot and cold cylinders, respectively. For a cylinder annulus of large height Γd ($\Gamma > \text{Pr Gr}/400$), this vertical flow is in the conduction regime [1] and homogeneous in the azimuthal and axial directions.

Supposing this homogeneity in the φ and z directions, we can determine the flow state from Eqs. (4-3a)–(4-3d) when both inner cylinder rotation and differential heating are applied to the system. The velocity and temperature fields $(\bar{\mathbf{u}}, \bar{\theta})$ are given by

$$\bar{\mathbf{u}} = \bar{v}(r) \mathbf{e}_\varphi + \bar{w}(r) \mathbf{e}_z, \quad \bar{\theta} = \frac{\log(1-\eta)r}{\log \eta} \quad \text{with} \quad (4-5a)$$

$$\bar{v} = \frac{\eta^{3/2} \text{Ta}}{(1-\eta)^{5/2} (1+\eta)} \left[\frac{1}{r} - (1-\eta)^2 r \right] \quad (4-5b)$$

$$\bar{w} = \text{Gr} \left(C \left[(1-\eta)^2 r^2 - 1 + (1-\eta^2) \bar{\theta} \right] - \frac{r^2 (1-\eta)^2 - \eta^2 \bar{\theta}}{4(1-\eta)^2} \right). \quad (4-5c)$$

The coefficient C is a function of η (see Eq. 16 in Yoshikawa et al. [101] for an explicit expression of C). During the determination of the vertical velocity component \bar{w} , the following no net flux condition has been used:

$$\int_0^{2\pi} d\varphi \int_{r_1}^{r_2} dr r \bar{w} = 0. \quad (4-6)$$

The profiles of the velocity components and the temperature in this conductive state depend only on the radius ratio η . The velocity \bar{v} is identical to the classical circular Couette flow generated by the inner cylinder rotation. Some profiles of the axial velocity \bar{w} are shown in Fig. 4-1(b), where the normalized vertical velocity $\bar{w}^* = \bar{w}/\text{Gr}$ is shown as function of the shifted coordinate $r^* = r - r_1$. The profile \bar{w} is almost antisymmetric at large η with respect to the mid-gap, while the flow is concentrated in an inner region at small η . As \bar{w}^* depends only on η , the shape of the velocity profile at a given η is the same for any value of Gr. When Gr is negative, the profile is the same as that for $|\text{Gr}|$, but the flow direction is inverted.

4.3 Linear stability analysis

The evolution of small perturbations (\mathbf{u}', θ') is governed by Eqs. (4-3) linearized around the conductive state (4-5):

$$\nabla \cdot \mathbf{u}' = 0, \quad (4-7a)$$

$$\frac{\partial \mathbf{u}'}{\partial t} + \bar{\mathbf{u}} \cdot \nabla \mathbf{u}' + \mathbf{u}' \cdot \nabla \bar{\mathbf{u}} = -\nabla \pi' + \nabla^2 \mathbf{u}' - \text{Gr} F^2 \left(\theta' G_c + \bar{\theta} \frac{2\bar{v}v'}{r} \right) \mathbf{e}_r + \text{Gr} \theta' \mathbf{e}_z \quad (4-7b)$$

$$\frac{\partial \theta'}{\partial t} + \bar{\mathbf{u}} \cdot \nabla \theta' + \mathbf{u}' \cdot \nabla \bar{\theta} = \frac{1}{\text{Pr}} \Delta \theta', \quad (4-7c)$$

where G_c is the centrifugal acceleration in the base conductive state: $G_c = \bar{v}^2/r$. The boundary conditions (4-3d) read for perturbation fields:

$$\mathbf{u}' = 0, \quad \theta' = 0 \text{ at } r = r_1, r_2. \quad (4-7d)$$

Assuming cylinders of infinite length, we can determine the stability of the conductive state by considering the linearized governing equations (4-7) for a normal mode $\exp[st + im\varphi + ikz]$, where $s = \sigma - i\omega$ is the complex growth rate (σ : the growth rate; ω : the frequency), m is the azimuthal mode number, and k is the axial wavenumber. For this mode, the governing equations form an eigenvalue problem $\mathbf{A}\mathbf{X} = s\mathbf{B}\mathbf{X}$, where $\mathbf{X} = [\hat{u}' \ \hat{\pi}' \ \hat{\theta}' \ \hat{\phi}']^T$ is the complex amplitude of the normal mode and \mathbf{B} is a constant matrix. The differential matrix operator \mathbf{A} depends on the mode and wave numbers (m, k) and involves the parameters $(\text{Ta}, \eta, \text{Pr}, F)$. We solve this eigenvalue problem numerically by invoking a spectral collocation method based on the Chebyshev polynomials.

The determined eigenvalue s with the maximum real part crosses the imaginary axis in the complex plane at a certain value of Ta for given (m, k) and for given parameters (η, Pr, F) . Seeking this value of Ta with varying the wavenumber k , we obtain the marginal stability curve $\text{Ta} = \text{Ta}(k)$ for the azimuthal mode m . The critical parameters $(\omega_c, k_c, m_c, \text{Ta}_c)$ are given by the lowest minimum among the marginal curves for different m , where ω_c is the critical frequency.

Results for a small F

We consider a particular case corresponding to the experiment of Lepiller et al. [49], where $\eta = 0.8$, $\text{Pr} = 5.5$ and $F = 7.3 \times 10^{-4}$. This small value of F indicates that the effects of the centrifugal buoyancy would be weak. According to Ali & Weidman [1], if the centrifugal buoyancy is negligible, the stability should exhibit symmetry with respect to the heating direction, i.e., the critical Taylor number for a given Grashof number Gr should be identical to that for the corresponding negative Grashof number: $\text{Ta}_c(\text{Gr}) = \text{Ta}_c(-\text{Gr})$. Indeed, the determined critical Taylor number shows this symmetry (Fig. 4-2a). The total wavenumber q of the critical mode also exhibits the symmetry with respect to the heating direction (Fig. 4-2b). In contrast, the inclination angle ψ of the critical mode and the axial phase velocity $c_z = \omega_c/k_c$ are antisymmetric (Fig. 4-2cd), where the total wavenumber q and the inclination angle ψ have been estimated at the mid-gap $r = r_0$ by

$$q = \sqrt{k^2 + k_\varphi^2} \quad \text{with} \quad k_\varphi = \frac{m}{r_0}; \quad \psi = \arctan \frac{k_\varphi}{k}. \quad (4-8)$$

With increasing the magnitude of Gr from 0, the conductive state is first stabilized (Fig. 4-2a), where the critical mode is axisymmetric and has a small frequency proportional to Gr : $\omega_c = -0.006\text{Gr}$. This stabilized range ($|\text{Gr}| < 23$) could not be identified by Lepiller et al. [49], since the smallest $|\text{Gr}|$ in their non-isothermal experiments was around 160. At Gr larger than 23, the destabilization by heating is observed. The critical mode is non axisymmetric and its mode number m_c is negative and positive for $\text{Gr} > 23$ and $\text{Gr} < -23$, respectively. The magnitude $|m_c|$

increases with increasing $|Gr|$. For $|Gr| \gtrsim 1700$, the critical mode number becomes constant ($m_c = \pm 10$). The Taylor number also becomes almost constant and the wavenumber and the inclination angle vary slightly (Fig. 4-2bc). Once $|Gr|$ attains 7930, the critical mode becomes again axisymmetric and Ta_c decreases toward zero, where the flow is driven only by the differential heating of cylinders.

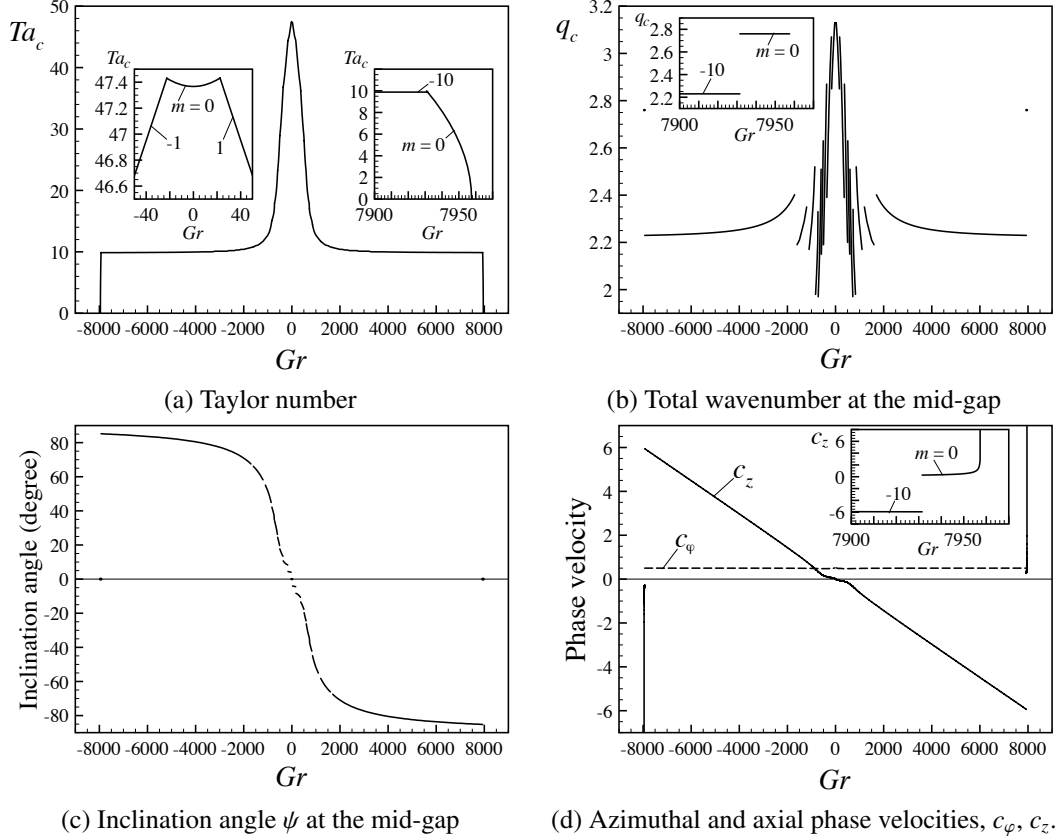


Figure 4-2: Critical parameters for $\eta = 0.8$, $Pr = 5.5$, and $F = 7.3 \times 10^{-4}$.

Eigenfunctions at different Gr are shown in Fig. 4-3. When the mode is axisymmetric at small $|Gr|$, vortices are circular and no inclination of temperature cells are observed (Panel a1). With increasing $|Gr|$ beyond 23 where the flow is non axisymmetric, vortices are deformed and temperature cells are inclined (Panels a2&a3). Beyond $|Gr| = 7930$, the eigenmode returns to be axisymmetric, but flow is more complex than the axisymmetric flow at small $|Gr|$ (Panel a4). Temperature cells are inclined steeply. Panel (b) shows two flow states at the codimension-two point $(Gr, Ta) = (7932, 9.88)$, where non-axisymmetric mode with $m_c = -10$ and axisymmetric mode are both critical.

The roles of different forces in the instability can be clarified by the evolution equation of the kinetic energy, as we employed it for the TEHD instability (Chaps. 2 & 3). This equation for the present problem can be obtained from the linearized momentum equation (4-7b) and is given by

$$\frac{dK}{dt} = W_{Ta} + W_{Hy} + W_\theta + W_C - D_v, \quad (4-9)$$

where K is the kinetic energy of perturbation flow. The first term W_{Ta} in the right-hand-side represents the power by the centrifugal force that is responsible for the centrifugal instability. The power W_{Hy} is produced by the Reynolds

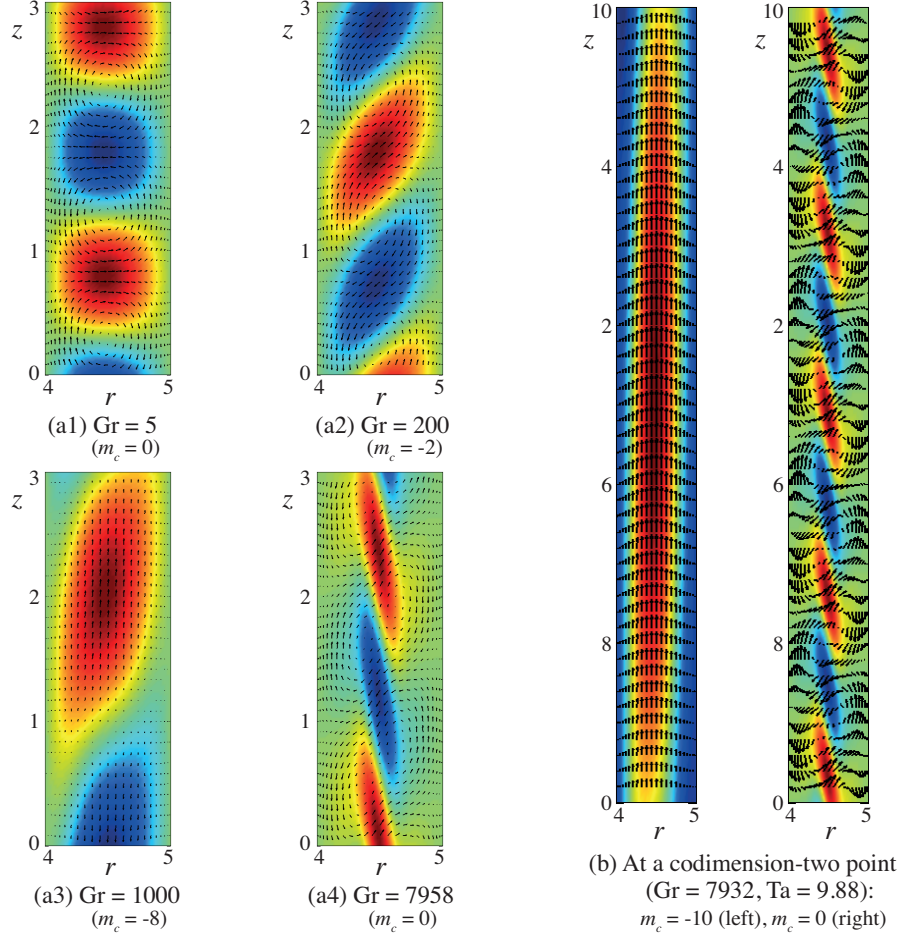


Figure 4-3: Critical eigenfunctions for $\eta = 0.8$, $\text{Pr} = 5.5$, and $F = 7.3 \times 10^{-4}$: Perturbation velocity and temperature fields are shown by arrows and colors, respectively.

stress on the baroclinic vorticity. The terms W_θ and W_C are the powers by the thermal Archimedean buoyancy and by the centrifugal buoyancy, respectively. The viscous energy dissipation rates is designated by D_v . The explicit definitions of these terms are

$$K = \left\langle \frac{1}{2} \mathbf{u}'^2 \right\rangle, \quad W_{Ta} = - \left\langle \left(\frac{d\bar{v}}{dr} - \frac{\bar{v}}{r} \right) u' v' \right\rangle, \quad W_{Hy} = - \left\langle \frac{d\bar{w}}{dr} u' w' \right\rangle, \quad (4-10a)$$

$$W_\theta = \text{Gr} \langle \theta' w' \rangle, \quad W_C = -\text{GrF}^2 \left\langle u' \frac{\bar{v}}{r} (\theta' \bar{v} + 2\bar{\theta} v') \right\rangle, \quad D_v = \langle \dot{\epsilon} : \dot{\epsilon} \rangle, \quad (4-10b)$$

where $\dot{\epsilon}$ is the rate-of-strain tensor. The angle brackets mean the following averaging and integration operation:

$$\langle \cdot \rangle = \frac{\omega}{2\pi} \int_0^{2\pi/\omega} dt \frac{1}{2\pi} \int_0^{2\pi} d\varphi \frac{k}{2\pi} \int_0^{2\pi/k} dz \quad \cdot, \quad (4-11)$$

where the averaging operations with respect to φ and t should be omitted for axisymmetric and stationary normal modes, respectively.

Computing these power terms at critical conditions, we can distinguish the force that plays the major role in the

energy transfer from the base to perturbation flows (Fig. 4-4). The stabilization at small $|\text{Gr}|$ (< 23) is due to the stabilization by the thermal Archimedean buoyancy on the axisymmetric mode. Indeed, W_θ takes negative values in this range of Gr . The drastic decrease of Ta_c within $30 < |\text{Gr}| < 2000$ is associated with the increasing destabilization by the thermal Archimedean buoyancy on non axisymmetric modes. The power W_θ increases with $|\text{Gr}|$. It is the major energy transfer mechanism for $|\text{Gr}| > 500$, while the power on the baroclinic vorticity, W_{Hy} , contributes also destabilization. When the $|\text{Gr}|$ attains 7930, the power W_{Hy} becomes dominant suddenly. This sudden change corresponds to the qualitative change of the eigenfunctions at the codimension-two point $|\text{Gr}| = 7930$ (Fig. 4-3b).

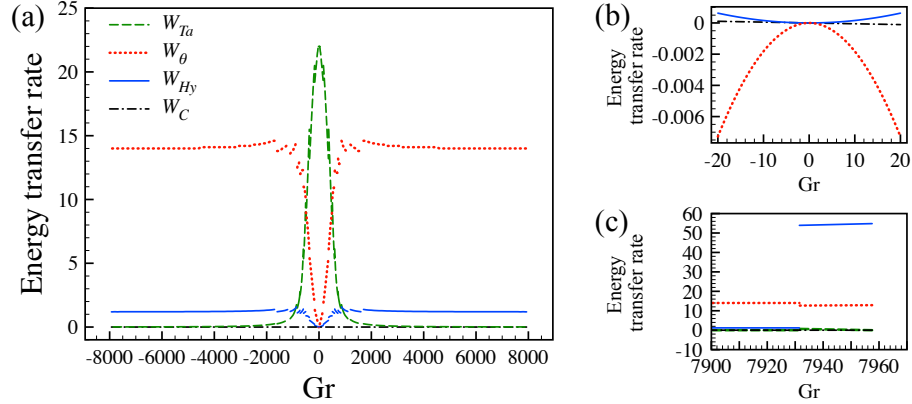


Figure 4-4: Power terms in the kinetic energy Eq. (4-9) normalized by the twice of the kinetic energy K ($\eta = 0.8$, $\text{Pr} = 5.5$, $F = 7.3 \times 10^{-4}$).

Results for large F

When the parameter F is large, the centrifugal buoyancy is important compared with the thermal Archimedean buoyancy. It will play a significant role in the instability mechanism and could break the symmetry of the stability with respect to the heating direction. In fact, as we saw in the analysis of the TEHD instability in cylindrical annular geometry (Chap. 3), a thermal buoyancy due to a radial acceleration field \mathbf{g}_e stabilizes a conductive fluid state when the temperature gradient is directed opposite to the acceleration. If the gradient is in the same direction as \mathbf{g}_e , the buoyancy is destabilizing. One can hence expect that the centrifugal buoyancy is stabilizing and destabilizing in outward and inward heating, respectively. Indeed, for large F , the critical Taylor number shows a clear tendency of increase and decrease for positive and negative values of Gr , respectively (Fig. 4-5a). An analysis of the energy transfer by Eq. (4-9) confirms that this symmetry breaking is due to the centrifugal buoyancy (Fig. 4-5b): the power W_C is negative and positive in outward and inward heating, respectively.

The centrifugal buoyancy can not only affect the instability threshold but also change the nature of critical flow. Figure 4-6(a) shows a phase diagram of the temporal and spatial nature of critical modes. For focusing on the effects of the centrifugal buoyancy, the diagram is drawn for the case where the Grashof number vanishes with keeping the product $\gamma_a = \text{Gr}F^2 = \alpha \Delta T$ finite. Since γ_e is independent of the gap size and the gravity, the situation of vanishing Gr with a finite γ_a can be realized by a system either with a tiny gap or in a microgravity environment. The diagram indicates clearly the asymmetry of the system behavior with respect to the heating direction. Oscillatory axisymmetric modes can emerge from the conductive state only in outward heating.

The oscillatory behavior of these modes in outward heating is not a consequence of the advection by the base flow, since the vortices are toroidal and the base flow has no axial velocity component for $\text{Gr} = 0$. The oscillation is

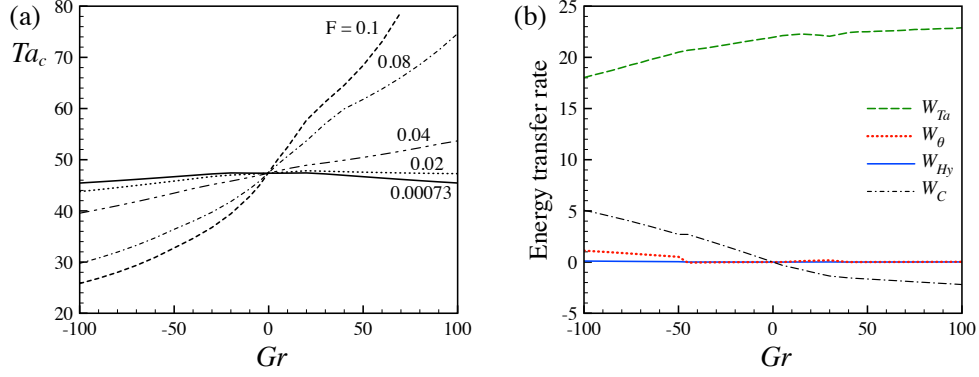


Figure 4-5: Stability for large F . (a) Critical Taylor number for different F . (b) Different power terms in the kinetic energy Eq. (4-9) computed for critical modes ($F = 0.08$, $\eta = 0.8$, $Pr = 5.5$).

related to internal waves propagating in a stratified fluid layer. In fact, the centrifugal buoyancy is stabilizing in outward heating. It follows that the buoyancy force has tendency to restore any fluid particle deviated from its equilibrium position. One may compute the buoyancy frequency N by comparing this restoring buoyancy force $(d\rho/dr)G_c\delta r = (d\rho/dr)(\bar{v}^2/r)\delta r$ with fluid inertia $\rho N^2\delta r$, where δr is a radial deviation of a fluid particle from its equilibrium position. The frequency N is hence given in dimensional form by

$$N^2 = \frac{G_c}{\rho} \frac{d\rho}{dr} = -\frac{\alpha \bar{v}^2}{r} \frac{d\bar{\theta}}{dr}. \quad (4-12)$$

This frequency takes a real value only in outward heating.

The critical frequencies of observed oscillatory axisymmetric modes are correlated well with N (Fig. 4-6b). The frequencies ω_c for different Prandtl numbers seem to be proportional to the buoyancy frequency, when $N > \tau_v^{-1}$, i.e., when the fluid viscosity does not influence significantly wave motion. This result suggests that the critical oscillatory modes arise from internal waves in a fluid with a stable stratification against the centrifugal acceleration field.

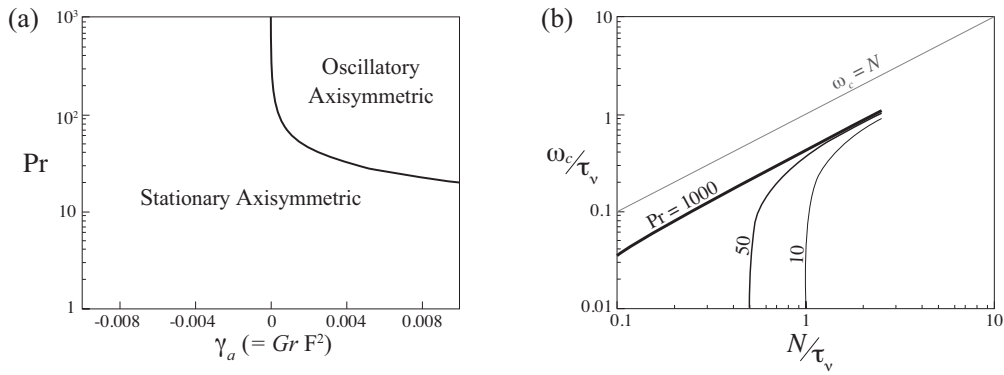


Figure 4-6: Generation of oscillatory axisymmetric (OA) flow by the centrifugal buoyancy: (a) Phase diagram indicating the parameter region for OA modes, (b) Comparison of the critical frequency with the buoyancy frequency. The radius ratio is fixed at $\eta = 0.5$.

4.4 Conclusion

The problem of the stability of a circular Couette flow with a radial temperature gradient was revisited. Our analysis clarified the role of the centrifugal buoyancy. For small values of the parameter $F = \nu / \sqrt{gd^3}$, this buoyancy is negligible compared with the thermal Archimedean buoyancy. The stability of the system is independent of the heating direction, as predicted by Ali & Weidman [1]. Heating stabilizes the conductive state at small temperature difference. For large values of F , the centrifugal buoyancy affects significantly the system behavior. The stability is sensitive to the heating direction: at small Gr , the system is more stable in outward heating than in inward heating. Our analysis also showed that the centrifugal buoyancy also modified significantly the nature of critical modes. Even in the absence of axial advection by the base flow (i.e., when Gr vanishes), oscillatory axisymmetric modes can develop from the conductive state in outward heating. The frequency of these modes is given by the buoyancy frequency based on the centrifugal acceleration. This result indicates a close relation of the oscillatory modes with the internal waves propagating in a stratified fluid layer.

Chapter 5

Taylor-Couette flows subjected to radial thermoelectric buoyancy

Theoretical investigations on the Taylor-Couette flows of a dielectric fluid subjected to a radial temperature gradient and a radial electric field are reported. This work was started in 2013 in collaboration with Antoine Meyer (LOMC) and Innocent Mutabazi (LOMC). Obtained results were presented in a number of conferences and published in *Phys. Rev. E* [100].

5.1 Introduction

In Taylor-Couette systems subjected to a radial temperature gradient (Chap. 4), the radial buoyancy force associated with centrifugal acceleration $\mathbf{g}_c = (v^2/r)\mathbf{e}_r$ can change significantly the stability of the conductive state and the flow behavior (v : the azimuthal flow velocity; r : the radial coordinate). Due to this force the behavior of the flow system loses the symmetry with respect to the heating direction. In fact, the thermal stratification in density is stable and potentially unstable in the centrifugal acceleration field \mathbf{g}_c in negative and positive radial temperature gradients, respectively. As a consequence, when the radial buoyancy force is significant compared with other effects, the conductive state is more and less stable than the isothermal flow in outward and inward heating, respectively.

We have considered in Chap. 3 the thermo-electrohydrodynamic (TEHD) convection in cylindrical annular geometry, which was induced by a radial thermal buoyancy associated with a radial acceleration field \mathbf{g}_e called *electric gravity*. If this electric gravity is applied to a no-isothermal Taylor-Couette system, it would change the system behavior as the centrifugal acceleration does so. Since the electric gravity can be adjusted to a desired value by varying the electric tension applied to the cylinders, we would be able to control the Taylor-Couette flow. This control can be used for enhancing the heat transfer in rotating machines. Such fluid systems are also of interest in geo- and astro-physics, where convective flows and stratified shear flows in the central gravity field are of primary importance.

The stability of the Taylor-Couette flow subjected to a radial thermal buoyancy force other than the centrifugal one has been investigated theoretically. Stiles et al. [78] considered a flow induced by the inner cylinder rotation, restricting their analysis to axisymmetric steady perturbations in a small gap geometry. Only outward heating was considered. They found that the critical Taylor number dropped effectively with increasing the temperature difference. Tagg & Weidman [80] considered a magnetic fluid in a vertical Taylor-Couette system with only the inner cylinder rotating. The thermal variation of the magnetization leads to a thermomagnetic body force density, which can be viewed as a thermal buoyancy force associated with a magnetic effective gravity in the radial direction. The

authors analyzed the linear stability of the base flow driven both by the inner cylinder rotation and by the differential heating under the Earth's gravity. Both axisymmetric and non-axisymmetric perturbations were considered. The behavior of the critical parameters in function of the Grashof number was examined. Outward heating was found to destabilize the flow significantly when the thermomagnetic buoyancy force was of the same order of magnitude as the thermal Archimedean force. When the heating direction was inverted, the thermomagnetic force had significant stabilizing effects.

In these existing theoretical investigations, oscillatory critical modes have not been highlighted. Although Tagg & Weidman [80] found oscillatory modes in the thermomagnetic Taylor-Couette flows, the origin of the oscillation was not discussed. Our investigation is intended to examine the effects of the radial thermoelectric buoyancy on the behavior of non-isothermal Taylor-Couette flows. In particular, we are interested in how this buoyancy affects the nature of critical modes. In fact, as shown in the electric gravity diagram in Fig. 1-1, the direction of the electric gravity $\bar{\mathbf{g}}_e$ in a curved geometry depends on the radius ratio η of inner to outer cylinder radii and the thermoelectric parameter $\gamma_e = e\Delta T$ that characterizes the stratification of a fluid layer in dielectric permittivity (ΔT : the temperature difference between the cylinders; for the definition of e , see Eq. 1-3). When the temperature gradient and the electric gravity are opposite to each other, i.e., in Zone II of the diagram, the density stratification is stable in the electric gravity field. In this situation, the thermoelectric buoyancy force has a tendency to restore any deviated fluid particle to its equilibrium position. We can expect that the inner cylinder rotation then provokes an oscillatory instability, as we found oscillatory modes in non isothermal Taylor-Couette flows in Chap. 4. The frequency of growing oscillatory perturbations would be associated with the buoyancy frequency N based on the thermoelectric buoyancy force. Such oscillatory instability has not been reported in the existing studies [78, 80].¹

We perform a linear stability analysis based on a theoretical model that takes into account not only the thermoelectric buoyancy but also the centrifugal buoyancy, i.e., the thermal buoyancy due to the centrifugal acceleration \mathbf{g}_c . In order to focus on these radial thermal buoyancy forces, the analysis is restricted to the situation where the Earth's gravity is negligible. Different from the existing study [78], we consider arbitrary perturbations and both inward and outward heating. The results presented in this chapter are concerned only with the centripetal electric gravity configuration, i.e., with only Zones I & II in the electric gravity diagram (Fig. 1-1). This case is the most relevant to the application in geo- and astro-physics. Results in the other electric gravity configurations are reported in Yoshikawa et al. [100].

Governing equations

We consider the Taylor-Couette flow of a dielectric fluid within the gap between two concentric cylindrical electrodes of infinite length (Fig. 5-1a). The inner cylinder of radius R_1 is maintained at a constant uniform temperature T_1 , while the outer cylinder of radius R_2 is kept at T_2 . An alternative electric tension $V(t) = \sqrt{2}\Phi_0 \sin(2\pi ft)$ is applied to the gap. The flow is induced by the inner cylinder rotation with an angular velocity Ω .

Non-isothermal Taylor-Couette flows can be modeled by the set of governing Eqs. (4-3) in the Boussinesq approximation, if the temperature variation is small. Taking into account the EHD force (Eq. 1-7a) as an external force in the momentum equation and adding the Gauss' law of electricity to the equation set, we have the following system of equations that governs the Taylor-Couette flow subjected to both centrifugal and thermoelectric buoyancy

¹The oscillatory modes reported by Tagg & Weidman [80] for the thermomagnetic Taylor-Couette systems were observed when the radial thermomagnetic force was destabilizing. So, these modes do not have relation with any buoyancy frequency.

forces:

$$\nabla \cdot \mathbf{u} = 0, \quad (5-1a)$$

$$\frac{\partial \mathbf{u}}{\partial t} + \mathbf{u} \cdot \nabla \mathbf{u} = -\nabla \pi + \nabla^2 \mathbf{u} - \gamma_a \theta \mathbf{g}_c \mathbf{e}_r - \frac{L}{\text{Pr}} \theta \mathbf{g}_e \quad (5-1b)$$

$$\frac{\partial \theta}{\partial t} + \mathbf{u} \cdot \nabla \theta = \frac{1}{\text{Pr}} \nabla^2 \theta, \quad (5-1c)$$

$$\nabla \cdot [(1 - \gamma_e \theta) \nabla \phi] = 0, \quad (5-1d)$$

where the equations have been nondimensionalized with the scales $d (= R_2 - R_1)$ of length, $\tau_v = d/\nu^2$ of time, d/τ_v of velocity, $\Delta T (= T_1 - T_2)$ of temperature and Φ_0 of electric potential. The thermal expansion parameter $\gamma_a = \alpha \Delta T$ has been introduced (α : the coefficient of thermal expansion) in addition to the following four dimensionless numbers used in Chap. 3: the radius ratio $\eta = R_1/R_2$, the Prandtl number $\text{Pr} = \nu/\kappa$, the thermoelectric parameter $\gamma_e = e \Delta T$ and the electric Rayleigh number L defined by Eq. (1-24). In outward heating, the three parameters (γ_a, γ_e, L) are all positive, while they take negative values in inward heating.

Following the same argument as that developed in our analysis on the TEHD convection (Sec. 1.3), we assume a high frequency electric tension to adopt the time-averaged description. The boundary conditions on flow fields are then given by

$$\mathbf{u} = \sqrt{\frac{\eta}{1-\eta}} \text{Ta} \mathbf{e}_\varphi, \quad \theta = 1, \quad \phi = 1 \quad \text{at } r = r_1, \quad (5-1e)$$

$$\mathbf{u} = \mathbf{0}, \quad \theta = 0, \quad \phi = 0 \quad \text{at } r = r_2, \quad (5-1f)$$

where the Taylor number Ta has been introduced with the same definition as Eq. (4-4). The radial coordinates r_1 and r_2 indicate the inner and outer cylinder positions: $r_1 = \eta/(1-\eta)$ and $r_2 = 1/(1-\eta)$.

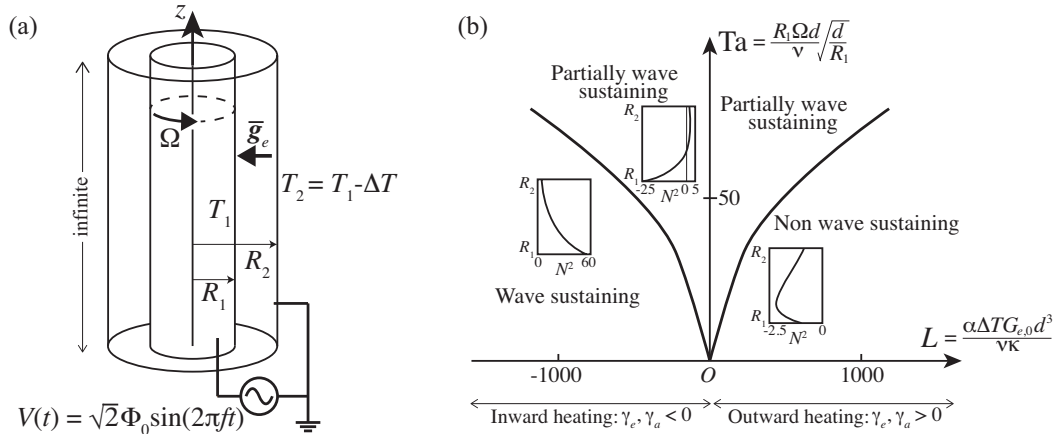


Figure 5-1: Taylor-Couette flow subjected to the radial electric gravity. (a) Schematic illustration of the considered system. (b) Phase diagram of the nature of the density stratification in the L - Ta plane ($\eta = 0.5$, $\gamma_a = \gamma_e = \pm 0.01$). Some profiles of N^2 are shown in insets placed at relevant locations in the plane. In the present chapter, the reference electric gravity $G_{e,0}$ is the electric gravity \mathbf{g}_e in the conductive state at the mid gap: $G_{e,0} = |\mathbf{g}_e(\frac{R_1+R_2}{2})|$.

Conductive state and wave sustainability

We consider a Taylor-Couette system of infinite length. If the imposed temperature and electric field are weak and small, the state of flow will respect the symmetry of the system: it will be axisymmetric, be stationary, have mirror symmetry with respect to any plane perpendicular to the axis and be invariant to translation in the axial direction. The conductive state hence depend only the radial coordinate r . As a consequence, no advection occurs and the velocity decouples from the temperature. The velocity $\bar{\mathbf{u}}$ is the classical circular Couette flow induced by the inner cylinder rotation: $\bar{\mathbf{u}} = \bar{v}(r)\mathbf{e}_\varphi$, with \bar{v} found in Eq. (4-5). The temperature and electric fields are given by Eqs. (1-15)–(1-16). The electric gravity $\bar{\mathbf{g}}_e = -G_e(r)\mathbf{e}_r$, given by Eq. (1-17), depends on (γ_e, η) . Some profiles of the electric gravity are illustrated in Fig. 3-1.

In this conductive state, the stratified fluid layer is subjected to the thermal buoyancy forces due to the centrifugal acceleration $\bar{\mathbf{g}}_c = G_c(r)\mathbf{e}_r$ and to the centripetal electric gravity $\bar{\mathbf{g}}_e = -G_e(r)\mathbf{e}_r$, where $G_c = \bar{v}^2/r$. The buoyancy frequency associated with these forces can be computed by

$$N^2 = \frac{-G_e + G_c}{\rho} \frac{d\rho}{dr}. \quad (5-2)$$

The quantity N^2 is a function of the radial position r . If N^2 is positive around a radial position r , we may expect internal wave propagation in the vicinity of the position r .

According to the sign of the buoyancy frequency, we can distinguish three parameter regions in the L -Ta plane as illustrated in Fig. 5-1(b). The function N^2 is positive throughout the layer in *the wave sustaining region*, while $N^2 < 0$ in *the non wave sustaining region*. Between these two regions, we find *the partially wave sustaining region*, where N^2 is positive only in a sublayer of fluid. This diagram suggests that the heating direction would have prominent effects on the stability and that the instability may be oscillatory either in the wave sustaining region or in the partially wave sustaining region.

5.2 Linear stability theory

The evolution of small perturbation fields can be analyzed by the governing Eq. (5-1) linearized around the conductive state $(\bar{\mathbf{u}}, \bar{\theta}, \bar{\phi})$:

$$\nabla \cdot \mathbf{u}' = 0, \quad (5-3a)$$

$$\frac{\partial \mathbf{u}'}{\partial t} + \bar{\mathbf{u}} \cdot \nabla \mathbf{u}' + \mathbf{u}' \cdot \nabla \bar{\mathbf{u}} = -\nabla \pi' + \nabla^2 \mathbf{u}' - \gamma_a \left(\theta' G_c + \bar{\theta} \frac{2\bar{v}v'}{r} \right) \mathbf{e}_r - \frac{L}{\text{Pr}} \theta' \bar{\mathbf{g}}_e - \frac{L}{\text{Pr}} \bar{\theta} \mathbf{g}'_e \quad (5-3b)$$

$$\frac{\partial \theta'}{\partial t} + \bar{\mathbf{u}} \cdot \nabla \theta' + \mathbf{u}' \cdot \nabla \bar{\theta} = \frac{1}{\text{Pr}} \Delta \theta', \quad (5-3c)$$

$$\nabla \cdot \left[(1 - \gamma_e \bar{\theta}) \nabla \phi' - \gamma_e \theta' \nabla \bar{\phi} \right] = 0, \quad (5-3d)$$

$$\mathbf{u}' = 0, \quad \theta' = \phi' = 0 \quad \text{at } r = r_1, r_2, \quad (5-3e)$$

where $(\mathbf{u}', \theta', \phi')$ are the perturbation velocity, temperature, and electrostatic potential, respectively.

We can determine the stability by considering Eqs. (5-3) for a normal mode $\exp[st + im\varphi + ikz]$, where $s = \sigma - i\omega$ is the complex growth rate (σ : the growth rate; ω : the frequency), m is the azimuthal mode number, and k is the axial wavenumber. For this mode, Eqs. (5-3) forms an eigenvalue problem $\mathbf{A}\mathbf{X} = s\mathbf{B}\mathbf{X}$, where $\mathbf{X} = [\hat{u}' \ \hat{\pi}' \ \hat{\theta}' \ \hat{\phi}']^T$ is the complex amplitude of the normal mode and \mathbf{B} is a constant matrix. The differential matrix operator \mathbf{A} depends on the mode and wave numbers (m, k) and involves the parameters $(L, \text{Ta}, \eta, \gamma_e, \gamma_a, \text{Pr})$. We solve this eigenvalue

problem numerically by invoking a spectral collocation method based on the Chebyshev polynomials. The eigenvalue s with the maximum real part crosses the imaginary axis in the complex plane at a certain value of Ta for given (m, k) and for given parameters (L, η, γ_e, Pr) . Determining this value of Ta with varying the wavenumber k , we obtain the marginal stability curve $Ta = Ta(k)$ for the azimuthal mode m . We then seek the smallest minimum from marginal curves for different azimuthal modes to obtain the critical parameters $(m_c, k_c, Ta_c, \omega_c)$ for a parameter set $(L, \eta, \gamma_e, \gamma_a)$.

The phase diagram in Fig. 5-2 summarizes the basic nature of determined critical modes in the L - Pr plane. The mode is oscillatory axisymmetric (OA), stationary axisymmetric (SA), or oscillatory non axisymmetric (ONA). This diagram is not symmetric with respect to the line $L = 0$. The radial buoyancy forces break the symmetry with respect to the heating direction.

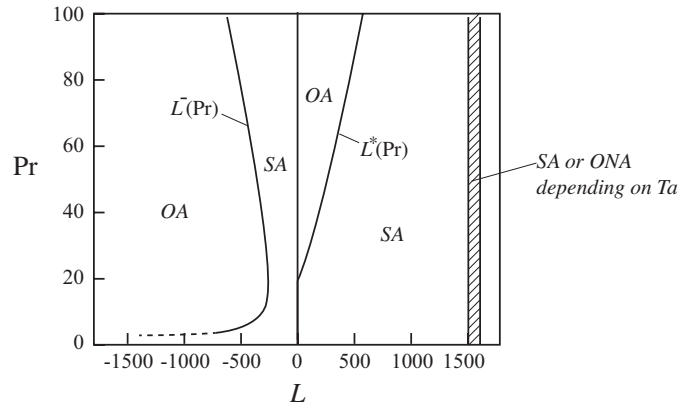


Figure 5-2: Phase diagram of the nature of the critical modes ($\eta = 0.5$, $\gamma_a = \gamma_e = \pm 0.01$): OA : oscillatory axisymmetric; SA : stationary axisymmetric; ONA : oscillatory non axisymmetric.

For a given fluid (i.e., Pr) and a given temperature difference (i.e., γ_e and γ_a), we can explore different instability regimes by varying electric Rayleigh number L . In inward heating the instability is in the OA regime at large negative L . With increasing L , the critical Taylor number decreases slightly (Fig. 5-3a). The total wavenumber q , which is defined by Eq. (4-8) and identical to the axial wavenumber k for axisymmetric modes, is almost constant (Fig. 5-3b). The frequency $|\omega_c|$ decreases toward zero (Fig. 5-3c). At a certain finite negative value $L = L^-$, both OA and SA modes become critical. This coordinate of a codimension-two point varies with Pr , as illustrated by the boundary between the OA and SA regimes found in negative L plane in Fig. 5-2. For negative L larger than L^- , the critical mode is SA . The critical Taylor number decreases rapidly. The critical wavenumber q_c takes slightly larger values than in the OA regime.

In outward heating the instability is in the OA regime at small L if the Prandtl number is larger than a certain value. With increasing L , the critical Taylor number decreases slightly until another codimension-two point $L = L^*$, through which the instability regime changes to SA . In this SA regime, Ta_c decreases significantly. The value of the coordinate L^* also varies with Pr , as illustrated by the boundary between OA and SA in positive L plane in Fig. 5-2. If the Prandtl number is smaller than the lowest point of this boundary, the OA regime does not exist even at small L . Finally, at large positive L , the instability is TEHD and the critical mode is ONA . In this regime, the thermoelectric buoyancy generates spiral convection rolls and these rolls are advected by a slow azimuthal base flow to yield oscillatory behavior of the critical mode.

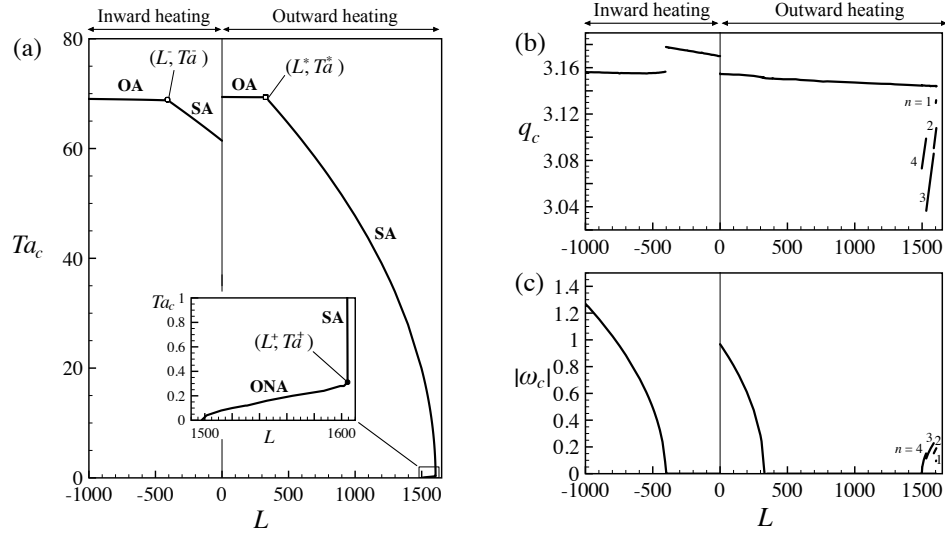


Figure 5-3: Critical parameters for $\eta = 0.5$ and $\text{Pr} = 60$. Thermal expansion and thermoelectric parameters are set at $\gamma_a = \gamma_e = -0.01$ for inward heating and at $\gamma_a = \gamma_e = 0.01$ for outward heating.

Eigenfunctions

In the SA regimes, the velocity field has a fixed phase advance or delay by $\frac{\pi}{2}$ to the temperature fields (Fig. 5-4). Flow goes from the hot to cold cylinders passing through hot temperature cells, as in thermal convection. In the OA regimes, the phase between the velocity and temperature fields varies with L . In the ONA regime, vortices are spiral and distorted in the r - z plane.

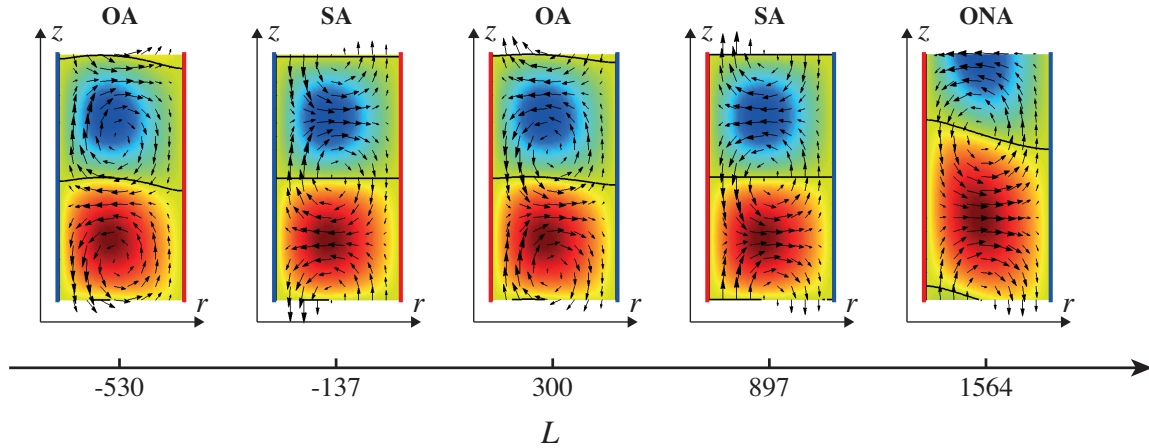


Figure 5-4: Perturbation velocity and temperature fields in the r - z plane in different instability regimes ($\eta = 0.5$, $\text{Pr} = 60$, $\gamma_a = \gamma_e = \pm 0.01$). Solid black curves in each panel are isotherms $\theta' = 0$.

5.3 Analysis

Dispersion relations

The dispersion relation $s = s(k)$ shows qualitative differences between different instability regimes (Fig. 5-5). In SA regimes, a series of dispersion curves $\sigma = \sigma(k)$ are found that are almost parallel to each other (Panel a). In OA regime, the parallel curves are also found in the k - σ plane (Panel b). They are intersected by another curve of larger curvature and the critical mode belongs to the latter curve. Only the normal modes in a limited range of k have frequencies. In ONA regime, the parallel dispersion curves are found again in the k - σ plane (Panel c). All the normal modes have frequencies. As this oscillation behavior is a consequence of the advection of spiral vortices by the slow base flow, the values of the frequencies are almost identical to each other.

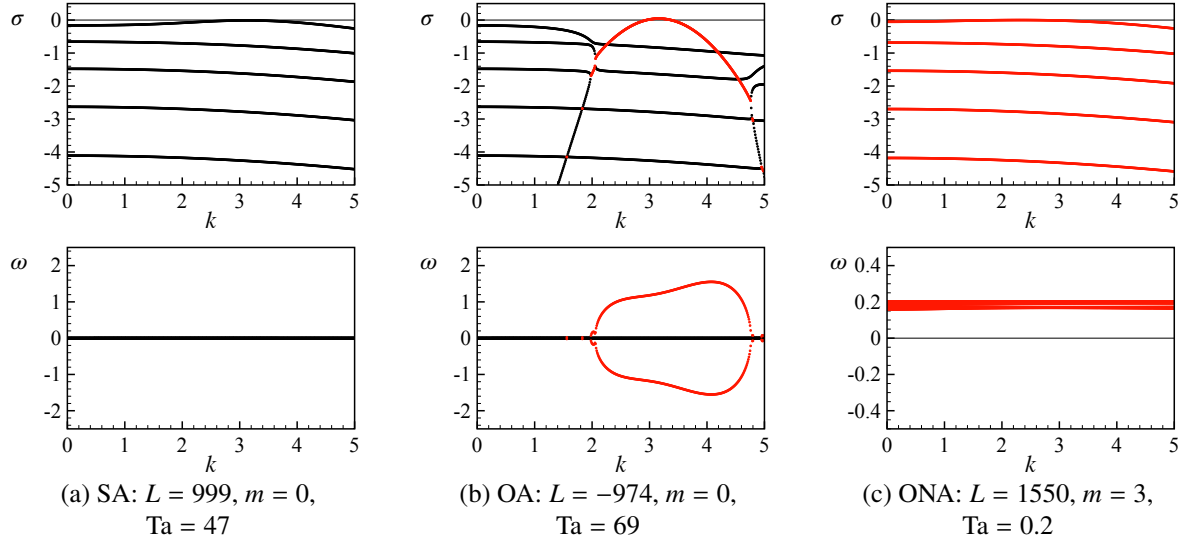


Figure 5-5: Dispersion relations in different instability regimes. The azimuthal model number and the Taylor number are set at critical ones, i.e., $m = m_c$ and $Ta = Ta_c$. ($\eta = 0.5$, $Pr = 60$, $\gamma_e = \pm 0.01$). Black and red dots mean stationary and oscillatory eigenmodes, respectively.

All the observed critical modes have a finite wavelength, i.e., all the instabilities are of type-I. The nonlinear evolution of the perturbation flow can hence be described by the complex Ginzburg-Landau equation:

$$\tau_0 \left(\frac{\partial A}{\partial t} + c_g \frac{\partial A}{\partial z} \right) = \delta (1 + ic_0) A + (1 + ic_1) \xi_0^2 \frac{\partial^2 A}{\partial z^2} - (1 - ic_3) g_0 |A|^2 A, \quad (5-4)$$

where $c_0, c_1, c_3, \tau_0, \xi_0$ and g_0 are real constants. Writing this complex Ginzburg-Landau equation, we have restricted our attention to the OA and SA regimes. The values of the constants involved in Eq. (5-4), except c_3 and g_0 , can be determined from the dispersion curves by invoking Eqs. (2-8) and the following equations:

$$c_g = \left(\frac{\partial \omega}{\partial k} \right)_{cr}, \quad c_0 = -\tau_0 \left(\frac{\partial \omega}{\partial \delta} \right)_{cr}, \quad c_1 = \frac{\tau_0}{2\xi_0^2} \left(\frac{\partial^2 \omega}{\partial k^2} \right)_{cr}. \quad (5-5)$$

Computed values of these coefficients indicate that the nonlinear behavior of the flow will also be distinct in different instability regimes. For example, the coefficients τ_0 and ξ_0 shown in Fig. 5-6 behave very differently in SA and OA regimes. In OA regimes, the coefficients are constant and recover the values of the ordinary Taylor instability, while their values in the SA regimes are sensitive to L .

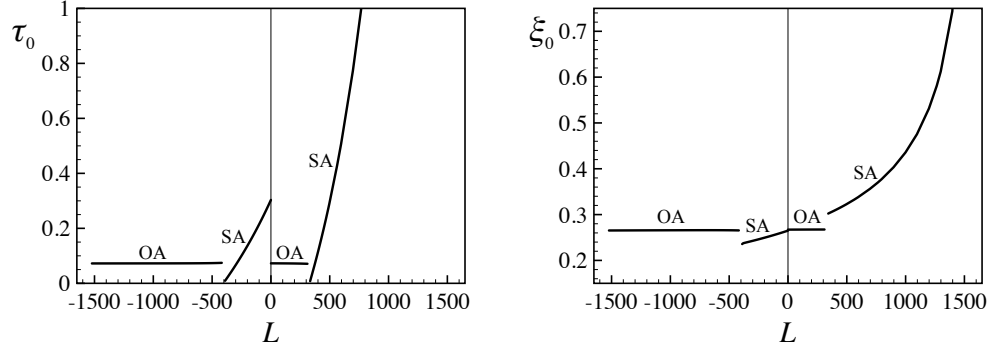


Figure 5-6: Some coefficients of the complex Ginzburg-Landau equation ($\eta = 0.5$, $\gamma_e = \pm 0.01$, $\text{Pr} = 60$)

Energetic analysis

The evolution equation of the kinetic energy of the perturbation flow is derived from the linearized momentum Eq. (5-3b) by taking the inner products with \mathbf{u}' , averaging in space and time and integrating the result over the gap:

$$\frac{dK}{dt} = W_{Ta} + W_C + W_{BG} + W_{PG} - D_v, \quad (5-6)$$

where K is the kinetic energy of the perturbation flow. W_{Ta} is the power by the centrifugal force, W_C is the power by the centrifugal buoyancy force. The contribution of the thermoelectric buoyancy is represented by W_{BG} and W_{PG} : the former by the component associated with the base electric gravity $\bar{\mathbf{g}}_e$ and the latter with the perturbation electric gravity \mathbf{g}'_e . The latter power is much smaller than the former power at small η , as we found in the study of TEHD instability in cylindrical geometry (Sec. 3.2). The term D_v is the viscous energy dissipation rate.

Except the case of large L in outward heating, the centrifugal power (W_{Ta}) is always responsible for the instability (Fig. 5-7). The centrifugal buoyancy and the thermoelectric buoyancy take only small values compared with W_{Ta} except in ONA case, where the thermoelectric buoyancy generates the TEHD convection flow. The radial thermal buoyancy forces, however, change the nature of the instability. In fact, the codimension-two point L^- in inward heating coincident with the moment where the effects of the two buoyancy forces cancel each other: $W_C + W_{BG} = 0$. This is also the case for the codimension-two point L^* in outward heating. The net contribution of the two thermal buoyancy forces is destabilizing, $W_C + W_{BG} < 0$, in both SA regimes. In contrast, in both OA regimes, the net contribution of the two thermal buoyancy forces is negative $W_C + W_{BG} < 0$, i.e., the thermal buoyancy plays a role of a restoring force. This suggests that the oscillatory motion in OA regimes bears a close relation with internal waves propagating due to the restoring force.

Frequency analysis

We found three oscillatory instability regimes. If a strong electric field is applied in outward heating, the instability is in ONA regime. The oscillatory behavior of the critical mode arises from the advection of spiral vortices by the slow base flow. Indeed, the observed azimuthal phase velocity c_φ is proportional to the cylinder rotation, i.e., the Taylor number (Fig. 5-8a).

In the other oscillatory regimes, the net thermal buoyancy has restoring effects. The thermal stratification of the fluid would then be able to sustain wave motion, as discussed earlier. Indeed, the OA regimes are found either in the wave sustaining region or in the partially wave sustaining region in the diagram presented in Fig. 5-1 (b). Furthermore, the buoyancy frequency N , computed by Eq. (5-2), is proportional to the observed critical frequency

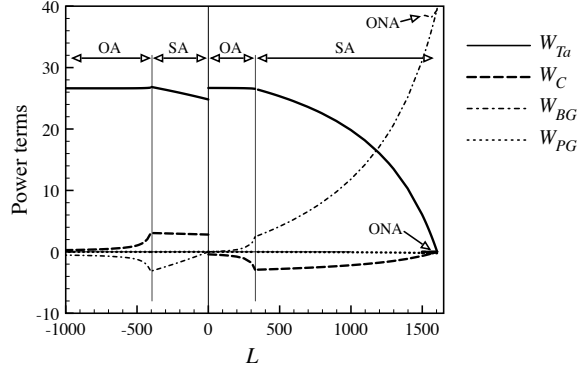


Figure 5-7: Different terms of the kinetic energy equation (5-6). Each term is computed for critical modes and normalized by the twice of the kinetic energy K . ($\eta = 0.5$, $Pr = 60$, $\gamma_a = \gamma_e = \pm 0.01$)

independently from the values of (Pr, γ_a) , if the frequency is higher than the inverse of the viscous time τ_ν (5-8b). This result suggests that the OA mode is internal waves propagating in a stratified fluid layer.

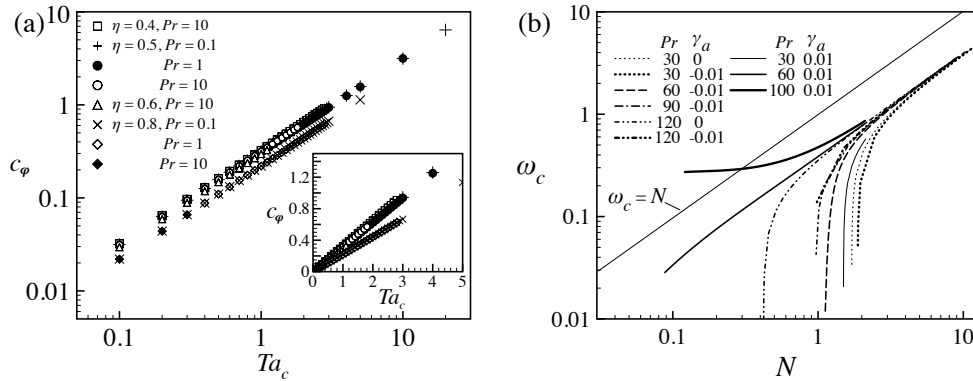


Figure 5-8: Critical frequencies in different oscillatory regimes. (a) ONA regime. (b) OA regimes in outward and inward heating.

5.4 Conclusion

We investigated the stability of a non-isothermal Taylor-Couette flow subjected to a radial buoyancy force due to the electric gravity \mathbf{g}_e by the linear perturbation theory. The theory also took into account another radial thermal buoyancy due to the centrifugal acceleration \mathbf{g}_c . The flow behavior was sensitive to heating direction. Different instability regimes were distinguished. The critical mode can be oscillatory axisymmetric (OA), either at strong thermoelectric buoyancy (i.e., at large $|L|$) in inward heating *or* at weak thermoelectric buoyancy (i.e., at small $|L|$) in outward heating in fluid of large Prandtl number. In this OA regime, the instability is provoked by the centrifugal force as in the Taylor instability. The effects of the two thermal buoyancy forces are, in contrast, stabilizing in total and this net restoring effect produces the oscillation of the mode. The frequency of the critical modes is given by the buoyancy frequency (Eq. 5-2) based on the two buoyancy forces, which characterizes internal waves propagating in a stratified fluid layer.

This result on the relation between the OA critical modes and the internal waves is a generalization of the close

relation between them found in our study on non-isothermal Taylor-Couette flows in Chap. 4. In the latter systems, the centrifugal buoyancy generated OA modes only in outward heating, since only in this heating direction thermal stratification in density was stable in the centrifugal acceleration field \mathbf{g}_c and could sustain waves. In the present thermoelectric Taylor-Couette flows, the stratification can also sustain waves in inward heating when the centripetal electric gravity \mathbf{g}_e is superior to the centrifugal \mathbf{g}_c . We can expect similar wave generation in other non-isothermal Taylor-Couette systems, e.g., the Taylor-Couette flow of ferrofluid subjected to a radial thermomagnetic buoyancy force.

Part III

Flow with bubbles

Chapter 6

Stability of bubbles in oscillatory flow

An experimental investigation on the stability of a centimeter-sized bubble is presented. The bubble is subjected to oscillatory flow in a microgravity environment. This investigation was performed in collaboration with Farzam Zoueshtiagh (IEMN, Lille), Hervé Caps (GRASP, Liège), Pascal Kurowski (PMMH, Paris) and Philippe Petitjeans (PMMH, Paris). The obtained results were communicated at a number of conferences and published in *Microgravity Sci. Technol.* [94] and in *Eur. Phys. J. E* [104]. The latter article is included in appendix C.

6.1 Introduction

Liquid flows with a dispersed gas phase are involved in a wide range of geophysical and industrial processes. Volcanic fluids at a shallow depth often contain ample quantity of gases [38]. Bubble column reactors are widely used in chemical, biochemical, and petrochemical industries [37]. The average size of bubbles is one of the key parameters in modeling these two-phase flows, as the liquid-gas interfacial area affects the local and global transfer of momentum, heat, and mass. Bubbles can breakup and coalesce with others in liquid flow and, as a consequence, their average size can vary in time. The stability of bubbles at a given flow condition is hence of primary importance in two-phase flow modeling.

On the ground the buoyancy in the Earth's gravitational field g is one of the dominant forces in the dynamics of bubbles. The size of stable bubbles is often limited by the capillary length ℓ_{cap} , i.e., the length scale at which the hydrostatic and capillary pressures are in equilibrium: $\ell_{cap} = \sqrt{\sigma/\rho g}$ (σ, ρ : the surface tension and the density of the liquid). This length is of the order of a few millimeters for most liquids. In microgravity conditions there is no corresponding limit¹. It is observed in many situations in microgravity environments that bubbles have a tendency to coalesce and to become larger in an imposed geometry. Liquid-gas interfacial area and, hence, interfacial transports are modest. The bubble size control is therefore an important issue in microgravity science and technologies.

Zoueshtiagh et al. [106] investigated the stability of a bubble in oscillatory liquid flow for bubbles of centimeter size. They performed an experiment on the ground with a setup illustrated in Fig. 6-1. A parallelepiped cell filled by a test liquid with a single air bubble of a given volume V_b ($\sim 2-7$ cm³) was put into oscillatory translational motion of a given frequency f and a given amplitude A . They observed the splitting of large bubbles that reduced efficiently the average bubble size. The size of the split bubbles was scaled by the capillary length ℓ'_{cap} based on the acceleration of the cell: $\ell'_{cap} = \sqrt{\sigma/(\rho A \omega^2)}$, where $\omega = 2\pi f$ is the angular frequency. In other words, bubbles

¹ ℓ_{cap} is of the order of 1 m in a microgravity condition of $1 \mu g = 9.81 \times 10^{-6} \text{ m/s}^2$.

of such a large size D_e that $D_e \gtrsim \ell'_{cap}$ were unstable in oscillatory flow and split into smaller ones, where D_e is the volume equivalent diameter defined by $\pi D_e^3/6 = V_b$.

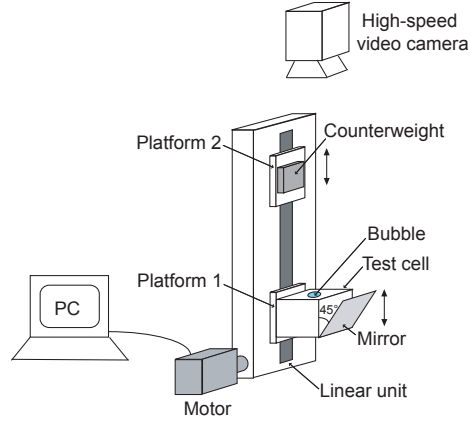


Figure 6-1: Experimental setup

After this preliminary experiment on the ground, we performed experiments in microgravity environments during several parabolic flight campaigns organized by the CNES (Centre National d'Etudes Spatiales). The bubble motion induced by the oscillation and the threshold of bubble splitting were determined in liquids of different viscosities and different surface tensions. We also performed similar experiments on the ground for wider ranges of experimental parameters than in the preliminary experiment. The obtained data in both gravitational environments were analyzed in details in order to reveal the mechanism of splitting. The present chapter is concerned only with the results in microgravity environments. The results in the normal gravity environment can be found in Yoshikawa et al. [104].

Dimensionless numbers

The dynamics of a bubble in oscillatory liquid flow involves different time scales. The viscous time $\tau_v = D_e^2/\nu$ and the advection time $\tau_{adv} = D_e/(A\omega)$ characterize diffusive and advective transports, respectively (ν : the kinematic viscosity of the liquid). The inertial/capillary time $\tau_{cap} = (\rho D_e^3/\sigma)^{1/2}$ is the time scale for a deformed bubble to restore its equilibrium shape. Comparing these time scales with the oscillation time $\tau_{osci} = 2/\omega$, we can find the following three dimensionless numbers:

$$\Omega = \frac{\omega D_e^2}{2\nu}, \quad K_C = \frac{2A}{D_e}, \quad \text{Oh} = \sqrt{\frac{\rho\nu^2}{D_e\sigma}}. \quad (6-1)$$

The first number, Ω , is a dimensionless frequency. The dimensionless amplitude is denoted by K_C , as it is identical to the Keulegan-Carpenter number. The Ohnesorge number Oh depends only on the fluid properties. In our experiments, these numbers take values in the following ranges: $12 < \Omega < 2600$, $0.018 < K_C < 14$, and $8.8 \times 10^{-4} < \text{Oh} < 0.16$.

If the wall effects on liquid and bubble motion are not significant, these three numbers form a complete set of dimensionless numbers to characterize the dynamics of a bubble in oscillatory flow. Indeed, only three dimensionless numbers can be composed from the dimensional parameters ρ , ν , σ , D_e , A and ω . In the following sections, we shall use the parameters (6-1) to present and discuss experimental results.

6.2 Results

Bubble translational motion

When the frequency and amplitude of the oscillatory motion of the parallelepiped cell are both small, the bubble is in oscillatory translational motion without any splitting (Fig. 6-2). During each oscillation period, the bubble deforms from elliptical to spherical cap shapes and vice versa. The translational motion has the same frequency as the cell's motion and a well-defined amplitude (Fig. 6-3a). The motion has a phase advance θ compared with the cell's motion. The phase θ is significantly larger than the value, $\pi/8$, expected for a bubble in creeping liquid flow. The observed shapes and the phase advance indicate that the bubble Reynolds number $Re_b = U_b D_e / \nu$ would be large ($\gtrsim 10^2$) [15], where U_b is the velocity amplitude of the bubble's relative motion to the cell.

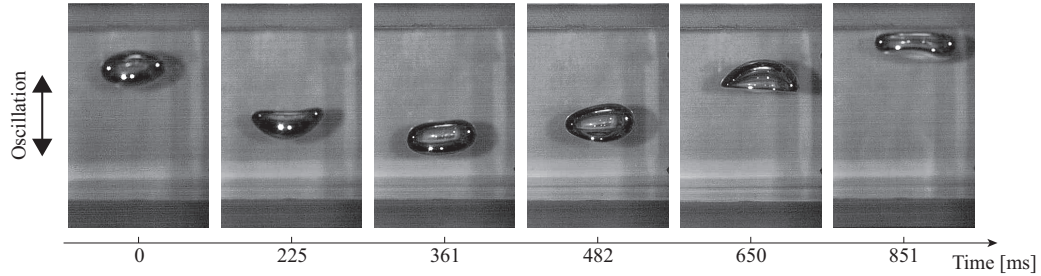


Figure 6-2: Bubble motion in side view (in silicone oil of $\nu = 50 \text{ mm}^2/\text{s}$, $A = 40 \text{ mm}$, $f = 1.0 \text{ Hz}$).

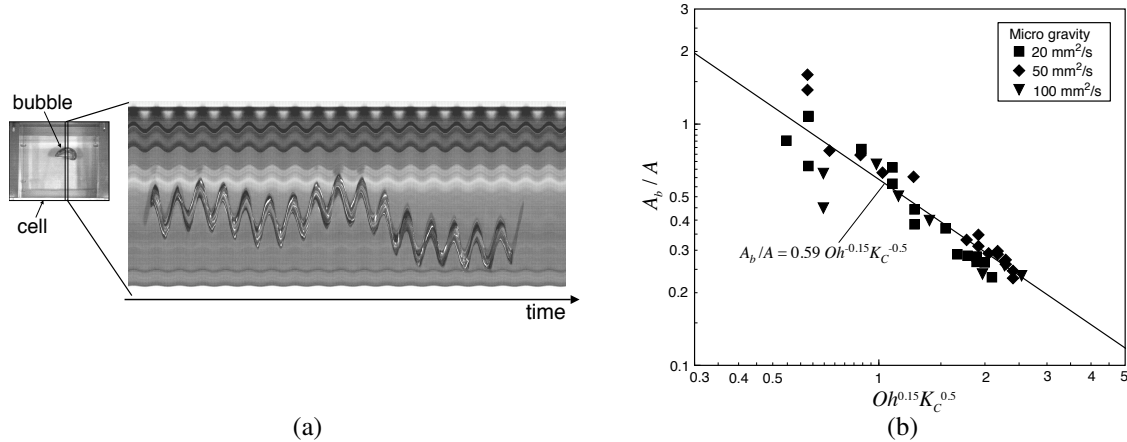


Figure 6-3: Amplitude A_b of bubble motion relative to the cell. (a) Space-time diagram of the bubble translational motion used for amplitude measurements. The diagram is created from a series of images in side view by extracting a narrow band passing the bubble centre at different instants and arranged them chronologically. (b) Results of the measurements for different silicone oils. The amplitude A_b is nondimensionalized by the amplitude A of cell's motion.

The bubble translational motion is a consequence of the cell's acceleration. In the reference frame of the cell, the fluid system is subjected to the oscillatory acceleration field of amplitude $A\omega^2$. The velocity U_b of the bubble relative to the cell is expected to be scaled by the bubble terminal velocity in this acceleration field so that $U_b \sim \sqrt{A\omega^2 D_e}$. The amplitude A_b of the bubble motion relative to the cell is then given by $A_b/A = U_b/(\omega A) \sim \sqrt{D_e/A}$. We hence expect the relation $A_b/A \sim K_C^{-0.5}$. Indeed, the experimental data obtained for different liquids of different

viscosities can be correlated well by the following empirical law (Fig. 6-3b):

$$\frac{A_b}{A} = 0.59 \text{Oh}^{-0.15} K_C^{-0.5}. \quad (6-2)$$

The bubble Reynolds number Re_b can be computed from the empirical relationship (6-2):

$$Re_b = \frac{U_b D_e}{\nu} = 0.588 \text{Oh}^{-0.15} \sqrt{K_C \Omega^2}, \quad (6-3)$$

which gives estimates for Re_b of the order of 100 or larger for the examined ranges of (Ω, K_C, Oh) . This result agrees with our earlier conjecture on Re_b from the bubble shapes and the phase advance.

Splitting

When the cell's oscillatory motion is strong enough, the bubble is pinched at the middle of the body and splits into two pieces of almost identical volume (Fig. 6-4). This splitting occurs during an interval less than 0.1 s. Splitting into several parts is also observed, but it is provoked by stronger oscillatory motion of the cell. The threshold for the splitting is determined by increasing the frequency f successively with a step of 0.1 Hz at a given amplitude A . For a given bubble size and a given liquid, the acceleration of the cell is almost constant at splitting thresholds (Fig. 6-5a). The determined critical acceleration increases with the liquid viscosity and surface tension. Indeed, seeking a power law for splitting thresholds by the least square method, we find the following relationship that correlates well all the threshold data (Fig. 6-5b):

$$K_C \text{Oh}^{1.7} \Omega^{1.93} = 29.3, \quad (6-4)$$

and this empirical law implied the following dependence of the critical acceleration a_c on liquid properties: $a_c \propto \rho^{-0.85} \nu^{0.23} \sigma^{0.85}$.

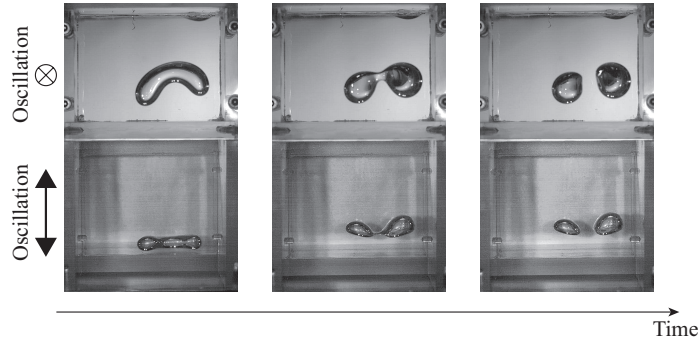


Figure 6-4: Splitting of a bubble. Upper half of each image shows a splitting bubble in axial view. Lower half is the image at the corresponding instant in side view.

6.3 Discussion on the splitting mechanism

The mechanisms of bubble splitting or breakup due to the flow in continuous phase can be classified into three categories [64]. At small Reynolds number, viscous shear at the bubble surface is responsible for the distortion and breakup of bubbles. The threshold of the breakup is given in terms of the capillary number Ca that compares viscous to capillary forces. At large Reynolds number, inertia of the flow is responsible for the breakup. The

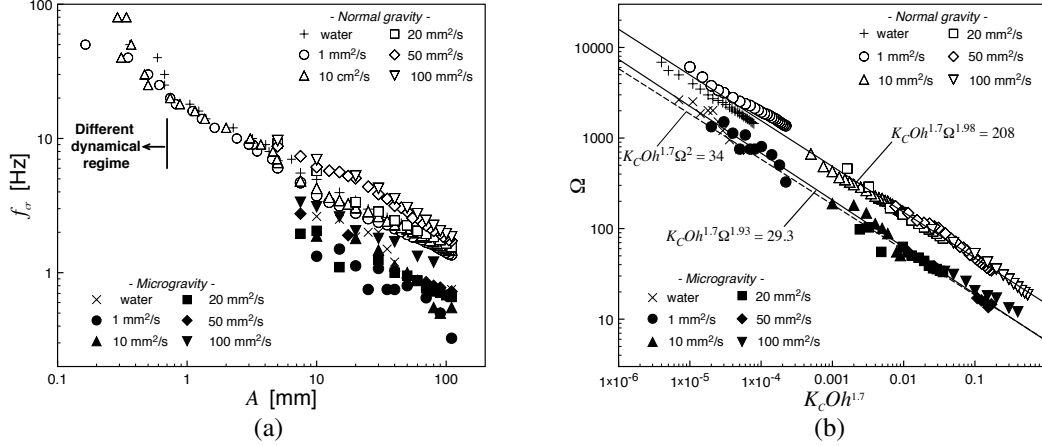


Figure 6-5: Thresholds of bubble splitting: (a) in terms of dimensional oscillation parameters and (b) in terms of dimensionless numbers. Experimental results on the ground are also shown.

breakup criterion is expressed in terms of the Weber number We that represents the relative importance of the inertia to capillarity. For a bubble subjected to unsteady flow, resonance may be responsible for bubble breakup, if the flow has a component at the natural frequencies of bubble's free oscillation.

While these three mechanisms rely on the liquid flow surrounding the bubble, the Rayleigh-Taylor instability can destabilize a bubble in quiescent liquid. It is indeed considered as the mechanism responsible for the instability of bubbles ascending in stagnant liquid and for the instability of bubbles at the rebound stage of cavitation collapse [29, 9].

Among the above-mentioned four types of splitting mechanism, the mechanisms due to viscous shear and to resonance are not plausible. The bubble Reynolds number is high ($\gtrsim 100$) at the splitting threshold observed in our experiments and no preferred frequency is detected in the splitting threshold curves (Fig. 6-5a).

The Rayleigh-Taylor instability might seem to be the most plausible mechanism, since the splitting threshold is characterized by a constant acceleration. According to the theoretical study of Kitscha and Kocamustafaogullari [40], a spherical bubble of diameter D is unstable against the Rayleigh-Taylor instability, when the following inequality holds:

$$\frac{\rho a D^2}{\sigma} > 732.8 \left(1 + \sqrt[4]{\frac{\rho a D^2}{\sigma} Oh} \right)^{1.66}, \quad (6-5)$$

where a is the acceleration to which the bubble is subjected. For the present experiment, this acceleration is calculated by $a = -A\omega^2 \cos \omega t - A_b\omega^2 \cos(\omega t + \theta)$. Since A_b is less than A for most cases (e.g., Fig. 6-3b) and there is a phase advance θ larger than $\pi/8$ in the bubble motion, the maximum acceleration during an oscillation period can be estimated by $(a)_{\max} \approx A\omega^2$ without much error. First splitting would be possible only if the criterion (6-5) is satisfied for this maximum acceleration. Substituting $a = A\omega^2$ and $D = D_e$ into the inequality (6-5), we obtain a necessary condition of the bubble splitting for our experiments: $A\omega^2 > 732.8\sigma/(\rho D_e^2)$. This criterion yields the critical acceleration $a_c = 48.70$ m/s² that is fifty times larger than the observed critical acceleration. Hence, the Rayleigh-Taylor instability mechanism cannot explain the observed splitting.

The splitting due to the inertial mechanism occurs, when the pressure perturbation in continuous phase overcomes the stabilizing capillary pressure. For a spherical drop of diameter D subjected to a steady stream U at high

Reynolds number, the following criterion is used for predicting the drop breakup [32, 84]:

$$\text{We} = \frac{\rho U^2 D}{\sigma} > 12. \quad (6-6)$$

Since this inequality does not depend on the fluid properties of the drop, it would be applicable to the present bubble splitting problem.² First splitting would be expected when the criterion (6-6) holds for the maximum stream velocity $U = U_b = A_b \omega$. Substituting this maximum velocity as well as $D = D_e$ into the criterion (6-6), making use of the correlation (6-2) to estimate the amplitude A_b of bubble motion, and expressing the result in terms of the dimensionless numbers (Ω , K_C , Oh), we obtain the following splitting criterion from Eq. (6-6):

$$K_C \text{Oh}^{1.7} \Omega^2 > 34. \quad (6-7)$$

This prediction is very close to the empirical correlation (6-4). Indeed, comparison with the experimental results shows that the criterion (6-7) agrees excellently with the data, as the correlation (6-4) does (Fig. 6-5b). The inertial mechanism is hence responsible for the observed splitting.

6.4 Conclusion

The stability of a centimeter-sized bubble in oscillatory flow was investigated in microgravity environments. The bubble splitting occurred at a constant acceleration $A\omega^2$ in a given liquid. The analyses of the bubble translational motion and of the bubble splitting thresholds revealed that the inertial criterion $\text{We} > 12$ (i.e., Eq. 6-6) explained the experimental results. This inertial splitting mechanism is independent of the liquid viscosity and it predicts a constant bubble velocity U_b for a bubble of a given size in a given liquid. The liquid viscosity, however, affects the bubble translational motion: in a more viscous liquid, the bubble moves with a smaller oscillation amplitude A_b (Eq. 6-2) and, hence, with a smaller velocity U_b relative to the liquid phase. Consequently, the bubble is more stable in a more viscous liquid, as we observed in experiments (Fig. 6-5a).

Applying the investigated bubble splitting technique to a liquid-gas two-phase system, we can disperse the gas phase in liquid phase with controlling the diameter of gas bubbles. According to the criterion (6-4), one can break bubbles whose diameter is larger than

$$D_e = 1.27 \sqrt{\frac{\sigma^{0.846} \nu^{0.229}}{\rho^{0.846} A^{0.995} f^{1.92}}} \approx 8.0 \ell'_{cap} \left(\frac{\rho^2 \nu^3 f}{\sigma^2} \right)^{0.017}, \quad (6-8)$$

by oscillatory flow, where ℓ'_{cap} is the capillary length based on the acceleration of the cell. This result is similar to that obtained by Zoueshtiagh et al. [106] in their experiments on the ground, but with a correction factor that represents the stabilizing effects of the liquid viscosity.

²The flow unsteadiness would not matter, since the oscillation time τ_{osci} remains large compared with the time scale of splitting (~ 0.1 s) in our experiments.

Chapter 7

Vapor bubble dynamics in microgravity environments

An experimental investigation on the dynamics of a vapor bubble is presented. The bubble nucleates and grows at an artificial nucleation site on a heated wall in a liquid shear flow. Experiments were performed in microgravity conditions. Obtained data were used to compute hydrodynamic and capillary forces in order to assess a theoretical model of the vapor bubble dynamics. This investigation was done in collaboration with Catherine Colin (IMFT, Toulouse) and Cees van der Geld (Eindhoven University of Technology). It was communicated at a number of conferences and published in proceedings of international conferences [46, 95] as well as in *Phys. Fluids* [88].

7.1 Introduction

Nucleate boiling is a heat transfer mode of large capacity. Its application to power consuming devices in orbital systems is waited for managing waste heat in an efficient way. Many studies have been devoted to this mode of heat transfer on the ground, see, e.g., Collier & Thome [17]. However, because of the Archimedean buoyancy that often plays a dominant role in the dynamics of liquid-gas two phase flows on the ground, the results of these studies cannot be extrapolated to the nucleate boiling in other gravitational environments.

Boiling heat transfer involves complex hydrodynamic and thermodynamic processes. Vapor bubbles nucleate at imperfections (e.g., micro cavities, scratches) of a heated surface. They grow at the nucleation sites due to the vaporization of surrounding liquid. Once a bubble attains a certain size, it departs from its nucleation site along the surface or detaches from the surface. This bubble motion disturbs the thermal boundary layer on the heated surface and provokes unsteady heat conduction in the liquid phase. For successful use of nucleate boiling heat transfer in microgravity environments, it is necessary to improve our current understanding on this vapor bubble behavior from a dynamical point of view.

Developing a mechanistic model seems a promising way to predict the complex processes of the nucleate boiling heat transfer [6, 44, 92, 105]. In mechanistic models, the three fundamental processes of heat transfer are identified: liquid vaporization at bubble surface; the unsteady heat conduction during the restitution of the thermal boundary layer on a heated wall that has been disturbed by the passage of a bubble; the steady heat conduction after the restitution of the thermal layer and before the passage of the next bubble. These processes can be parameterized by the bubble size (radius R_b) at its detachment from the wall, the frequency of bubble nucleation and the density of active nucleation sites on the wall surface. Among these parameters, the bubble size R_b is sensitive to the gravitational environment. In mechanistic models, the vapor bubble behavior near the wall is analyzed by a force

balance equation in order to predict R_D , but this approach has never been validated in microgravity conditions.

Intending to develop a reliable model of the vapor bubble dynamics in the vicinity of a heated wall, we perform experiments in microgravity conditions. The growth and motion of a vapor bubble nucleating at an artificial cavity on a heated wall surface is measured by optical observation. Forces exerted on the bubble are estimated from the data obtained about the bubble's geometrical characteristics and motion. These estimates are used to examine whether the balance of the forces can predict the bubble behavior.

The force balance equation to be examined is written [85, 92]:

$$\mathbf{F}_{AM} + \mathbf{F}_D + \mathbf{F}_L + \mathbf{F}_C + \mathbf{F}_P = 0, \quad (7-1)$$

The added-mass force \mathbf{F}_{AM} arises from the inertia of the liquid portion displaced by the bubble. It is associated with bubble's growth and unsteady motion. The hydrodynamic drag \mathbf{F}_D and lift \mathbf{F}_L represent the viscous and inertial effects of the liquid flow. Two forces are exerted by the wall: the capillary force \mathbf{F}_C and the contact pressure force \mathbf{F}_P . The former arises from the capillary attraction at the contact line. The latter is the reaction of the wall to the vapor pressure at the bubble base on the wall.

The forces involved in Eq. (7-1) are not completely known. Their modeling forms an major part of the efforts to develop a force balance model of the bubble dynamics. In our investigation, we follow the work of Montout [55] for this modeling. His force balance model agrees favorably with experimentally determined vapor bubble behavior on the ground. The adopted mathematical expressions of the forces are summarized in Table 7.1 (see also Fig. 7-1a, where the geometrical characteristics of a bubble are illustrated). For the added mass force \mathbf{F}_{AM} , the expression derived by Duhar et al. [24] for a spherical bubble in the vicinity of a solid wall is adopted. The drag coefficient C_D and the lift coefficient C_L in Eqs. (7-2b) and (7-2c) are estimated from the results of a numerical study of Legendre et al. [48]. In Eq. (7-2d) for the capillary force \mathbf{F}_C , $\gamma = \gamma(\varphi)$ is the local contact angle at the azimuthal position φ . Following Thorncroft et al. [85], we assume that the angle γ can be estimated from the upstream and downstream contact angles, α and β , by a polynomial equation $\gamma = \beta + (\alpha - \beta)[3(|\varphi|/\pi)^2 - 2(|\varphi|/\pi)^3]$. To calculate the contact pressure \mathbf{F}_P , the arithmetic mean curvature \mathcal{H} is supposed to be given by the inverse of the bubble radius: $\mathcal{H} = 1/R$.

In the next section, we describe the experimental setup and conditions. Results obtained on the bubble behavior are given and analyzed by computing the forces.

Table 7.1: Forces exerted on a bubble of volume V_b .

| Force | Equation |
|------------------|---|
| Added mass | $\mathbf{F}_{AM} = -\frac{\rho}{2} \frac{d}{dt} \left[\frac{11}{8} V_b v \mathbf{e}_y + \frac{19}{16} V_b (w - W) \mathbf{e}_z \right] + \frac{3}{32} \rho \frac{d^2}{dt^2} (R V_b) \mathbf{e}_y$ (7-2a) |
| Drag | $\mathbf{F}_D = \frac{\rho}{2} C_D \pi R^2 \mathbf{U}' \mathbf{U}'$ (7-2b) |
| Lift | $\mathbf{F}_L = \rho C_L V_b \mathbf{U}' \times \nabla (W \mathbf{e}_z)$ (7-2c) |
| Capillary | $\mathbf{F}_C = -\sigma r_f \int_{-\pi}^{\pi} \sin \gamma d\varphi \mathbf{e}_y - \sigma r_f \int_{-\pi}^{\pi} \cos \varphi \cos \gamma d\varphi \mathbf{e}_z$ (7-2d) |
| Contact pressure | $\mathbf{F}_P = 2\pi r_f^2 \sigma \mathcal{H} \mathbf{e}_y$ (7-2e) |

v, w : the components of the bubble velocity: $v = dy_c/dt, w = dz_c/dt$.

\mathbf{U}' : the relative flow velocity: $\mathbf{U}' = W \mathbf{e}_z - (v \mathbf{e}_y + w \mathbf{e}_z)$.

φ : the azimuthal angle (see Fig. 7-1a).

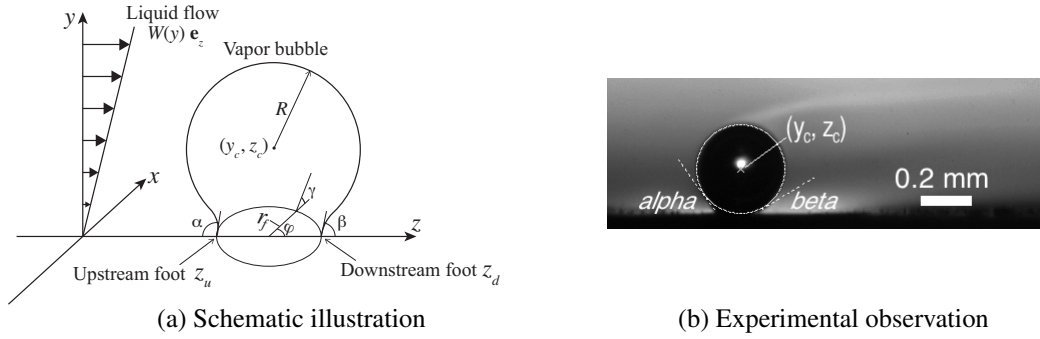


Figure 7-1: A vapor bubble on a heated wall. In (b), the bubble centre and contact angles detected by image analysis are indicated.

7.2 Experiments

Setup & Conditions

A linear duct of rectangular cross section $5 \times 40 \text{ mm}^2$ is used to establish a two-dimensional flow (Fig. 7-2a). The duct has 650 mm in length and a vapor bubble generator (Fig. 7-2b) is flush-mounted on a wider wall at a distance 460 mm downstream from the inlet. The test liquid is HFE-7000 ($\text{C}_3\text{F}_7\text{OCH}_3$) that has a low saturation temperature (Table 7.2). Typical values of the temperature and the pressure of the liquid are $32 \text{ }^\circ\text{C}$ and $1.4 \times 10^5 \text{ Pa}$ corresponding to a subcooling of $10 \text{ }^\circ\text{C}$. The mass flow rate is measured by a Coliolis flow meter which works independently of gravitational environments.

The vapor bubble generator is a thin layer of gold ($\sim 200 \text{ nm}$) sputtered on a glass substrate. A cavity of mouth size around $50 \text{ }\mu\text{m}$ on the layer provides a nucleation site. The electrical resistance of the gold layer is $20 \text{ }\Omega$ at room temperature. It is powered by a constant temperature anemometer for keeping the temperature of the layer constant.

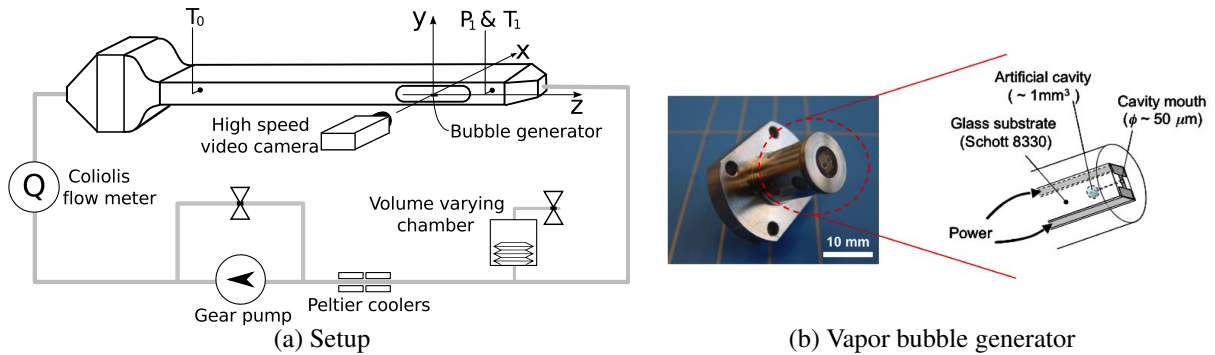


Figure 7-2: Experimental setup and bubble generator

Table 7.2: Properties of HFE-7000 (3MTM, NovecTM7000) at an atmospheric pressure and at $25 \text{ }^\circ\text{C}$.

| | | | | | |
|-----------------|----------|--|-----------------------------|---------------|---------------------------------|
| Density | ρ | 1400 kg/m^3 | Specific heat | c_p | 1300 J/kgK |
| Viscosity | ν | $0.32 \times 10^{-6} \text{ m}^2/\text{s}$ | Latent heat of vaporization | \mathcal{L} | $1.42 \times 10^5 \text{ J/kg}$ |
| Surface tension | σ | $12.4 \times 10^{-3} \text{ N/m}$ | Saturation temperature | T_{sat} | $34 \text{ }^\circ\text{C}$ |

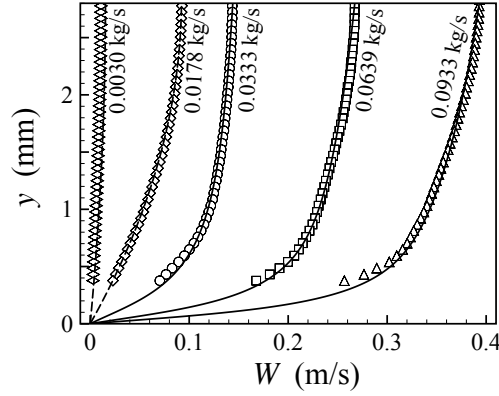


Figure 7-3: Velocity profile at different flow rate

Bubbles growing and moving on the wall are subjected to liquid wall flow. Profiles of the velocity field $W(y)e_z$ measured by the particle image velocimetry at the bubble nucleation site are shown in Fig. 7-3 for different flow rates Q . For small Q (0.0030 and 0.0178 kg/s), the Saint-Venant solution [70] for steady laminar flow is also shown in broken line. Turbulent flow profiles of Reichardt type [63] are plotted with solid line for larger Q (0.0333, 0.0639 and 0.0933 kg/s):

$$W = w^* \left[\frac{1}{\kappa} \log(1 + \kappa y^+) + c \left(1 - e^{-y^+/\chi} - \frac{y^+}{\chi} e^{-0.33y^+} \right) \right] \quad (7-3)$$

with $y^+ = w^*y/\nu$, where w^* is the friction velocity. The von Karman constant κ is given by $\kappa = 0.41$. The other constants are set at $\chi = 11$ and $c = 8.67$. As seen in the figure, the laminar and turbulent velocity profiles predict well the velocity fields at low and high flow rates, respectively. The laminar-turbulent transition that is found between $Q = 0.0178$ and 0.0333 kg/s corresponds to a reasonable value of the Reynolds number Re (≈ 3000). The bubble behavior reported in the next section was obtained at $Q = 0.0333$ kg/s. The calculation of different forces will be based on the velocity profile (7-3). The friction velocity w^* for this flow rate is 0.00568 m/s.

Experiments were performed in a microgravity environment realized by parabolic flights of the aircraft Airbus A300 ZERO-G during the 50th ESA Parabolic Flight Campaign in May 2009. At each parabola, the microgravity state lasted 22 s with a typical quality of $10^{-2}g$ (g : the gravitational acceleration). The temperature in the cabin is kept at 20 °C by air conditioning.

Results

Growth and motion of bubbles at the bubble generator are observed by a high-speed camera whose optical axis is perpendicular to the flow plane (i.e., the y - z plane). A typical rate of image acquisition is 500 images per second. The resolution of images is 508 pixels/mm. Recoded images are processed to determine the radius R and centre of the bubble (y_c, z_c) as well as the positions of bubble feet, z_u, z_d , and the contact angles, α, β (Fig. 7-1a). A typical result of the processing is shown in Fig. 7-1(b), where determined best fitting circle and contact angles are superposed on an experimental image.

A bubble at the nucleation site of the bubble generator grows as shown in Fig. 7-4 where the time evolution of the bubble radius R is plotted. A fitting curve for R indicates a time dependency $R \propto t^{1/3}$, which is slower than the growth in the diffusion-controlled regime ($\propto t^{1/2}$) [10]. This might be a result of the condensation of vapor at the bubble top where a luminous plume indicating a high liquid temperature is observed (Fig. 7-1b). At the same instant as the departure from the nucleation site, the bubble detaches from the wall. This detachment occurs within

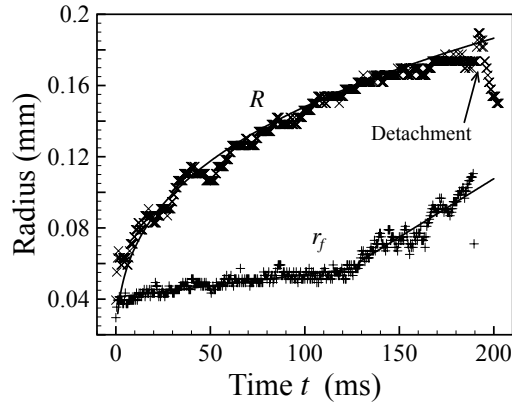


Figure 7-4: Evolution of the bubble radius R and the radius r_f of the bubble-wall contact area (see Fig. 7-1a for the definition of r_f).

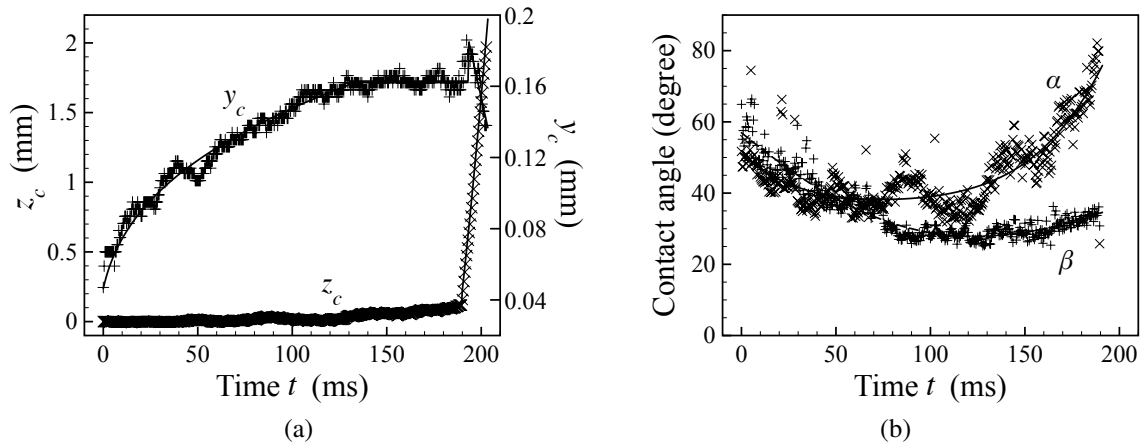


Figure 7-5: Bubble motion: (a) the evolution of the bubble center and (b) evolution of the upstream and downstream contact angles.

a very short time interval (~ 1 ms). After the detachment, the bubble radius R decreases due to recondensation of vapor in subcooled surrounding liquid. In Fig. 7-4, the radius r_f of the bubble-wall contact circle: $r_f = (z_d - z_u)/2$, is also shown. It increases at a small rate at the beginning ($t < 130$ ms) and at a larger rate at the end until the detachment ($130 < t < 190$ ms).

Figure 7-5(a) shows the displacement of the bubble center (y_c, z_c). At the nucleation site, the bubble is pulled downstream by the flow only a little. Indeed, the position z_c along the wall does not vary much until the departure. After the detachment, the bubble is advected by the liquid flow. The coordinate y_c increases due to the bubble growth. Its variation merges with the evolution of the bubble radius R .

Figure 7-5(b) shows the time evolution of the contact angles (α, β), with tendency curves shown in solid and broken lines. At the beginning ($t < 80$ ms), hydrodynamic effects of the liquid flow are small compared with capillary effects because of the small size of the bubble. Consequently, the bubble has a symmetrical shape with respect to its normal axis to the wall. The upstream contact angle α and the downstream contact angle β are hence almost equal to each other. The symmetric bubble shape is observed until the bubble size becomes $R \sim 0.15$ mm (Fig. 7-4). Once the bubble becomes larger, the forces exerted by the flow breaks the symmetry: the upstream contact angle α

increases, while the downstream one β remains constant ($t > 130$ ms). The lost of symmetrical shape is coincident with the change of the rate of increase found in the behavior of the contact area radius r_f (Fig. 7-4).

Analysis

Forces calculated by Eqs. (7-2) are shown in Fig. 7-6. All the time derivatives needed for the calculations have been computed by using the tendency curves shown in Figs. 7-4 & 7-5 in solid lines. In the normal direction to the wall (i.e., in the y direction), the dominant forces are the capillary force F_C and the contact pressure force F_P (Fig. 7-6a). They are directed opposite to each other and, qualitatively, they balance each other out. Even at the departure ($t = 190$ ms), no indication of the violation of the force balance is seen. In the stream direction (i.e., in the z direction), the drag and capillary forces are dominant compared with the other forces (Fig. 7-6b). The former, which tends to remove the bubble from the nucleation site, increases linearly in time until the bubble detachment. Qualitatively, this force is equilibrated by the capillary force until $t \sim 130$ ms, except at the beginning of bubble growth ($t \lesssim 70$ ms), where contact angle measurements would include large errors due to small bubble sizes. After $t \sim 130$ ms, the upstream contact angle α increases rapidly (Fig. 7-5b) and, as a consequence, the capillary force decreases rapidly. The balance between capillary and drag forces cannot be expected. Even though the observed departure occurred at $t = 190$ ms, this indication to the break of the force balance would be regarded as a sign of the bubble departure.

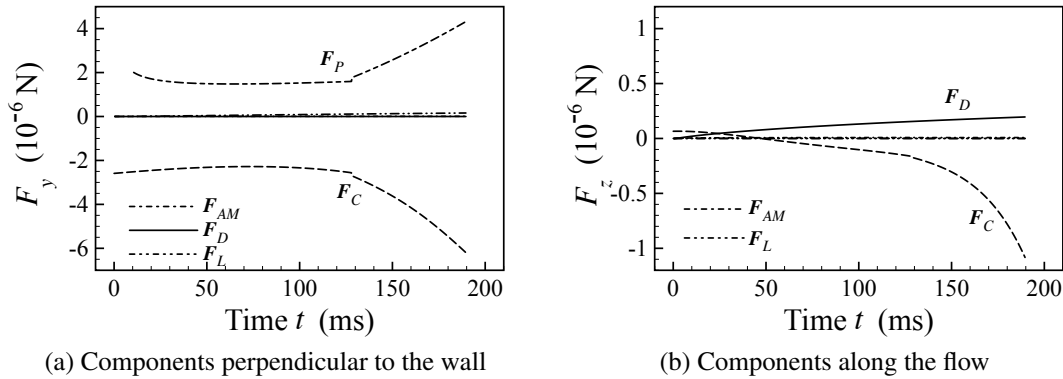


Figure 7-6: Different forces before the departure from the nucleation site.

7.3 Conclusions

Dynamics of a isolated vapor bubble was investigated experimentally in microgravity environments. Optical observation of the bubble behavior was performed to calculate different forces exerted on the bubble attached on the wall at the nucleation site. Calculated forces confirmed the balance of these forces and suggested that the bubble departure could be associated with the break of this force balance. Modeling the vapor bubble dynamics by the force balance is hence a promising way for prediction vapor bubble behavior. It is however necessary to refine substantially the models of forces, as the quantitative agreement is not satisfactory.

Chapter 8

Formation of spiral patterns in a simple liquid-gas system

An experimental investigation on the formation of regular patterns in a simple liquid-gas two-phase flow system is reported. A theoretical model developed for getting insights into the pattern formation mechanism is also presented. This investigation was motivated by the analogy of observed patterns with the formation of botanical patterns, *the phyllotaxis*. This research was performed in collaboration with Dr. Christian Mathis, Dr. Philippe Maïssa and Dr. Germain Rousseaux of Laboratoire J.-A. Dieudonné as well as with Dr. Stéphane Douady (MSC, Paris). The results were published in *Eur. Phys. J. E* [99] and in a proceedings book of a conference [98].

8.1 Introduction

Liquid-gas two-phase flows are observed in many natural and industrial processes. Experimental, theoretical, and numerical investigations on their dynamics have been performed in a variety of flow configurations. Due to the complex interaction between liquid and gas phases, much effort still must be made to understand these two-phase flows. Even a simple flow system, in which bubbles are formed by continuous gas supply through a tube or an orifice, exhibits rich dynamical behavior [16, 60]. In the present chapter, we report an experiment on a pattern formation in a very simple system illustrated in Fig. 8-1(a), where gas bubbles of volume V_b are injected one by one with a period T into a liquid of density ρ and kinematic viscosity ν contained in a cylindrical tank. We are interested in the patterns exhibited by these bubbles after their emergence from the liquid free surface. The main motivation for investigation comes from the analogy between these patterns and patterns in plants.

The arrangement of leaves on plant stems, called *phyllotaxis*, has interested scholars for a long time [13, 69] because of its astonishing regularity. Leaves often exhibit a spiral pattern that results from a constant angular shift, called *the divergence angle*, around the stem between two consecutive leaves. Phyllotaxis is known for its mathematical richness: it has a close relation with the golden mean $\tau = (\sqrt{5} + 1)/2$ and the Fibonacci series. Microscopic observation of shoot apices, where leaf primordia are born, and surgical experiments on them suggest that the compaction of the primordia during the meristematic development plays a crucial role in phyllotaxis [69]. Recently, considering systems other than plants, Levitov [50] and Douady & Couder [22, 23] showed that repulsive objects¹ under a geometric constraint can exhibit phyllotaxis-like patterns characterized by a constant angular shift ψ between two consecutive objects. Increasing the compaction of the objects, they found that the angular

¹Abrikosov vortices in a superconductor in [50]; ferrofluid drops in a magnetic field in [22, 23]

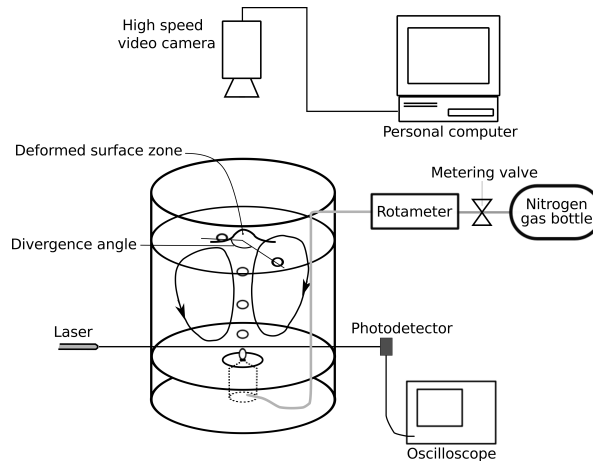


Figure 8-1: Schematic illustration of the investigated flow system with measurement devices.

shift ψ experienced a series of quasi-bifurcations and converged to the Fibonacci angle $\psi_F = 360^\circ/\tau^2 = 137.5^\circ$, which is the most frequently observed angle in natural plants. These results suggest that the phyllotactic pattern formation would be observed in a wide class of non-botanical systems.

8.2 Experiments

The experimental setup is illustrated in Fig. 8-1(a). Nitrogen gas is injected into silicone oil through an orifice placed at the center of the bottom of a vertical cylindrical tank. The orifice has a diameter ranging from 0.8 to 3.0 mm. Bubbles of a constant volume V_b form at and detach from the orifice with a constant period T . The volume-equivalent diameter D_e of the bubbles is about 6 mm. After being released from the orifice, bubbles rise along the system's symmetry axis in a regular chain (Fig. 8-2a1) and emerge from the free surface with a period identical to the bubble injection period T . This bubble motion induces a liquid jet along the bubble rising path, which impinges the free surface to make a bump (*apex*). The jet is then converted into a diverging radial flow along the surface (Fig. 8-2b). Bubbles emerging from the free surface are advected radially by this surface flow.

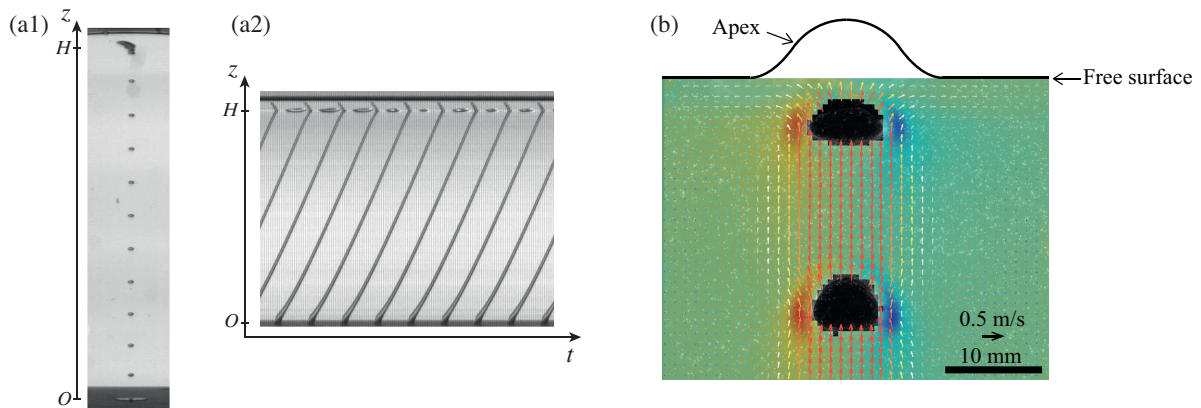


Figure 8-2: Rising motion of bubbles and induced velocity field. (a1) Rising bubbles in side view. $z = H$ indicates the level of the free surface. (a2) A space-time diagram constructed from a series of successive images in side view. Oblique gray stripes signify the motion of bubbles. (b) A velocity field in the vicinity of the free surface. Background colors show vorticity.

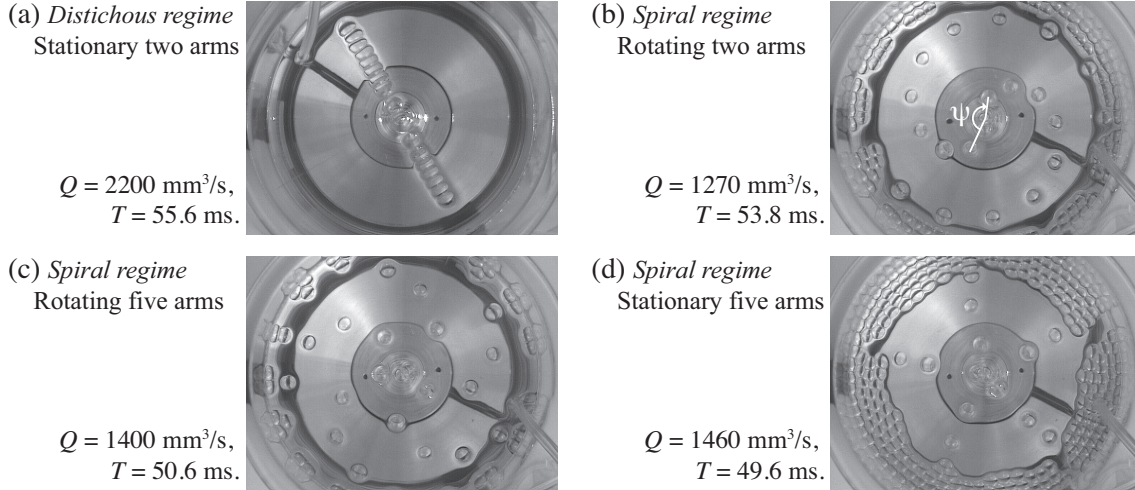


Figure 8-3: Patterns of bubbles formed on the free surface of a silicone oil of 0.033 Pa s at different gas flow rates Q . The measured value of the bubble formation period T is shown at the side of each image. The definition of the divergence angle ψ is illustrated in (b).

At a small flow rate Q of nitrogen gas, emerged bubbles are clustered at the central zone of the surface due to the capillary attraction between floating bubbles. With increasing Q , the frequency of bubble injection, $1/T$, increases and the induced liquid jet and surface flow become strong. The resulting strong advection of bubbles by the surface flow makes each emerged bubble move individually in a radial direction at the surface. The angle of divergence, ψ , i.e., the angular shift between the radial directions of two consecutive bubbles, is constant and equal to 180 degrees. In this *distichous regime*, a straight arrangement of bubbles is observed on the surface (Fig. 8-3a). Further increase of Q leads to another regime, *spiral regime*, where ψ is a constant smaller than 180 degrees: a spiral arrangement is formed at the surface (Fig. 8-3b-d). The transition between these two regimes occurs through a supercritical bifurcation. The divergence angle ψ decreases with Q . If the flow rate exceeds a certain value, bubbles emerge from the free surface with a period two times larger than the bubble injection period T . This is a consequence of an instability in bubble chains [68], which leads to bubbles' pairing and period doubling behavior. This third regime is out of scope of the present investigation.

Figure 8-4 summarizes our experimental observations, where the following three dimensionless numbers are used for presentation: the Bond number Bo , the Ohnesorge number Oh and the dimensionless frequency Ω of bubble injection. These numbers are defined by

$$Bo = \frac{\rho g D_e^2}{\sigma}, \quad Oh = \sqrt{\frac{\rho \nu^2}{\sigma D_e}}, \quad \Omega = \frac{D_e^2}{\nu T}, \quad (8-1)$$

where σ is the surface tension of the liquid. Figure 8-4(a) shows behavior of the divergence angle ψ for different silicone oils of different viscosities. Figure 8-4(b) illustrate the parameter zones corresponding to the distichous, spiral and period doubling regimes. In the spiral regime, the values of the divergence angle are indicated by iso-value curves.

The transition from distichous to spiral regimes is closely related to the interaction between emerging bubbles in the apex. Indeed, the bubble motion observed in side view (Fig. 8-2a) gave no indication to the transition, while the behavior of bubbles in the apex changes qualitatively at the transition. Optical observation of the latter behavior

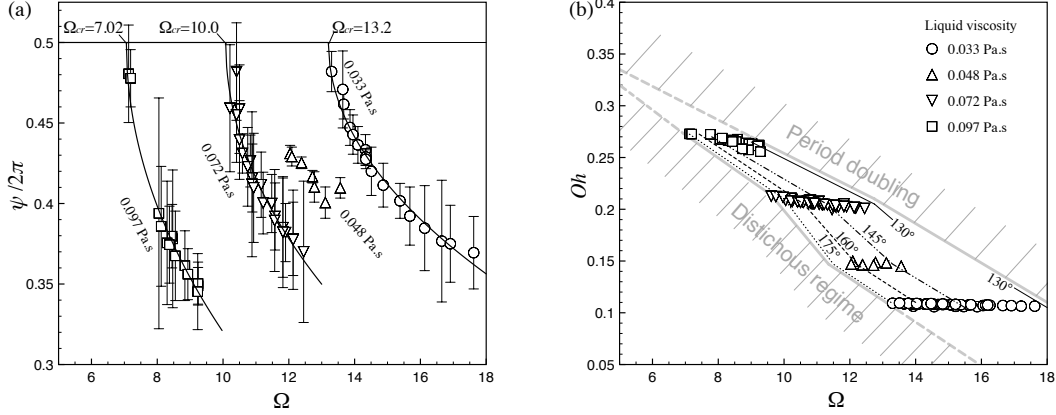


Figure 8-4: Divergence angle ψ observed in the spiral regime. (a) Variation of ψ with the dimensionless frequency Ω for different liquids. (b) Phase diagram. The divergence angle ψ is shown by iso-value curves in the spiral regime.

shows that the number N of the bubbles with which each bubble interacts during the emergence increases at the distichous-spiral transition. In the distichous regime, superposition of two bubbles is observed just before a bubble emerges from the free surface. It follows that each bubble interacts with its preceding and succeeding ones during the emergence so that $N = 2$. In contrast, superposition of three bubbles occurs in the spiral regime (Fig. 8-5), implying $N = 4$. This finding suggests that the transition is a consequence of the increase of compaction in the apex, where emerging bubbles are subjected to geometric constraint. The mechanism of the formation of observed patterns would hence be similar to that of phyllotaxis.

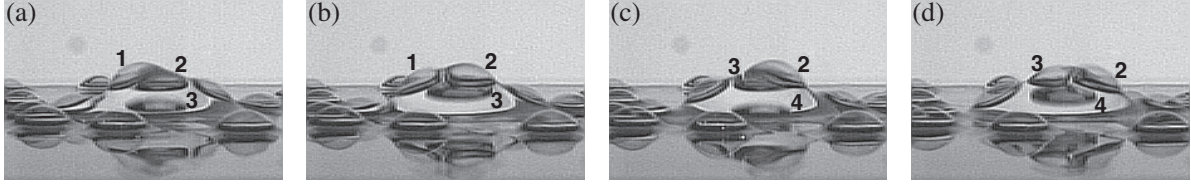


Figure 8-5: Successive images showing bubble behavior at their emergence from the free surface in the spiral regime. Images were taken by a horizontal camera with its optical axis tilted slightly downward. The bubbles are numbered chronologically. The liquid is a silicone oil of 0.033 Pa s.

8.3 Theoretical model

We develop a theoretical model in order to substantiate the idea that the interaction of bubbles in the apex gives rise to different observed patterns. The model is based on the equation of motion for each bubble:

$$0 = 2\pi\rho\nu D_e \left(\mathbf{U} - \frac{d\mathbf{r}_j}{dt} \right) + \sum_i \mathbf{f}_{ji} + \rho \frac{\pi}{6} D_e^3 g \mathbf{e}_z + \mathbf{S} \quad (j = 1, 2, \dots), \quad (8-2)$$

where \mathbf{r}_j is the position of the j 'th bubble's centre. The first term in the right-hand-side is the Stokes drag that represents the advection of the bubble by the liquid flow. The liquid flow velocity field \mathbf{U} is assumed of the form $\mathbf{U}(r, \varphi, z) = a(r\mathbf{e}_r - 2z\mathbf{e}_z)$ that mimics measured velocity fields in the vicinity of the free surface (a : an adjustable constant of the order of 20 s^{-1}). The second term represents the interactions with other bubbles: \mathbf{f}_{ji} is the force exerted by the i 'th bubble. This bubble interaction can be significant only when the inter-bubble distance becomes

small, i.e., only when bubbles are found in the apex. As we observed strong distortion of bubbles in the apex, we assume repulsive interaction arising from the capillarity: $\mathbf{f}_{ji} = K(\mathbf{r}_j - \mathbf{r}_i)$ with the coefficient $K = b\sigma$ (b : an adjustable constant of the order of unity). This force is effective only for two neighboring bubbles of inter-bubble distance smaller than a bubble diameter: $|\mathbf{r}_j - \mathbf{r}_i| < D_e$. The third term is the Archimedean buoyancy force. A correction to the latter force after the bubble emerges from the surface and the interaction with the free surface are taken into account in the fourth term \mathbf{S} , which is a vertical force pushing the bubble downwards at the surface.

Nondimensionalizing Eq. (8-2) with a time scale T and a length scale D_e , we get the following coupled ordinary equation set:

$$\frac{d\mathbf{r}_j}{dt} = A\mathbf{U} + F \sum_{j \neq i} (\mathbf{r}_j - \mathbf{r}_i) H(1 - |\mathbf{r}_j - \mathbf{r}_i|) + S(\mathbf{r}_i, \text{Bo}, \Omega) \mathbf{e}_z \quad (j = 1, 2, \dots), \quad (8-3)$$

where H stands for the Heaviside step function. The dimensionless parameters A and F represent the advection by the flow and the bubble-bubble interaction, respectively:

$$A = T \left(\frac{\partial U_r}{\partial r} \right)_{(r,z)=0}, \quad F = \frac{KT}{2\pi\rho\nu D_e}. \quad (8-4)$$

where U_r is the radial flow velocity and the point $(r, z) = 0$ indicates the center of the free surface. The advection parameter A is of the order of the unity for our experiments.

Numerical simulation of the model is carried out by integrating the ordinary differential equation set (8-3) with the initial condition that bubbles are injected at $z = z_0$ (< 0) without any velocity with a constant period. For the integration of each equation, the fourth-order Runge-Kutta method was adopted. Results of the simulation show that, as speculated, any bubble interacts with others only when it is emerging from the surface at a small central zone ($r \lesssim 1$). After leaving this zone, the bubble moves in a radial direction without any more interaction with other bubbles. We can then determine the radial direction of the surface motion of a bubble and can compute its angular deviation from the direction of the preceding bubble. Figure 8-6(a) shows the behavior of this divergence angle ψ_j between the j 'th and $(j+1)$ 'th bubbles ($j = 1, 2, \dots$) for a given value of A . After 50 bubbles, the divergence angle converges to a constant value ψ . The final value ψ of the divergence angle is 160 degrees: a spiral arrangement will be observed on the free surface. In the figure, the number N_j of the bubbles with which the bubble j interacts is also plotted. While N_j takes odd values (3 and then 5) at the beginning, it converges to the final value $N = 4$, the expected value in the spiral regime.

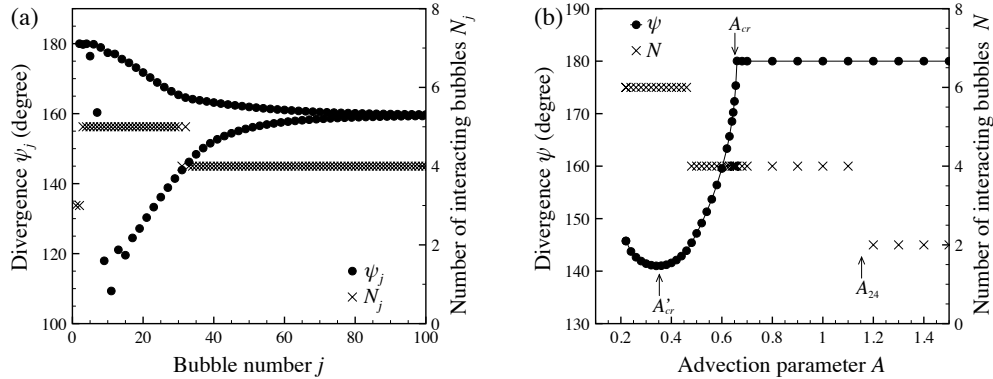


Figure 8-6: Divergence angles obtained in simulations of the theoretical model (Eq. 8-3). (a) Angle ψ_j between two consecutive bubbles at $A = 0.6$. (b) Final constant value ψ . The bubble interaction number N_j and its final value N are also shown in these graphs. ($F = 0.3$ and $\text{Bo} = 17$ for both panels).

The final value of the divergence, ψ , depends on the advection parameter A and the interaction parameter F . Varying these parameters, the model can reproduce the bifurcation from the distichous to spiral regimes observed in the experiment. Figure 8-6(b) shows the behavior of ψ when the advection parameter A is varied. For large A , the angle ψ is 180° so that the system is in the distichous regime. Below a critical value $A_{cr} = 0.66$, the divergence ψ decreases with decreasing A . This behavior is similar to that observed in the experiment (Fig. 8-4a), where ψ decreases with increasing dimensionless frequency Ω which is inversely proportional to the advection parameter A . Further decrease of A leads to another transition at $A'_{cr} = 0.34$, where ψ starts increasing. This corresponds to the first quasi-bifurcation observed in the theoretical studies on phyllotactic pattern formations [50, 22]. In Fig. 8-6(b), the number N of interacting bubbles is also plotted. For large A , the number N is equal to 2. With decreasing A , the number N jumps to 4: the bubble j interacts with the bubbles $j - 2$, $j - 1$, $j + 1$ and $j + 2$. This jump occurs at $A = A_{24}$ which is larger than A_{cr} . For A in the range $A_{24} < A < A_{cr}$, the interactions with the bubbles $j \pm 2$ are not strong enough and, consequently, the system would remain in the distichous mode. Similar delay of regime transition is also found for the transition at A'_{cr} : with decreasing A , the number N jumps to 6 slightly before $A = A'_{cr}$. In our experiment, the transition at $A = A'_{cr}$ was not observed, since instability of ascending bubble chain [68], which is not taken into account in the model, occurred before.

The behavior of ψ and N predicted by the simulation is consistent with the experimental observations, as described above. It supports the conjecture that the increasing compaction of bubbles in the apex provokes the distichous-spiral transition and gives rise to the decrease of ψ in the spiral regime.

8.4 Conclusion

We investigated the formation of patterns exhibited by periodically emerging bubbles from a liquid free surface. Experimental observation of bubble behavior shows that the bubble-bubble interaction in a bump of the surface (apex) plays a decisive role in the pattern formation. This indicates the analogy with the meristematic development in a shoot apex of a plant that leads to a regular leaf arrangement, *phyllotaxis*. A simple theoretical model was developed for our experiment. The model is based on the balance of the forces on each bubble and takes into account the advection by the liquid flow and the bubble-bubble interaction, both of which affect the compaction of bubbles in the apex. The model can reproduce the experimentally observed behavior of the divergence angle ψ , in particular, the transition from the distichous regime to the spiral regime. The predicted behavior of the number N of interacting bubbles in the apex is consistent with experimental observations. The compaction of bubbles in the apex is hence the origin of observed spiral patterns. The mechanism of the pattern formation is a phyllotactic one.

Perspectives

Research project for coming years

For coming years, my research activities will be concentrated on non-isothermal electrohydrodynamic (EHD) flows driven by the thermal DEP force in cylindrical annular and spherical shell geometries. Non-linear flow states and related heat transfer will be investigated by theoretical analyses as well as by direct numerical simulations. This is a continuation of my preceding works (Chaps. 2, 3, & 5) in the sense that the gravito-EHD analogy motivates the research. However, the focus of investigations is the propagation of waves due to the thermoelectric buoyancy in a stratified fluid layer. My investigations aim to establish a theoretical basis for these EHD internal waves.

Fluids in electric fields can sustain wave motion due to forces exerted by the field. EHD surface waves on a liquid film and on a liquid jet have been investigated by many researchers (e.g., [14, 53] among others), as they pertain to many applications (control of coating process, heat transfer enhancement at a liquid surface, atomization of a liquid jet, etc.). The behavior of free charge carriers at an isotype heterogeneous junction of a semiconductor was modeled by an electrohydrodynamic approach and wave propagation was predicted [8]. The waves were characterized by a Brunt-Väisälä frequency associated with the stratification of the junction. Electrohydrodynamic effects on the gravity waves that generate the traveling ionospheric disturbances in the Earth's upper atmosphere have also been discussed [39]. All these waves are, however, related to the Coulomb forces on free charges suspended in the fluid. There are few studies on waves sustained by the dielectric force.

According to the gravito-EHD analogy, however, it is expected that internal waves propagate in a thermally stratified fluid layer in an electric field due to the thermal DEP force. Indeed, a dispersion relation similar to the relation of the classical internal waves was obtained for a fluid layer in a cylindrical capacitor in the limit of vanishing viscosity.¹ The maximum value of the frequency of these EHD internal waves is given by the buoyancy frequency N based on the centripetal electric gravity G_e : $N = \sqrt{-(G_e/\rho)d\rho/dr}$. Furthermore, in my preceding research on a non-isothermal Taylor-Couette system with a radial electric field (Chap. 5), we found the oscillatory eigenmodes that are characterized by this buoyancy frequency N . Investigations on the EHD internal waves will be of great interest in geo- and astro-physics, since laboratory experiments on these waves can enable us to simulate large-scale wave motions in atmosphere and ocean up to highly nonlinear flow regimes.

Theoretical and numerical investigations are needed for guiding experiments on the EHD internal waves and understanding their results. In particular, we should know, by theories and DNS, under which conditions the analogy works precisely. In fact, the gravito-EHD analogy is broken by thermoelectric feedback effects, which is represented by the perturbation component of the electric gravity \mathbf{g}'_e (Chaps. 2&3).

To establish the theoretical basis of experiments on the EHD internal waves, I plan to perform the following tasks for flows, mainly in cylindrical annular geometry:

1. Determination of non-linear states of oscillatory modes found in a Taylor-Couette system (Chap. 5),
2. Characterization of the EHD internal waves in the linear regime with/without cylinder rotation,
3. Characterization of the EHD internal waves in the non-linear regimes with/without cylinder rotation, by theoretical modeling and by direct numerical simulations.

For Task 1, the exact traveling wave solutions of the governing equations (5-1) are determined. For this determination, we will follow the path of the bifurcation from the conductive state, whose stability is considered in Chap. 5.

¹My result communicated at APS DFD conference in 2014.

The governing equation will be solved in Fourier-Chebyshev spectral space by the Newton-Raphson method. For Task 2, dispersion relations will be determined by solving linearized governing equations with exploring different ranges of flow parameters. For Task 3, the wave equations that model the non-linear wave behavior will be sought. They may take the forms of the Korteweg-de Vries equation or of the non-linear Schrödinger equation, depending on geometrical constraints and flow parameters. DNS aims to validate these model equations as well as to examine the parameter ranges at which the models lost their validity. Simulations will be performed by developing existing spectral codes and/or finite volume codes. Throughout these investigations, the contribution of the thermoelectric feedback to wave dynamics will be distinguished in order to clarify the validity of the gravito-EHD analogy. In non-linear regimes, momentum and heat transfer associated with the waves will be determined for future comparisons with experiments.

In Task 3, particular focus will be placed on the propagation of solitary waves in annular geometry. This type of nonlinear wave, which can travel a long distance with keeping their shape due to the balance between the non-linearity and dispersion of the waves, is observed in a variety of physical systems [59]. Propagation of solitary waves is also observed in geophysics. These waves play an important role in the large-scale transport phenomena and in the energy exchange between flows of different scales. They have been studied for waves in the atmosphere, e.g., for gravity waves and for Rossby waves [30, 62]. Solitary waves are also subject of intense research in oceanography. Many observations of solitary waves by satellites have been reported [4]. The gravito-EHD analogy can offer laboratory experiments to simulate this important class of geophysical waves.

The research will be carried out in collaboration with other researchers. The determination of non-linear exact solutions will be performed in collaboration with Prof. M. Nagata (Tianjin University). Direct numerical simulation would benefit from a future collaboration with experts in computational fluid dynamics of EHD flows. I will also keep the actual close relation with a research team of the Laboratoire Ondes et Milieux Complexes in Le Havre (Prof. I. Mutabazi, Dr. O. Crumeyrolle), which plans to perform experiments in annular geometry.

Bibliography

- [1] M. Ali and P. D. Weidman. On the stability of circular Couette flow with radial heating. *J. Fluid Mech.*, 220:53–84, 1990.
- [2] A. Alonso, M. Net, and E. Knobloch. On the transition to columnar convection. *Phys. Fluids*, 7(5):935–940, 1995.
- [3] A. Alonso, M. Net, I. Mercader, and E. Knobloch. Onset of convection in a rotating annulus with a radial gravity and heating. *Fluid Dyn. Res.*, 24:133–145, 2008.
- [4] J. R. Apel, L. A. Ostrovsky, Y. A. Stepanyants, and J. F. Lynch. Internal solitons in the ocean and their effect on underwater sound. *J. Acoust. Soc. Am.*, 121(2):695–722, 2007.
- [5] K. S. Ball, B. Farouk, and V.C. Dixit. An experimental study of heat transfer in a vertical annulus with a rotating inner cylinder. *Int. J. Heat Mass Transfer*, 32(8):1517–1527, 1989.
- [6] N. Basu, G. R. Warriar, and V. K. Dhir. Wall heat flux partitioning during subcooled flow boiling: Part 1—model development. *J. Heat Transfer*, 127(2):131, 2005.
- [7] A. Bozhko and G. Putin. Thermomagnetic convection as a tool for heat and mass transfer control in nanosize materials under microgravity conditions. *Microgravity Sci. Technol.*, 21:89–93, 2009.
- [8] R. A. Brazhe and R. M. Meftahutdinov. Waveguide propagation of internal electrohydrodynamic waves in heterojunctions. *Radiophysics and Quantum Electronics*, 43(5):407–410, 2000.
- [9] Christopher E. Brennen. *Fundamentals of Multiphase Flow*. Cambridge University Press, New York, April 2005.
- [10] V. P. Carey. *Liquid-Vapor Phase-Change Phenomena*. Taylor & Francis, 2nd edition, 2008.
- [11] Bo Chandra and D. E. Smylie. A laboratory model of thermal convection under a central force field. *Geophysical Fluid Dynamics*, 3:211–224, 1972.
- [12] S. Chandrasekhar. *Hydrodynamic and hydromagnetic stability*. Dover, New York, 1961.
- [13] H. Church. *On the relation of phyllotaxis to mechanical laws*. Williams & Norgate, 14 Henrietta street, Covent Garden, London, 1904.
- [14] R. Cimpeanu and D. T. Papageorgiou. On the generation of nonlinear travelling waves in confined geometries using electric fields. *Proc. R. Soc. Lond. A*, 372(2020), 2014.
- [15] R. Clift, J. R. Grace, and M. E. Weber. *Bubbles, Drops, and Particles*. Academic Press, New York, 1978.

- [16] Eduardo Colli, Viviane S. M. Piassi, Alberto Tufaile, and José Carlos Sartorelli. Bistability in bubble formation. *Phys. Rev. E*, 70:066215, 2004.
- [17] J. G. Collier and J. R. Thome. *Convective boiling and condensation*. Oxford University Press, 1996.
- [18] M. Cross and H. Greenside. *Pattern formation and dynamics in nonequilibrium systems*. Cambridge University Press, New York, 2009.
- [19] M. C. Cross. Derivation of the amplitude equation at the Rayleigh-Bénard instability. *Phys. Fluids*, 23:1727–1731, 1980.
- [20] M. C. Cross and P. C. Hohenberg. Pattern formation outside of equilibrium. *Rev. Mod. Phys.*, 65(3):851–1112, July 1993.
- [21] N. Dahley, B. Futterer, C. Egbers, O. Crumeyrolle, and I. Mutabazi. Parabolic flight experiment “convection in a cylinder – Convection patterns in varying buoyancy forces. *J. Physics: Conference Series*, 318:082003, 2011.
- [22] S. Douady and Y. Couder. Phyllotaxis as a physical self-organized growth process. *Phys. Rev. Lett.*, 68(13):2098–2101, March 1992.
- [23] S. Douady and Y. Couder. Phyllotaxis as a self organizing process. part 1. *J. Theor. Biol.*, 178(255), 1996.
- [24] G. Duhar, G. Riboux, and C. Colin. Vapour bubble growth and detachment at the wall of shear flow. *Heat Mass Transfer*, 45(7):847–855, 2009.
- [25] P. M. Eagles and V. M. Soundalgekar. Stability of flow between two rotating cylinders in the presence of a constant heat flux at the outer cylinder and radial temperature gradient — wide gap problem. *Heat Mass Transfer*, 33(3):257–260, 1997.
- [26] D. G. Economides and G. Moir. Taylor vortices and the Goldreich-Schubert instability. *Geophys. Astrophys. Fluid Dynamics*, 16:299–317, 1981.
- [27] M. Tadie Fogaing, H. N. Yoshikawa, O. Crumeyrolle, and I. Mutabazi. Heat transfer in the thermo-electrohydrodynamic convection under microgravity conditions. *Eur. Phys. J. E*, page under consideration, 2013.
- [28] B. Futterer, A. Krebs, A.-C. Plesa, F. Zaussinger, R. Hollerbach, D. Breuer, and C. Egbers. Sheet-like and plume-like thermal flow in a spherical convection experiment performed under microgravity. *J. Fluid Mech.*, 735:647–683, 2013.
- [29] J. R. Grace, T. Wairegi, and J. Brophy. Break-up of drops and bubbles in stagnant media. *Can. J. Chem. Eng.*, 56:3–8, 1978.
- [30] R. Grimshaw, editor. *Environmental stratified flows*. Kluwer Academic Publishers, Boston, MA, 2002.
- [31] J. E. Hart, G. A. Glatzmaier, and J. Toomre. Space-laboratory and numerical simulations of thermal convection in a rotating hemispherical shell with radial gravity. *J. Fluid Mech.*, 173:519–544, 1986.
- [32] L.-P. Hsiang and G. M. Faeth. Drop deformation and breakup due to shock wave and steady disturbances. *Int. J. Multiphase Flow*, 21(4):545–560, 1995.
- [33] J. D. Jackson. *Classical Electrodynamics*. Wiley, 3rd edition, 1999.

- [34] T. B. Jones. Electrohydrodynamically enhanced heat transfer in liquids – A review. *Advances in Heat Transfer*, 14:107–148, 1979.
- [35] T. B. Jones. *Electromechanics of Particles*. Cambridge University Press, 2005.
- [36] L. Kahouadji, H. Yoshikawa, J. Peixinho, and I. Mutabazi. Heat transfer by Görtler vortices developed on a wall with finite conductivity. *Proc. of Rencontre du Non-Linéaire*, 2014.
- [37] N. Kantarci, F. Borak, and K. O. Ulgen. Bubble column reactors. *Process Biochem.*, 40:2263–2283, 2005.
- [38] H. Kawakatsu and M. Yamamoto. *Treatise on Geophysics – Earthquake Seismology*, volume 4, chapter Volcano Seismology, pages 389–420. Elsevier, 2007.
- [39] M. C. Kelley and C. A. Miller. Electrodynamics of midlatitude spread f 3. Electrohydrodynamic waves ? A new look at the role of electric fields in thermospheric wave dynamics. *J. Geophys. Res.*, 102(A6):11539–11547, 1997.
- [40] J. Kitscha and G. Kocamustafaogullari. Breakup criteria for fluid particles. *Int. J. Multiphase Flow*, 15(4):573–588, 1989.
- [41] C.-H. Kong and I-C. Liu. The stability of nonaxisymmetric circular Couette flow with a radial temperature gradient. *Phys. Fluids*, 6:2617, 1994.
- [42] N. Kosseifi, P. H. Biwole, C. Mathis, G. Rousseaux, S. A. E. Boyer, H. N. Yoshikawa, and T. Coupez. Application of two-color LIF thermometry to nucleate boiling. *J. Materials Science and Engineering A*, 3(5):281–290, 2013.
- [43] F. Kreith. Convection heat transfer in rotating systems. *Advances in Heat Transfer*, 5:129–251, 1968.
- [44] N. Kurul and M. Podowski. Multidimensional effects in force convection subcooled boiling. In *Proceedings of the 9th Heat Transfer Conference*, pages 21–26, 1990.
- [45] L. D. Landau and E. M. Lifshitz. *Electrodynamics of Continuous Media*, volume 8 of *Landau and Lifshitz Course of Theoretical Physics*. Butterworth–Heinemann, 2nd edition, 1984.
- [46] M. Lebon, H. N. Yoshikawa, J. Sebilleau, and C. Colin. Bubble formation in a quiescent liquid and in a shear flow. In *ICMF 2015 Proceedings*, Boulder, CO, April 2015.
- [47] Y. N. Lee and W. J. Minkowycz. Heat transfer characteristics of the annulus of two coaxial cylinders with one rotating. *Int. J. Heat Mass Transfer*, 32(4):711–722, 1989.
- [48] D. Legendre, J. Magnaudet, and G. Mougin. Hydrodynamic interactions between two spherical bubbles rising side by side in a viscous liquid. *J. Fluid Mech.*, 497:133–166, 2003.
- [49] V. Lepiller, A. Goharzadeh, A. Prigent, and I. Mutabazi. Weak temperature gradient effect on the stability of the circular Couette flow. *Eur. Phys. J. B*, 61:445–455, 2008.
- [50] L. S. Levitov. Phyllotaxis of flux lattices in layered superconductors. *Phys. Rev. Lett.*, 66:224–227, 1991.
- [51] J. M. Lopez, F. Marques, and M. Avila. The Boussinesq approximation in rapidly rotating flows. *J. Fluid Mech.*, 737:56–77, 2013.
- [52] S. V. Malik, H. N. Yoshikawa, O. Crumeyrolle, and I. Mutabazi. Thermo–electro–hydrodynamic instabilities in a dielectric liquid under microgravity. *Acta Astronaut.*, 81:563–569, 2012.

- [53] J. R. Melcher. Electrohydrodynamic and magnetohydrodynamic surface waves and instabilities. *Phys. Fluids*, 4:1348–1354, 1961.
- [54] J. R. Melcher. *Continuum Electromechanics*. The MIT Press, 1981.
- [55] M. Montout. *Contribution au développement d'une approche prédictive de la crise d'ébullition*. PhD thesis, Université de Toulouse, France, 2008.
- [56] D. R. Ohlsen and P. B. Rhines. Laboratory studies of equatorially trapped waves using ferrofluid. *J. Fluid Mech.*, 338:35–58, 1997.
- [57] J. S. Paschkewitz and D. M. Pratt. The influence of fluid properties on electrohydrodynamic heat transfer enhancement in liquids under viscous and electrically dominated flow conditions. *Exp. Therm. Fluid Sci.*, 21(4):187–197, 2000.
- [58] R. Pethig. Review article – Dielectrophoresis: Status of the theory, technology, and applications. *Biomeicrofluidics*, 4:022811, 2010.
- [59] M. Peyrard and T. Dauxois. *Physique des solitons*. EDP Sciences, Paris, cnrs editions edition, 2004.
- [60] Viviane S. M. Piassi, Alberto Tufaile, and José Carlos Sartorelli. Period-adding bifurcations and chaos in a bubble column. *Chaos*, 14(2):477–486, 2004.
- [61] H. A. Pohl. *Dielectrophoresis: The behavior of neutral matter in nonuniform electric fields*. Cambridge University Press, 1978.
- [62] L. G. Redekopp. On the theory of solitary Rossby waves. *J. Fluid Mech.*, 82(4):725–745, 1977.
- [63] H. Reichardt. Vollständige darstellung der turbulenten geschwindigkeitsverteilung in glatten leitungen. *Z. Angew. Math. Mech.*, 31(7):208–219, 1951.
- [64] F. Risso. The mechanisms of deformation and breakup of drops and bubbles. *Multiphase Science and technology*, 12:1–50, 2000.
- [65] P. H. Roberts. Electrohydrodynamic convection. *Q. J. Mech. Appl. Math.*, 22:211–220, 1969.
- [66] R. E. Rosensweig, J. Browaeys, J.-C. Bacri, A. Zebib, and R. Perzynski. Laboratory study of spherical convection in simulated central gravity. *Phys. Rev. Lett.*, 83(23):4904–4907, 1999.
- [67] G. Rousseaux, H. Yoshikawa, A. Stegner, and J. E. Wesfreid. Dynamics of transient eddy above rolling-grain ripples. *Phys. Fluids*, 16(4):1049–1058, April 2004.
- [68] M. C. Ruzicka. Vertical stability of bubble chain: multiscale approach. *Int. J. Multiphase Flow*, 31:1063–1096, 2005.
- [69] T. Sachs. *Pattern formation in plant tissues*. Cambridge University Press, 1991. Chap. 11.
- [70] B. Saint-Venant. Mémoire sur la torsion des prismes. *Mémoires de l'Académie des Sciences des Savants Etrangers*, 14:233–560, 1855.
- [71] A. Schlüter, D. Lortz, and F. Busse. On the stability of steady finite amplitude convection. *J. Fluid Mech.*, 23:129–144, 1965.
- [72] G. Schubert and D. Bercovici, editors. *Treatise on Geophysics – Mantle dynamics*. Elsevier, 2009.

- [73] B. Sitte and H. J. Rath. Influence of the dielectrophoretic force on thermal convection. *Exp. Fluids*, 34:24–27, 2003.
- [74] B. L. Smorodin and M. G. Velarde. On the parametric excitation of electrothermal instability in a dielectric liquid layer using an alternating electric field. *J. Electrostatics*, pages 205–226, 2001.
- [75] H. A. Snyder and S. K. F. Karlsson. Experiments on the stability of Couette motion with a radial thermal gradient. *Phys. Fluids*, 7(10):1696–1706, 1964.
- [76] M. M. Sorour and J. E. R. Coney. The effect of temperature gradient on the stability of flow between vertical, concentric, rotating cylinders. *J. Mech. Engng Sci.*, 21(6):403–409, 1979.
- [77] P. J. Stiles. Electro-thermal convection in dielectric liquids. *Chem. Phys. Lett.*, 179(3):311–315, 1991.
- [78] P. J. Stiles and M. Kagan. Stability of cylindrical Couette flow of a radially polarised dielectric liquid in a radial temperature gradient. *Physica A*, 197:583–592, 1993.
- [79] P. J. Stiles, F. Lin, and P. J. Blennerhassett. Convective heat transfer through polarized dielectric liquids. *Phys. Fluids A*, 5(12):3273–3279, 1993.
- [80] R. Tagg and P. D. Weidman. Linear stability of radially-heated circular Couette flow with simulated radial gravity. *Z. Angew. Math. Phys.*, 58:431–456, 2007.
- [81] M. Takashima. Electrohydrodynamic instability in a dielectric fluid between two coaxial cylinders. *Q. J. Mech. Appl. Math.*, 33(1):93–103, 1980.
- [82] M. Takashima and H. Hamabata. The stability of natural convection in a vertical layer of dielectric fluid in the presence of a horizontal ac electric field. *J. Phys. Soc. Jpn*, 53(5):1728–1736, May 1984.
- [83] H. S. Takhar, V. M. Soundalgekar, and M. A. Ali. Effects of radial temperature gradient on the stability of a narrow-gap annulus flow. *J. Math. Anal. Appl.*, 152:156–175, 1990.
- [84] G. I. Taylor. The shape and acceleration of a drop in a high-speed air stream. Technical Report AC 10647/Phys. C69, Advisory Council on Scientific Research and Technical Development, Ministry of Supply, 1949.
- [85] G. E. Thorncroft, J. F. Klausner, and R. Mei. Bubble forces and detachment models. *Multiphase Science and technology*, 13(3 & 4):35–76, 2001.
- [86] V. Travnikov, O. Crumeyrolle, and I. Mutabazi. Numerical investigation of the heat transfer in cylindrical annulus with a dielectric fluid under microgravity. *Phys. Fluids*, 27:054103, 2015.
- [87] R. J. Turnbull. Effect of dielectrophoretic forces on the Bénard instability. *Phys. Fluids*, 12(9):1809–1815, 1969.
- [88] C. W. M. van der Geld, C. Colin, Q. I. E. Segers, V. H. Pereira da Rosa, and H. N. Yoshikawa. Forces on a boiling bubble in a developing boundary layer, in microgravity with g-jitter and in terrestrial conditions. *Phys. Fluids*, 24:082104, 2012.
- [89] J. Walowit, S. Tsao, and R. C. DiPrima. Stability of flow between arbitrarily spaced concentric cylindrical surfaces including the effect of a radial temperature gradient. *ASME J. Appl. Mech.*, 31(4):585–593, 1964.

- [90] T. Yamamoto and H. R. Velkoff. Electrohydrodynamics in an electrostatic precipitator. *J. Fluid Mech.*, 108:1–18, 1981.
- [91] I. M. Yavorskaya, N. I. Fomina, and Yu. N. Belyaev. A simulation of central-symmetry convection in microgravity conditions. *Acta Astronautica*, 11(3–4):179–183, 1984.
- [92] G. H. Yeoh, Sherman C. P. Cheung, J. Y. Tu, and K. M. Ho Mark. Fundamental consideration of wall heat partition of vertical subcooled boiling flows. *Int. J. Heat Mass Transfer*, 2008.
- [93] C-S. Yih. Dual role of viscosity in the instability of revolving fluids of variable density. *Phys. Fluids*, 4(7):806–810, 1961.
- [94] H. Yoshikawa, P. Kurowski, P. Petitjeans, F. Zoueshtiagh, and H. Caps. Bubble rupture in a vibrated liquid under microgravity. *Microgravity Sci. Technol.*, 19(3-4):155–156, October 2007.
- [95] H. N. Yoshikawa and C. Colin. Single vapor bubble behavior in a shear flow in microgravity. In *ICMF 2010 Proceedings*, Tampa, FL, May–June 2010.
- [96] H. N. Yoshikawa, O. Crumeyrolle, and I. Mutabazi. Dielectrophoretic force-driven thermal convection in annular geometry. *Phys. Fluids*, 25:024106, 2013.
- [97] H. N. Yoshikawa, M. Tadie Fogaing, O. Crumeyrolle, and I. Mutabazi. Dielectric Rayleigh-Bénard convection under microgravity conditions. *Phys. Rev. E*, 87:043003, 2013.
- [98] H. N. Yoshikawa, C. Mathis, P. Maïssa, and G. Rousseaux. *Spiral pattern formation in a simple two-phase flow system*, pages 113–122. World Scientific, Singapore, 2012.
- [99] H. N. Yoshikawa, C. Mathis, P. Maïssa, G. Rousseaux, and S. Douady. Pattern formation in bubbles emerging periodically from a liquid free surface. *Eur. Phys. J. E*, 2010.
- [100] H. N. Yoshikawa, A. Meyer, O. Crumeyrolle, and I. Mutabazi. Linear stability of a circular couette flow under a radial thermoelectric body force. *Phys. Rev. E*, 91(3):033003, 2015.
- [101] H. N. Yoshikawa, M. Nagata, and I. Mutabazi. Instability of the vertical annular flow with a radial heating and rotating inner cylinder. *Phys. Fluids*, 25:114104, 2013.
- [102] H. N. Yoshikawa and J. E. Wesfreid. Oscillatory Kelvin-Helmholtz instability. Part 1. A viscous theory. *J. Fluid Mech.*, 675:223–248, 2011.
- [103] H. N. Yoshikawa and J. E. Wesfreid. Oscillatory Kelvin-Helmholtz instability. Part 2. An experiment in fluids with a large viscosity contrast. *J. Fluid Mech.*, 675:249–267, 2011.
- [104] H. N. Yoshikawa, F. Zoueshtiagh, H. Caps, P. Kurowski, and P. Petitjeans. Bubble splitting in oscillatory flows on ground and in reduced gravity. *Eur. Phys. J. E*, 31:191–199, 2010.
- [105] L. Z. Zeng, J. F. Klausner, D. M. Bernhard, and R. Mei. A unified model for the prediction of bubble detachment diameters in boiling systems. II. Flow boiling. *Int. J. Heat Mass Transfer*, 36:2271–2279, 1993.
- [106] F. Zoueshtiagh, H. Caps, M. Legendre, N. Vandewalle, P. Petitjeans, and P. Kurowski. Air bubbles under vertical vibrations. *Eur. Phys. J. E*, 20:317–325, 2006.

Appendixes

Appendix A

Curriculum vitæ

Harunori NAKAGAWA-YOSHIKAWA

Date of birth 5 January 1974
Nationality Japanese
Office Laboratoire J.-A. Dieudonné
UMR 7351 CNRS – Université Nice Sophia-Antipolis
Parc Valrose - 06108 Nice Cedex 02, France
Phone +33 (0)4 9207 6486 **Fax** +33 (0)4 9351 7974
e-mail harunori@unice.fr
web <http://math.unice.fr/~harunori>

Research field

Experimental and theoretical fluid dynamics (Instabilities, Pattern formation, Bubble dynamics, Boiling)

Education

Sep. 2006 Ph.D. (Mechanics, Acoustics and Electronics), Université Paris VI
Ph.D. Thesis: “Instabilité des interfaces sous oscillations”
Supervisor: Dr. José Eduardo Wesfreid
Dissertation committee: Prof. Stéphane Zaleski, Prof. Innocent Mutabazi, Prof. Tatyana Lyubimova,
Prof. Philippe Gondret, Dr. José-Eduardo Wesfreid

Mar. 2002 M.Eng. (Electrical Engineering), Doshisha University
Master thesis: “The momentum diffusion of a planar plasma jet in a homogeneous plasma,” Supervisor:
Prof. Motoi Wada

Mar. 2000 B.Eng. (Electronics), Doshisha University

Professional positions

Sep. 2013 – Associate Professor (MCF, Sec. 60; Université Nice Sophia-Antipolis)

Jan. 2013 – Aug. 2013 Postdoc. Research Fellow (CNRS)
Work on the heat transfer in the Görtler vortices, in the laboratory LOMC^{*1}, with Prof.
Innocent Mutabazi and Dr. Jorge Peixinho.

Jan. 2012 – Dec. 2012 Postdoc. Research Fellow (Le Havre University)
Work on the thermo-electro hydrodynamic instability, in the laboratory LOMC, with Prof.
Innocent Mutabazi.

-
- Sep. 2009 – Dec. 2011 Postdoc. Research Fellow (French Ministry of Higher Education & Research)
Work on a pattern formation problem in a two-phase system as well as on the local vapor bubble dynamics in pool boiling, in the laboratory J.-A. Dieudonné, with Drs. Christian Mathis, Germain Rousseaux and Philippe Maïssa.
 - Sep. 2007 – Aug. 2009 Postdoc. Research Fellow (CNES)
Work on the vapor bubble dynamics on a heating wall, in the IMFT^{*2}, with Prof. Catherine Colin.
 - Feb. 2007 – Aug. 2007 Postdoc. Research Fellow (CNRS)
Work on the stability of air bubbles in an oscillatory flow, in the laboratory PMMH^{*3}, with Drs. Philippe Petitjeans and Pascal Kurowski.
 - Nov. 2006 – Jan. 2007 Postdoc. Research Fellow (ESPCI^{*4})

Academic qualification

Qualified as an associate university professor by the French Ministry of Higher Education and Research in the following fields:

- Feb. 2011 Section 37 (Meteorology, Environmental physical oceanography)
- Jan. 2011 Section 60 (Mechanics, Mechanical engineering, Civil engineering)
- Feb. 2010 Section 62 (Energy engineering, Chemical engineering)

Project proposals

- 2014 Proposer of the PEPS Project (Physique théorique et ses interfaces):
“*Ondes internes dans un fluide diélectrique sous l’action de la gravité effective électrique*”.
Involved other investigators: Prof. Didier Clamond, Prof. Innocent Mutabazi, Dr. Olivier Crumeyrolle. Allocated amount: 3 000€.
- 2013 Co-proposer of the Labex EMC3 Projct:
“*Dynamique des Tourbillons de Görtler et Impact sur les Transferts Thermiques*”
Proposer: Prof. Abdellah Hadjadj (CORIA, Rouen). Involved other investigators: Dr. Jorge Peixinho, Prof. Innocent Mutabazi. Allocated amount: 136 400€.

Awards & Distinctions

- Research featured on the cover page of Eur. Phys. J. E, vol. 31, no. 2, 2010

Special experience

| Year/Month | Experiences | Objective |
|------------|---|--|
| 2009/03 | Participation in a CNES Parabolic Flight Campaign | Experimental study of the nucleate boiling |
| 2009/05 | Participation in an ESA Parabolic Flight Campaign | |

Teaching experiences

Teaching courses

| University year | Subject | College | Students | Level | Hours |
|-----------------|----------------------|--------------------------------|----------------|-------|---------|
| 2013 – | General Mechanics | Polytech Nice Sophia | Undergraduates | Ugrd. | 39/year |
| | Thermodynamics | Polytech Nice Sophia | Undergraduates | Ugrd. | 39/year |
| | Numerical Methods | Polytech Nice Sophia | Undergraduates | Ugrd. | 30/year |
| | Fluid Mechanics | Polytech Nice Sophia | Undergraduates | Ugrd. | 39/year |
| 2008 – 2009 | Analog Control Sys. | ICAM de Toulouse ^{*5} | Undergraduates | Ugrd. | 18 |
| | Analog Control Sys. | ICAM de Toulouse | Engineers | Ugrd. | 18 |
| | Digital Control Sys. | ICAM de Toulouse | Engineers | Ugrd. | 16 |

| University year | Subject | College | Students | Level | Hours |
|-----------------|----------------------|------------------|----------------|-------|-------|
| 2007 – 2008 | Analog Control Sys. | ICAM de Toulouse | Undergraduates | Ugrd. | 14 |
| | Digital Control Sys. | ICAM de Toulouse | Engineers | Ugrd. | 14 |

Supervising PhD researche

| University year | Candidate | University | Subject |
|-----------------|------------------------|---------------------|--|
| 2014 - | Antoine Mayer | Université du Havre | Thermoelectric instability of the Taylor-Couette flow |
| 2012 - 2013 | Mireille Tadie Fogaing | Université du Havre | Thermoelectric convection in a vertical cavity: Numerical simulation |

Supervising research training

| University year | Student | Training length | Subject |
|-----------------|---|-----------------|--|
| 2012–2013 | Antoine Meyer (Univ. Le Havre, Master) | 3 months | Thermoelectric convection |
| 2011–2012 | Victor Fronzi (ENSMA ^{*6}) | 3 months | Two-color LIF thermography |
| 2008–2009 | Grégory Houvin (ENSEEIH ^{*7} , Master) | 1 month | Vapor bubble dynamics on a heating wall |
| 2006–2007 | Virginie Titren (Univ. Paris 11, Ugrd.) | 1 month | Instability of two-layer oscillatory flows |
| 2005–2006 | Anne Bagué Xiaojing Zhang (Univ. Paris 6, Master) | } 1 month | Instability of two-layer oscillatory flows |
| 2004–2005 | Antoine Fornari (ESPCI, Ugrd.) | 1 month | Instability of two-layer oscillatory flows |

^{*1} Laboratoire Ondes et Milieux Complexes, UMR 6294 (<http://www.univ-lehavre.fr/recherche/lomc/>) ^{*2} Institut de Mécanique des Fluides de Toulouse, UMR 5502 (<https://www.imft.fr>) ^{*3} Physique et Mécanique des Milieux Hétérogènes, UMR 7636 (<http://www.pmmh.espci.fr/>)
^{*4} Ecole Supérieure de Physique et de Chimie Industrielles de la ville de Paris (<http://www.espci.fr>) ^{*5} Institut Catholique d'Arts et Métiers de Toulouse (<http://icam.groupe-icam.fr>) ^{*6} Ecole National Supérieure de Mécanique et d'Aérotechnique ^{*7} Ecole Nationale Supérieure d'Electrotechnique, d'Electronique, d'Informatique, d'Hydraulique et des Télécommunications (<http://www.enseiht.fr>)

Appendix B

List of Publications

Articles in Refereed Journals

1. Meyer, A., Yoshikawa, H., Mutabazi, I., “Effect of the radial buoyancy on a circular Couette flow,” *Phys. Fluids*, **27**, 114104, 2015
2. Yoshikawa, H., Meyer, A., Crumeyrolle, O., Mutabazi, I., “Linear stability of a circular Couette flow under a radial thermoelectric body force,” *Phys. Rev. E*, **91**, 033003, 2015
3. Tadie Fogaing, M., Yoshikawa, H., Crumeyrolle, O., Mutabazi, I., “Heat transfer in the thermo-electro-hydrodynamic convection under microgravity conditions,” *Eur. Phys. J. E*, **37**(4), 35, 2014
4. Yoshikawa, H., Nagata, M., Mutabazi, I., “Instability of the vertical annular flow with a radial heating and rotating inner cylinder,” *Phys. Fluids*, **25**, 114104, 2013
5. Yoshikawa, H., Tadie Fogaing, M., Crumeyrolle, O., Mutabazi, I., “Dielectrophoretic Rayleigh-Bénard convection under microgravity conditions,” *Phys. Rev. E*, **87**, 043003, 2013
6. Kosseifi, N., Biwole, P.H., Mathis, C., Rousseaux, G., Boyer, S.A.E., Yoshikawa, H., Coupez, T., “Application of two-color LIF thermometry to nucleate boiling,” *J. Mater. Sci. Eng. B* (David Publishing), **3**(5), pp. 281–290, 2013
7. Yoshikawa, H., Crumeyrolle, O., Mutabazi, I., “Dielectrophoretic force-driven thermal convection in annular geometry,” *Phys. Fluids*, **25**(2), 024106, 2013
8. Malik, S., Yoshikawa, H., Crumeyrolle, O., Mutabazi, I., “Thermo–electro–hydrodynamic instabilities in a dielectric liquid under microgravity,” *Acta Astronaut.*, **81**(2), pp. 563–569, 2012
9. van der Geld, C.W.M., Segers, Q., Pereira da Rosa, V.H., Colin, C., Yoshikawa, H., “Forces on a boiling bubble in a developing boundary layer, in microgravity with g-jitter and in terrestrial conditions,” *Phys. Fluids*, **24**, 082104, 2012
10. Yoshikawa, H., Wesfreid, J.E., “Oscillatory Kelvin-Helmholtz instability. Part 1. A viscous theory,” *J. Fluid Mech.*, **675**, pp. 223–248, 2011
11. Yoshikawa, H., Wesfreid, J.E., “Oscillatory Kelvin-Helmholtz instability. Part 2. An experiment in fluids with a large viscosity contrast,” *J. Fluid Mech.*, **675**, pp. 249–267, 2011

-
12. Yoshikawa, H., Mathis, C., Maïssa, P., Rousseaux, G., Douady, S., “Pattern formation in bubbles emerging periodically from a liquid free surface,” *Eur. Phys. J. E*, **33**(1), pp.11-18, 2010
 13. Yoshikawa, H., Zoueshtiagh, Z., Caps, H., Kurowski, P., Petitjeans, P., “Bubble splitting in oscillatory flows on ground and in reduced gravity,” *Eur. Phys. J. E*, **31**(2), pp.191-199, 2010
 14. Yoshikawa, H., Zoueshtiagh, Z., Caps, H., Kurowski, P., Petitjeans, P., “Bubble rupture in a vibrated liquid under microgravity”, *Microgravity Sci. Technol.*, **19**(3-4), pp.155-156, 2007
 15. Rousseaux, G.[†], Yoshikawa, H.[†], Stegner, A. and Wesfreid, J.E., “Dynamics of transient eddy above rolling-grain ripples,” *Phys. Fluids*, **16**(4), pp.1049-1058, 2004

† Co-first authors

Book chapter

1. Futterer, B., Yoshikawa, H., Mutabazi, I., Egbers, C., “Electric fields,” in *Generation on Earth of an extra-terrestrial environment*, Ed. J. van Loon & D. Beysens, River Publisher, 2015
2. Yoshikawa, H., Mathis, C., Maïssa, P., Rousseaux, G., “Spiral pattern formation in a simple two-phase flow system,” *Chaos, Complexity and Transport*, Ed. X. Leoncini & M. Leonetti, World scientific, pp. 113–122, 2012

Conference Papers

1. Lebon, M., Yoshikawa, H., Sebilleau, J., Colin, C., “Bubble formation in a quiescent liquid and in a shear flow,” Article #NSB 6 in *9th International Conference on Boiling & Condensation Heat Transfer*, Boulder, Colorado, 2015
2. Kahouadji, L., Yoshikawa, H., Peixinho, J., Mutabazi, I., “Heat transfer by Görtler vortices developed on a wall with finite conductivity,” *Rencontre du Non-Linéaire*, Paris, 2014
3. Kosseifi, N., Yoshikawa, H., Biwolé, P.H., Mathis, C., Rousseaux, G., Fronzi, V., Boyer, S.A.E., Coupez, T., “Application of two-colour LIF thermometry to nucleate boiling,” *ECI 8th International Conference on Boiling and Condensation Heat Transfer*, Lausanne, Switzerland, 2012
4. Yoshikawa, H., Colin, C., “Single vapour bubble behavior in a shear flow in microgravity,” *7th International Conference on Multiphase Flow*, Tampa, USA, May 30 – June 4, 2010
5. Colin, C., Legendre, D., Yoshikawa, H., Montout, M., “Hydrodynamics of bubble detachment in convective boiling,” *7th International Conference on Boiling Heat Transfer*, Florianópolis, Brazil, May 3–7, 2009
6. Yoshikawa, H., Rousseaux, G., Kruithof, J., Stegner, A., Wesfreid, J.E., “Flow structure over rolling-grain ripples – laboratory experiments and theoretical study,” *Proc. the Marine Sandwave and River Dune Dynamics*, pp. 346–351, 2004

Conferences

1. Yoshikawa, H., Meyer, A., Crumeyrolle, O., Mutabazi, I., “Stability of a circular Couette flow under radial thermal body forces,” *6th International Symposium on Bifurcations and Instabilities in Fluid Dynamics*, Paris, France, July 15–17, 2015
2. Yoshikawa, H., Meyer, A., Crumeyrolle, O., Mutabazi, I., “Wave generation in a circular Couette flow in thermoelectric radial buoyancy,” *19th International Couette-Taylor Workshop*, Cottbus, Germany, June 22–24, 2015
3. Lebon, M., Yoshikawa, H., Sebilliau, J., Colin, C., “Bubble formation in a quiescent liquid and in a shear flow,” *9th International Conference on Boiling & Condensation Heat Transfer*, Boulder, Colorado, April 26-30, 2015
4. Yoshikawa, H., Meyer, A., Crumeyrolle, O., Meyer, A., “Thermo-electrohydrodynamic internal waves in annular geometry,” *67th Annual Meeting of the APS Division of Fluid Dynamics*, San Francisco, USA, November 23–25, 2014
5. Kahouadji, L., Yoshikawa, H., Peixinho, J., Mutabazi, I., “Heat transfer by Görtler vortices developed on a wall with finite conductivity,” *Rencontre du Non-Linéaire*, Paris, 2014
6. Yoshikawa, H., Mutabazi, I., Crumeyrolle, O., Meyer, A., “Stability of the Taylor-Couette flow under a radial thermoelectric body force,” 66th Annual Meeting of the APS Division of Fluid Dynamics, Pittsburgh, USA, November 24–26, 2013
7. Mutabazi, I., Yoshikawa, H., Peixinho, J., Kahouadji, L., “Heat transfer enhancement by the Goertler vortices developed on a wall with a finite thermal conductivity,” 66th Annual Meeting of the APS Division of Fluid Dynamics, Pittsburgh, USA, November 24–26, 2013
8. Yoshikawa, H., Crumeyrolle, O., Mutabazi, I., “Couette-Taylor flow under a thermoelectric body force in microgravity,” *18th International Couette-Taylor Workshop*, Enschede, Netherlands, June 24–26, 2013
9. Yoshikawa, H., Crumeyrolle, O., Mutabazi, I., “DEP thermal convection in annular geometry under microgravity conditions,” *65th Annual Meeting of the APS Division of Fluid Dynamics*, San Diego, USA, November 18–20, 2012
10. Yoshikawa, H., Wesfreid, J.E., “Kelvin-Helmholtz instability in viscous two-layer oscillatory flow,” *4th International Symposium on Bifurcations and Instabilities in Fluid Dynamics*, Barcelona, Spain, July 18–21, 2011
11. Yoshikawa, H., Mathis, C., Maïssa, P., Rousseaux, G., “Spiral pattern formation in a simple two-phase flow system,” *Chaos, Complexity and Transport 11*, Marseilles, France, May 23–27, 2011
12. Yoshikawa, H., Mathis, C., Maïssa, P., Rousseaux, G., “Pattern formation of bubbles emerging on a free surface,” *New Trends On Growth And Form*, Agay, France, June 21–25, 2010
13. Yoshikawa, H., Mathis, C., Maïssa, P., Rousseaux, G., Douady, S., “Pattern formation of bubbles periodically emerging at a liquid free surface,” *11th Experimental Chaos and Complexity Conference 2010*, Lille, France, June 1–4, 2010
14. Yoshikawa, H., Zoueshtiagh, Z., Kurowski, P., Petitjeans, P., “Stabilité des bulles dans un champ d’accélération oscillant,” *GDR Microgravité Fondamentale et Appliquée Meeting*, Aussois, France, December 1–3, 2008

-
15. Yoshikawa, H., Vertier, B., Kanengieser, O., Colin, C., “Ecoulements diphasiques en ébullition,” GDR *Microgravité Fondamentale et Appliquée* Meeting, Aussois, France, December 1–3, 2008
 16. Yoshikawa, H., Colin, C., Legendre, D., “Prediction of bubble sliding and lift-off diameters at the wall in a shear flow,” *7th European Fluid Mechanics Conference, Manchester*, UK, September 15–18, 2008
 17. Yoshikawa, H., Colin, C., “Dynamics of single vapour bubbles nucleated and growing on a heating surface in μg ,” ESA Convective Boiling and Condensation Meeting, Noordwijk, Netherlands, December 6–7, 2007
 18. Yoshikawa, H., Zoueshtiagh, Z., Kurowski, P., Petitjeans, P., “Scission de bulles par une pesanteur artificielle,” GDR *Microgravité Fondamentale et Appliquée* Meeting, Fréjus, France, November 26–28, 2007
 19. Yoshikawa, H., Caps, H., Zoueshtiagh, Z., Kurowski, P., Petitjeans, P., “Bubble rupture in a vibrated liquid under microgravity,” *Second international topical team workshop on two-phase systems for ground and space application*, Kyoto, Japan, October 26–28, 2007
 20. Yoshikawa, H., Zoueshtiagh, Z., Caps, H., Kurowski, P., Petitjeans, P., “Break-up of bubbles and drops under modulated gravity,” *Elgra Biennial Symposium*, Florence, Italy, September 4–7, 2007
 21. Yoshikawa, H., Wesfreid, J.E., “Instabilité de Kelvin-Helmholtz anormale d’une interface à un fort contraste en viscosité sous un cisaillement oscillant,” *Euromech 493 – Interface dynamics, Stability and Fragmentation*, Grenoble, France, August 29–31, 2007
 22. Yoshikawa, H., Wesfreid, J.E., “Unsteady Kelvin-Helmholtz instability of an immiscible interface with a large contrast in viscosity,” *APS March Meeting*, Denver, USA, March 5–9, 2007
 23. Yoshikawa, H., Wesfreid, J.E., “Instability of superposed fluids subjected to tangential oscillation,” *6th European Fluid Mechanics Conference, Stockholm*, Sweden, June 26–30, 2006
 24. Yoshikawa, H., Wesfreid, J.E., “Instability of an interface, with large viscosity-contrast, under tangentially oscillatory motion,” *58th Annual Meeting of the APS Division of Fluid Dynamics*, Chicago, USA, November 20–22, 2005
 25. Yoshikawa, H., Wesfreid, J.E., “Dunes fluides ?,” GDR *Milieux Divisés* Meeting, Carry-le-Rouet, France, June 9–11, 2005
 26. Yoshikawa, H., Kruihof, J., Rousseaux, G., Wesfreid, J.E., “Fluid flow structure above sand ripples generated by oscillatory shear flow,” *International workshop on dunes and sand transport*, Carry-le-Rouet, France, June 9–11, 2004
 27. Yoshikawa, H., Rousseaux, G., Kruihof, J., Stegner, A. and Wesfreid, J.-E., “Flow structure over rolling-grain ripples – laboratory experiments and theoretical study,” *Marine Sandwave and River Dune Dynamics*, pp.168–175, Enschede, Netherlands, April 1–2, 2004
 28. Yoshikawa, H., Wesfreid, J.E., “Ecoulement moyen sur des rides marines,” *Journée de Physique Statistique*, Paris, France, January 29, 2004
 29. Yoshikawa, H., Rousseaux, G., Wesfreid, J.E., “Fluid flow morphology over sand ripples,” *Euromech Colloquium n.451 – Sea wave bottom boundary layer*, Taormina, Italy, October 26–29, 2003

Invited Seminars

1. "Fluid flow and heat transfer in the electric gravity," Japan Society of Mechanical Engineering, Hokkaido Division, Hokkaido University, Sapporo, Japan, April 10, 2015
2. "Fluid flow and heat transfer in electric effective gravity," Tokyo University of Science, Noda, Japan, April 5, 2015
3. "Formation de motifs phyllotactiques dans un écoulement à bulles," Institut PPRIME, Poitiers, France, March 21, 2013
4. "Convection thermique induite par la force diélectrophorétique en micropesanteur," Institut PPRIME, Poitiers, France, March 20, 2013
5. "Dielectrophoretic force-driven thermal convection in annular geometry," Brandenburg University of Technology, Cottbus, Germany, July 19, 2012
6. "Phyllotaxie hydrodynamique," Laboratoire Ondes et Milieux Complexes, Le Havre, France, December 10, 2010
7. "Ripple formation on a high-viscosity liquid layer," Observatoire de la Côte d'Azur, Nice, France, May 25, 2009
8. "Instabilité de Kelvin-Helmholtz des écoulements oscillants," Laboratoire Elaboration par Procédés Magnétiques, Grenoble, France, April 16, 2007
9. "Instabilité de Kelvin-Helmholtz des écoulements oscillants," Laboratoire de Mécanique, Physique et Géosciences, Le Havre, France, November 24, 2006

Appendix C

Selected articles published in international journals

TEHD convection in plane geometry

“Dielectrophoretic Rayleigh-Bénard convection under microgravity conditions,” *Phys. Rev. E*, **87**, 043003, 2013

“Heat transfer in the thermo-electro-hydrodynamic convection under microgravity conditions,” *Eur. Phys. J. E*, **37**, 35, 2014

TEHD convection in cylindrical geometry

“Dielectrophoretic force-driven thermal convection in annular geometry,” *Phys. Fluids*, **25**, 024106, 2013

Effects of a radial thermal gradient on a non-isothermal Taylor-Couette flow

“Instability of the vertical annular flow with a radial heating and rotating inner cylinder,” *Phys. Fluids*, **25**, 114104, 2013

Effects of a radial thermoelectric buoyancy force on a Taylor-Couette flow

“Linear stability of a circular Couette flow under a radial thermoelectric body force,” *Phys. Rev. E*, **91**, 033003, 2015

Stability of a bubble subjected to oscillatory flow

“Bubble splitting in oscillatory flows on ground and in reduced gravity,” *Eur. Phys. J. E*, **31**(2), 191–199, 2010

Pattern formation in a simple bubbly flow

“Pattern formation in bubbles emerging periodically from a liquid free surface,” *Eur. Phys. J. E*, **33**(1), 11–18, 2010

